REPORT NO. 3

MELT-GROWN OXIDE-METAL COMPOSITES

SEMI-ANNUAL TECHNICAL REPORT

(Period: 10 June 1971 to 9 December 1971)

Project Director
A. T. Chapman

Principal Investigators
J. F. Benzel R. J. Gerdes
R. K. Feeney J. W. Hooper
J. D. Norgard

Sponsored By
Advanced Research Projects Agency
Department of Defense

ARPA ORDER NO. 1637

Contract No. DAAH01-71-C-1046

January 1972

School of Ceramic Engineering
GEORGIA INSTITUTE OF TECHNOLOGY
Atlanta, Georgia

Unclassified
Security Classification

DOCUMENT CONTROL DATA - R & D

(Security classification of title, body of abstract and indexing annotation must be entered when the overall report is classified)

1. ORIGINATING ACTIVITY *(Corporate author)*
School of Ceramic Engineering
Georgia Institute of Technology

2a. REPORT SECURITY CLASSIFICATION
Unclassified

2b. GROUP

3. REPORT TITLE
MELT-GROWN OXIDE-METAL COMPOSITES

4. DESCRIPTIVE NOTES *(Type of report and inclusive dates)*
Semi-Annual (10 June 1971 - 9 December 1971)

5. AUTHOR(S) *(First name, middle initial, last name)*
Alan T. Chapman, James F. Benzel, Robert K. Feeney, Reiner J. Gerdes, John W. Hooper, J. D. Norgard

6. REPORT DATE	7a. TOTAL NO. OF PAGES	7b. NO. OF REFS
January 1972	116	5

8a. CONTRACT OR GRANT NO.	9a. ORIGINATOR'S REPORT NUMBER(S)
DAAH01-71-C-1046	E18-604-3
b. PROJECT NO.	
c.	9b. OTHER REPORT NO(S) *(Any other numbers that may be assigned this report)*
d.	ARPA ORDER NO. 1637

10. DISTRIBUTION STATEMENT
Distribution of this Document is unlimited.

11. SUPPLEMENTARY NOTES	12. SPONSORING MILITARY ACTIVITY
	Advanced Research Projects Agency 1400 Wilson Blvd. Arlington, Virginia 22209

13. ABSTRACT

Research work is underway developing melt-grown oxide-metal composite structures for electron emission testing. Prior to this report period, successful growth had been achieved only in the system UO_2-W and to a lesser extent in stabilized ZrO_2-W samples. The successful development of Y_2O_3 stabilized HfO_2-W as an additional refractory oxide-metal combination suited for composite growth is reported. Experiments using UO_2-Ta mixtures have produced extensive areas of Ta fiber growth in this oxide. Composition profiles obtained using the scanning electron microscope showed this instrument provided the necessary spatial resolution to examine individual oxide-matrix metal-fiber interfaces. The question of oxide stoichiometry and its influence on composite growth was extensively considered during all phases of composite growth. As a first step in the theoretical analysis of the emission anticipated from the composite structures, the electric potential distribution was determined in the interelectrode gap for several different array geometries. Experimental electron emission current densities of approximately 100 mA/cm^2 were routinely achieved, and attempts to exceed this density were limited by the onset of electrical breakdown in the test diode. With a segmental collector the emission from selected areas of the emitter surface was correlated with the growth-etch characteristics across the emitting surface.

DD FORM 1 NOV 68 1473 (PAGE 1)
S/N 0101-807-6801

Unclassified
Security Classification

14 KEY WORDS	LINK A		LINK B		LINK C	
	ROLE	WT	ROLE	WT	ROLE	WT
Oxide-Metal Composites		4				
Field Emission		4				
Rf Heating		3				
Field Emission Theory		3				
Oxides		2				
Refractory Metals		2				
Unidirectional Solidification		4				
Eutectic Structures		3				
UO_2		2				
ZrO_2 (Stabilized)		1				
HfO_2 (Stabilized)		1				
Internal Melting		3				
Etching		2				
Tungsten Fibers		4				
Electron Emitting Arrays		4				
Oxide-Metal Solidification		3				
High Field Emission		4				

Report No. 3

MELT-GROWN OXIDE-METAL COMPOSITES

SEMI-ANNUAL TECHNICAL REPORT

(Period: 10 June 1971 - 9 December 1971)

from

THE SCHOOL OF CERAMIC ENGINEERING
GEORGIA INSTITUTE OF TECHNOLOGY
ATLANTA, GEORGIA 30332

PROJECT DIRECTOR: A. T. CHAPMAN

January 1972

Sponsored by:
ADVANCED RESEARCH PROJECTS AGENCY
DEPARTMENT OF DEFENSE
ARPA ORDER NO. 1637

CONTRACT NO. DAAH01-71-C-1046

PERSONNEL PARTICIPATING IN PROJECT

Principal Investigators	Graduate Students
J. F. Benzel	W. F. Beaver
R. K. Feeney	N. E. Grynkewich
R. J. Gerdes	C. C. Jen
J. W. Hooper	T. A. Johnson
J. D. Norgard	W. L. Ohlinger
	J. W. Stendera
	M. D. Watson

TABLE OF CONTENTS

LIST OF ILLUSTRATIONS

LIST OF ILLUSTRATIONS (Continued)

LIST OF ILLUSTRATIONS (Continued)

LIST OF ILLUSTRATIONS (Continued)

LIST OF TABLES

FOREWARD

This research was supported by the Advanced Research Projects Agency of the Department of Defense and was monitored by the U. S. Army Missile Command under Contract Number DAAH01-71-C-1046.

"The views and conclusions contained in this document are those of the authors and should not be interpreted as necessarily representing the official policies, either expressed or implied, of the Advanced Research Projects Agency or the U. S. Government."

ABSTRACT

During the last eighteen months work has been underway developing melt-grown oxide-metal composite structures for electron emission testing. Prior to this report period, successful growth had been achieved only in the system UO_2-W and to a lesser extent in stabilized ZrO_2-W samples. The successful development of Y_2O_3 stabilized HfO_2-W as an additional refractory oxide-metal combination suited for composite growth is reported. Experiments using UO_2-Ta mixtures have produced extensive areas of Ta fiber growth in this oxide, and the growth of oxide-metal structures using metals other than W appear feasible. Composition profiles obtained using the scanning electron microscope showed this instrument provided the necessary spatial resolution to examine individual oxide-matrix metal-fiber interfaces and suggested the major metallic impurity, iron, is segregated in the W fibers.

The question of oxide stoichiometry and its influence on composite growth was extensively considered during all phases of composite growth. As a first step in the theoretical analysis of the emission anticipated from the composite structures, the electric potential distribution was determined in the interelectrode gap for several different array geometries. Experimental electron emission current

densities of approximately 100 mA/cm^2 were routinely achieved, and attempts to exceed this density were limited by the onset of electrical breakdown in the test diode. With a segmental collector the emission from selected areas of the emitter surface was correlated with the growth-etch characteristics across the emitting surface.

SECTION I

INTRODUCTION

This is the third report describing research performed on the "Melt-Grown Oxide-Metal Composite" Project, ARPA Order Number 1637, and also the Semi-Annual Technical Report for Contract DAAH01-71-C-1046, covering the report period 10 June 1971 through 10 December 1971. Previous reports[1,2] contained detailed descriptions of the modified floating zone technique and experimental facilities employed during the growth of the oxide-metal composite structures containing many millions of less than 1μdiameter tungsten fibers per cm^2 uniformly embedded in an oxide (insulating or semi-conducting) matrix. This information will be reviewed again only if it pertains to specific results presented in this Report.

The primary technical objective of this study is to understand the growth processes leading to coupled growth and ordered microstructures during the solidifications of refractory oxide-metal mixtures and to successfully produce useable samples of these composites and evaluate their potential for electronic applications, with the initial emphasis on electron field emission. The research program is divided into five areas to meet these objectives, and the work in these areas is outlined below.

A. INDUCTION COUPLING AND SOLIDIFICATION BEHAVIOR OF OXIDES AND OXIDE-METAL MIXTURES

A study of the chemical, thermal, electrical and mechanical variables active during the solidification of numerous induction melted oxides and oxide-metal mixtures is in progress to interpret and understand the parameters that control the successful growth of oxide-metal composites. Various techniques including doping, higher sample densification and higher preheat temperatures have been used to increase the number of oxide materials that can be internally melted by induction heating. During this report period the size and uniformity of stabilized ZrO_2-W samples has been greatly improved, and the first successful growth of oxide-metal composite structures in the system stabilized HfO_2-W has been achieved. Different refractory metals have been mixed with UO_2 to study composite growth in selected UO_2-metal systems.

B. STRUCTURAL AND CHEMICAL CHARACTERIZATION OF OXIDE-METAL COMPOSITES

As the different composite samples become available, they have been characterized with respect to their growth morphology and crystallographic orientation relationships, using predominantly x-ray diffraction and scanning electron microscopy (SEM) techniques. The study of the amount and location of impurities and dopants across cell and individual oxide-matrix metal-fiber interfaces, using primarily the energy dispersive x-ray detector of the SEM, has been initiated.

C. THE FORMATION OF OPTIMUM EMITTING ARRAYS

Composite growth experiments in the systems UO_2-W and ZrO_2-W are in progress to determine the practical limits of tungsten pin densities and diameters obtainable solidifying near eutectic compositions. Techniques to improve the uniformity of these arrays, specifically in pin spacings and diameters, and the continuity of the pins are under investigation. The influence of oxide stoichiometry changes on composite growth in the system UO_2-W is discussed. Chemical etching approaches are being used to develop improved techniques to expose, shape and recess the metallic pins in the different oxide matrixes.

D. FIELD EMISSION THEORY

Analytical and numerical techniques are being used to theoretically determine the field emission current from a generalized emitting array. Such variables as pin shape, pin height, pin radius and the properties of the matrix are included in the analysis. Since it is impossible to fabricate an array having all pins of uniform height, radius and spacings, the effects of distributions of these variables will be considered. The electric field strength in the interelectrode gap has been determined for several different pin geometries.

E. EXPERIMENTAL EMISSION MEASUREMENTS

The electron emission performance of oxide-metal composites is being evaluated in a diode structure as a function of array geometry and such electrical variables as field strength and interelectrode spacing. Emission measurements are conducted under carefully controlled conditions so that the onset of physical damage to the emitter structure can be determined. A segmental collector has proved especially useful in equating emission characteristics with emitter geometries. The emission measurements are ultimately directed toward predicting the performance of the oxide-metal composite cathodes in practical electron devices.

SECTION II

INDUCTION COUPLING AND SOLIDIFICATION BEHAVIOR OF OXIDES AND OXIDE-METAL MIXTURES

This section is subdivided into two subsections: A) Induction Coupling and Melting Behavior of Oxide Systems, and B) Solidification Behavior of Oxide-Metal Systems. These subsections cover investigations designed to develop new oxide systems that are capable of being internally melted by high frequency induction heating and attempts to combine these oxides with refractory metals to form useful oxide-metal composite structures. The description of current work in the most advanced system, UO_2-W, is covered in Section IV.

A. INDUCTION COUPLING AND MELTING BEHAVIOR OF OXIDE SYSTEMS

Melting and subsequent controlled solidification of refractory oxides and oxide-metal mixtures have been previously accomplished[1,2] using high (4 to 30 MHz) frequency rf heating. This technique is limited to systems that have sufficient electrical conductivity at elevated temperatures to support eddy-current heating at the level required to produce internal melting.

During the first half of this contract period a number of oxides, binary oxide compounds and oxide mixtures have

been tested to determine their suitability for internal melting using the rf coupling scheme. A compilation of the test results including preheat temperatures, rf coupling and melting behavior and miscellaneous comments for the three classes of materials - oxides, oxide compounds and oxide mixtures - are presented in Tables I and II. Sample preparation and testing were carried out in the manner previously described[1,2] except as noted in the Tables.

Of the single and binary oxide compounds tested (Table I), TiO_{2-x} appears to be the best candidate for use in composite structures. The addition of 5 weight % of -325 mesh titanium metal seems to have eliminated the outgassing of oxygen resulting from the change in stoichiometry. As can be seen in Figure 1, the metal addition has changed the color of the titania suboxide from white to black. Microscopic examination of the polished cross section did not reveal the presence of a metallic phase. However, under bright field illumination three oxide phases were observed: a matrix composed of light and dark blue grains and orange colored platelets. Of the oxide mixtures tested (Table II), HfO_2 + 10 mole % CaO and ZnO + 20 mole % Nb_2O_5 were the only ones to form a stable molten zone. However, they both suffer from other problems. During melting of the HfO_2-CaO mixture, a reddish-brown substance was deposited on the quartz atmosphere tube of the growth system which prevented accurate temperature measurements. This problem may be related to the formation of a

Figure 1. Polished Section of an Induction Melted TiO_2 Sample Containing 5 Weight % Addition of Ti Metal. X3.5.

compound between the two components of the mixture or between the components and the glassy carbon preheat tube. The ZnO-Nb_2O_5 eutectic mixture containing 30 mole % Nb_2O_5 (melting point 1285°C) was unsuccessfully tested earlier[1]. This two component system has another eutectic composition occurring at approximately 20 mole % Nb_2O_5 (melting point 1308°C). As indicated in Table II this second eutectic was easily internally melted; but, because of the low melting temperature, the surface of the pellet did not emit enough thermal energy to remain solid and contain the molten zone. This eutectic mixture may have potential for developing low temperature oxide-metal composites if the molten zone can be contained by using a lower rf frequency or by cooling the external surface of the sample.

Based on the experimental results observed during this report period, it appears that because of rf arcing problems the best method of improving the coupling efficiency of oxides and oxide mixtures is to decrease the rf frequency and utilize higher preheat temperatures to obtain the required electrical conductivity to support eddy current heating.

TABLE I

INDUCTION MELTING BEHAVIOR OF SINGLE AND BINARY OXIDE COMPOUNDS

Oxide	Preheating °C	Type Susceptor	Frequency (MHz)	Atmosphere	Behavior rf Coupled	Behavior Melted	Comments or Problems
ThO_2	1900	Glassy Carbon	7.6	H_2-N_2	No	No	Broke up during cooling.
$NiO \cdot TiO_2$	1300	Mo	3.8	N_2	Yes	Yes	Top of pellet "popped off" due to release of oxygen from liquid.
$NiO \cdot (1+x)TiO_2$	1300	Mo	3.8	N_2	Yes	Yes	Increasing the TiO_2 to NiO ratio indicated that excess TiO_2 (10 wt.%) reduces but does not eliminate outgassing problem.
$NiO \cdot TiO_{2-x}$	1300	Mo	3.8	N_2	Yes	Yes	Addition of 5 wt.% Ti metal reduced the stoichiometry of sample to the extent that nickel metal was precipitated
$NiO \cdot TiO_2$	1300	Mo	3.8	N_2	Yes	Yes	A hole drilled halfway down through a pressed pellet was quickly closed by molten material when a molten zone formed.
TiO_{2-x}	1100	Mo	3.8	N_2	Yes	Yes	A 5 wt.% addition of titanium metal appears to have eliminated the stoichiometry outgassing problem in this system.

TABLE I (Continued)

Oxide	Preheating °C	Type Susceptor	Frequency (MHz)	Atmosphere	Behavior rf Coupled	Melted	Comments or Problems
Y_2O_3	1800	Mo	3.8	H_2-N_2	Yes	No	Broke up on cooling.
Y_2O_3	1800	Mo	3.8	N_2	Yes	No	Broke up on cooling.

TABLE II

INDUCTION MELTING BEHAVIOR OF OXIDE MIXTURES

Oxide* Mixture	Preheating °C	Type Susceptor	Frequency (MHz)	Atmosphere	Behavior rf Coupled	Behavior Melted	Comments or Problems
Cr_2O_3+40% (ZrO_2+5%CaO)	1575	SiC	32	Air	Yes	Yes	Only small molten zones were formed. Coupling was unstable, and molten zones were lost after a very short time (~30 sec.)
Cr_2O_3+20% (ZrO_2+5%CaO)	1580	SiC	32	Air	Yes	No	Same as above.
HfO_2+10%CaO	1540	SiC	32	Air	Yes	No	
HfO_2+10%CaO	1650	Glassy Carbon	32	N_2	Yes	No	Arcing prevented the sample from being preheated to a higher temperature.
HfO_2+10%CaO	1810	Glassy Carbon	7.6	N_2	Yes	No	Almost internally melted.
HfO_2+10%CaO	(Approx. 1850)	Glassy Carbon	7.6	H_2-N_2	Yes	Yes	Reddish deposit formed on inside of quartz tube which prevented accurate temperature measurement. Stable internal molten zone formed.
HfO_2+10%CeO_2	1560	SiC	32	Air	Yes	No	

TABLE II (Continued)

Oxide* Mixture	Preheating °C	Type Susceptor	Frequency (MHz)	Atmosphere	Behavior rf Coupled	Behavior Melted	Comments or Problems
HfO_2+10%CeO_2	1970	Mo	3.8	H_2-N_2	-	-	Reacted with preheat tube. Area in contact with Al_2O_3 support rod melted.
HfO_2+15%Y_2O_3	1600	SiC	32	Air	Yes	No	
HfO_2+9wt%Y_2O_3	1950	Mo	3.8	H_2-N_2	Yes	No	
Y_2O_3+10wt% $CaCO_3$	1800	Mo	3.8	H_2-N_2	Yes	No	Broke up on cooling.
Y_2O_3+4wt% $SrCO_3$	1850	Mo	3.8	H_2-N_2	Maybe	No	Broke up on cooling.
Y_2O_3+10wt% ZrO_2	1850	Mo	3.8	H_2-N_2	Yes	No	Broke up on cooling.
ZnO+20wt% Nb_2O_5	1250	SiC	23	Air	Yes	Yes	ZnO did not sublime but because of this eutectic's low melting point the molten material melted through the pellet's walls.

*Oxide additions are in mole % unless otherwise indicated.

B. SOLIDIFICATION BEHAVIOR OF OXIDE-METAL SYSTEMS

The research included in this subsection was designed to improve and interpret the growth of oxide-metal eutectic structures in systems other than UO_2-W and to determine if oxides that can be internally melted by rf heating exhibit coupled (ordered) growth when solidified with metal additions. Prior to this report period only the growth of UO_2-W samples had been controlled well enough to warrant emission testing. Extensive ordered growth in the system stabilized ZrO_2-W has been achieved, and the initial emission testing of this material is reported in Section V of this Report. The growth of ordered W fibers in a stabilized HfO_2 matrix has been successfully accomplished, and the results of early work in this system are presented. A number of additional metals besides tungsten have been tested as the metallic component during the solidification of UO_2-metal samples. Encouraging results with UO_2-Ta samples have been obtained.

1. Stabilized ZrO_2-W

The melt-growth of oxide-metal composites in the system stabilized ZrO_2-W has advanced significantly during this report period. Composite specimens with "good" fiber growth running the entire length of the zone travel ($\sim$2 cm) have been obtained. This achievement has primarily been the result of varying (lowering) the rf frequency employed during

growth and establishing the influence that the stabilizer and tungsten content have on the composite structures. Work in these areas and the initial experiments designed to study the effect of the atmosphere on the stoichiometry (O:Zr ratio) of molten ZrO_2 are discussed in this subsection.

The frequency used to induction heat stabilized ZrO_2-W rods has a great effect in the ability to establish a stable internal molten zone. Frequencies used with ZrO_2-Y_2O_3-W mixtures have been 16, 7.6, and 3.8 MHz. Initially the higher frequencies were used because only at these higher frequencies was it possible to establish eddy-current heating in these poorly electrical conducting materials. With 16 MHz, ZrO_2-Y_2O_3 mixtures could be easily melted; but rf arcing and spills of the molten zone were problems. At 7.6 MHz the samples could also be melted and arcing problems were reduced; however, there was difficulty establishing a power setting high enough to insure complete internal melting while still maintaining the integrity of the thin solid skin.

Improved coil-sample geometries and increased preheat temperatures have lead to the successful rf melting of ZrO_2-Y_2O_3-W mixtures at 3.8 MHz. At this frequency the increased rf penetration leads to a thick unmelted shell to contain the molten zone, and increased power assures complete internal melting. During typical experiments ZrO_2-Y_2O_3-W rods approximately 19mm in diameter were preheated and sintered using a N_2-H_2 atmosphere at 1650-1700°C inside a

molybdenum tube and internally melted with a skin temperature of about 1870°C. (These are uncorrected, as-read optical temperatures obtained sighting directly on the Mo tube or oxide-metal rod.)

Variations in the amount of Y_2O_3 stabilizer and metal additions in the ZrO_2-Y_2O_3-W system have been studied to find compositions suitable for composite growth. Duwez, et.al.,[3] report that ZrO_2 and Y_2O_3 form a cubic solid solution from 7 to 56 mole % Y_2O_3 at 2000°C. The Y_2O_3 addition is necessary to produce a cubic solid solution which does not have any disruptive crystal lattice changes. Pure ZrO_2 and ZrO_2-Y_2O_3 mixtures with less than 7 mole % Y_2O_3 show a lattice transformation from monoclinic to tetragonal at about 1000°C, and a volume change of about 9% which would cause severe cracking, especially during cooling.

Samples containing 7.9 mole % Y_2O_3 and various amounts of W were induction melted. When 5 weight % W was used, the sample contained areas of fiber growth and also large areas of primary oxide without any W. With 10 weight % W, the samples contained uniform fibers throughout the melt zone. An addition of 15 weight % W to the ZrO_2 - 7.9 mole % Y_2O_3 mixture produced W dendrites in addition to the W fibers.

Increasing the Y_2O_3 content to 10 mole % also yielded samples displaying "good" growth; however, with this oxide mixture 15 weight % W was required. Tungsten additions above and below 15 weight % produced similar structural changes to

that noted for the ZrO_2-7.9 mole % Y_2O_3-10 weight % W described above.

In an initial experiment employing 12.5 mole % Y_2O_3 and 15 weight % W additions to ZrO_2, the structure shown in Figure 2 was obtained. With this composition the primary oxide phase appears at the cell (grain) boundaries rather than in isolated circular areas typical of oxide-rich mixtures[1,2]. This result seems compatible with the trend requiring an increased amount of W as the quantity of Y_2O_3 stabilizer added to ZrO_2 is increased in order to form "good" uniform oxide-metal structures.

Transverse and longitudinal views typical of the stabilized ZrO_2-W composites using the 10 and 7.9 mole % addition of Y_2O_3 and the 15 and 10 weight % addition of W are presented in Figures 3 and 4. Figure 3 shows a sample that was lowered at 1.85 cm/hr. The fibers are 0.3 microns in diameter, and there are about 20 million fibers per cm^2. Figure 4 shows that the fibers are continuous but have a wavy pattern. In addition to the uniform continuous fibers shown in these Figures, other types of structures have been observed. Banded fiber growth occasionally occurred in samples for reasons unknown as yet, and two different forms of banding have been identified. In the first type, Figure 5, the fibers are simply interrupted by a band of oxide a few microns thick. The fibers continue on the other side of the oxide band just as if the discontinuity had never occurred. In the second type

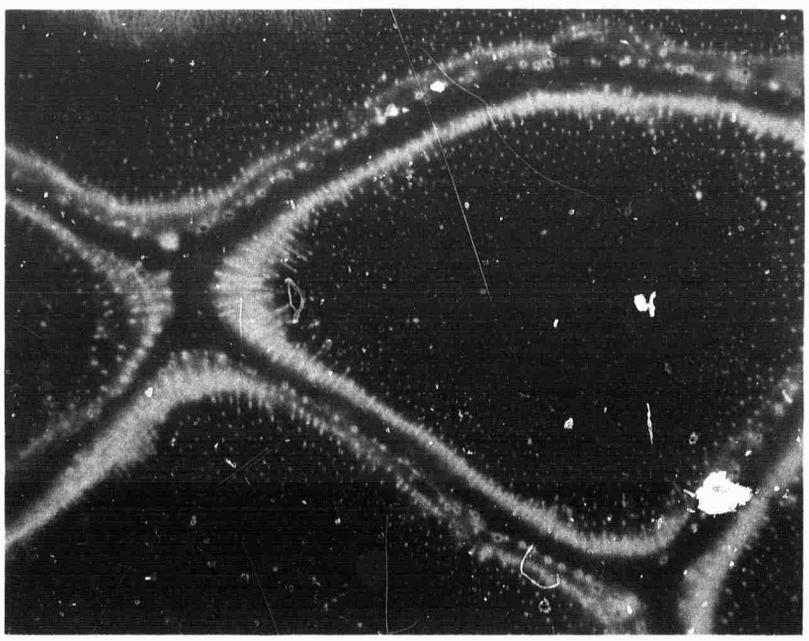

Figure 2. Transverse Section of a ZrO_2-12.5 mole % Y_2O_3 - 15 Weight % W Sample Displaying Primary Oxide Phase in the Cell Boundaries. Dark Field, X600.

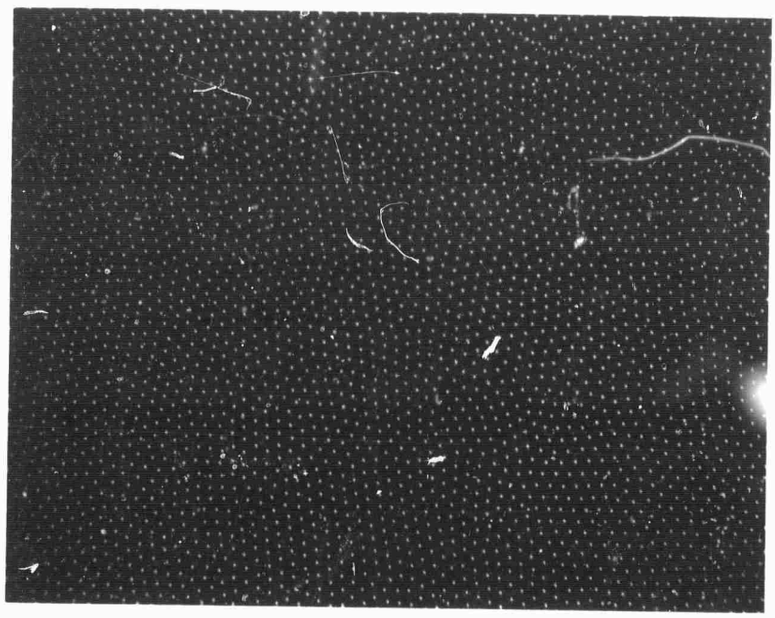

Figure 3. Transverse Section of "Good" Growth in a ZrO_2 - 10 Mole % Y_2O_3 - 15 Weight % W Sample. Dark Field, X600.

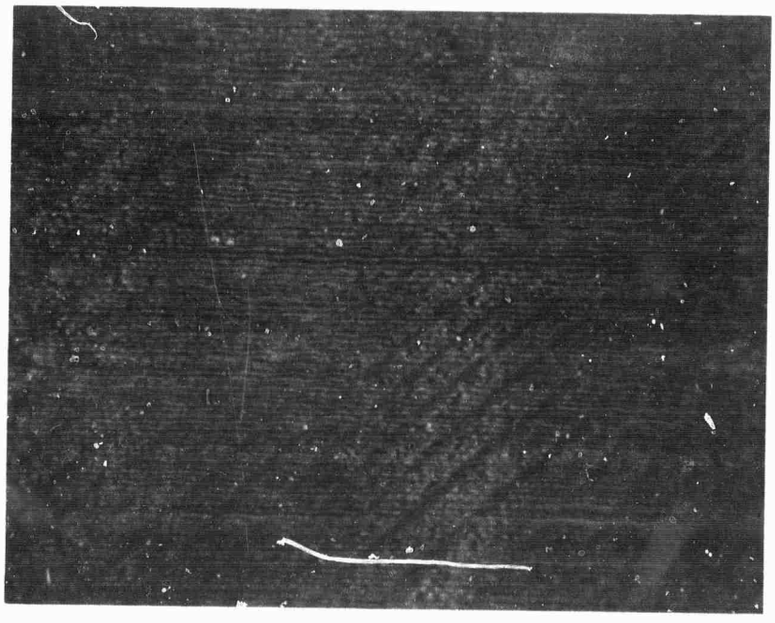

Figure 4. Longitudinal Section of "Good" Fiber Growth in a ZrO_2-7.9 Mole % Y_2O_3 - 10 Weight % W Sample. Dark Field, X600.

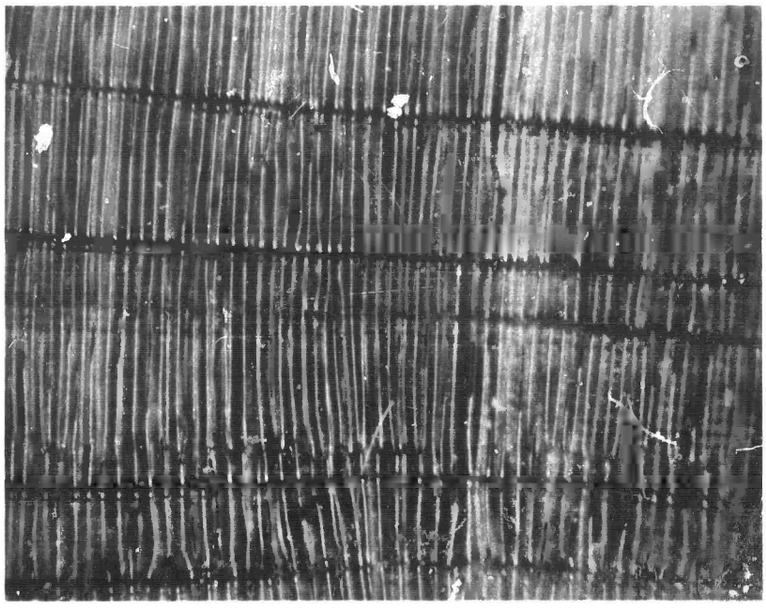

Figure 5. Longitudinal Section of a Stabilized ZrO_2-W Sample Showing the First Type of "Banding". Dark Field, X600.

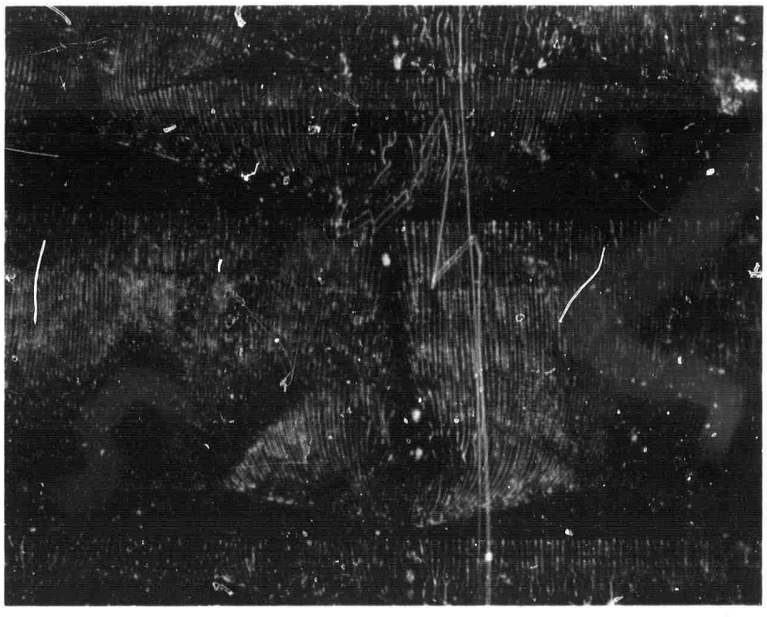

Figure 6. Longitudinal Section of a UO_2-W Specimen Displaying the Fan Type Growth Characteristics of the Second Type of "Banding". Dark Field, X600.

of banded structure, shown in Figure 6, the oxide band is wider; and the fibers appear to re-nucleate from a single point and fan out. Possible reasons for banded growth include non-eutectic liquid composition, fluctuations in the power causing remelting of an area already solidified, or fluctuations in the lowering rate.

In addition to fiber growth, several samples have shown extensive areas containing W platelets. The W platelets appear about a micron thick and a few hundred microns on a side. They are generally rectangular but sometimes have six or eight sides. Orientation of the platelets at first appears random, but careful observation reveals a regular angular relationship between the platelets. The matrix areas in which platelets have been observed have always been more transparent than those regions containing fibers in the same sample. This facilitates observation with a microscope since the plane of focus can be moved down through the sample. Figure 7 shows one plane of platelets in focus and many platelets in other planes which are out of focus. The orientation and shapes of the platelets may be an indication that they are not formed upon solidification. The W may be retained in solution as the matrix solidified and subsequently precipitated from the solid solution on selected crystallographic planes of the ZrO_2-Y_2O_3 matrix in a solid state process.

A study of the effect of atmosphere on the stoichiometry of molten Y_2O_3 stabilized ZrO_2 was initiated. Carniglia,

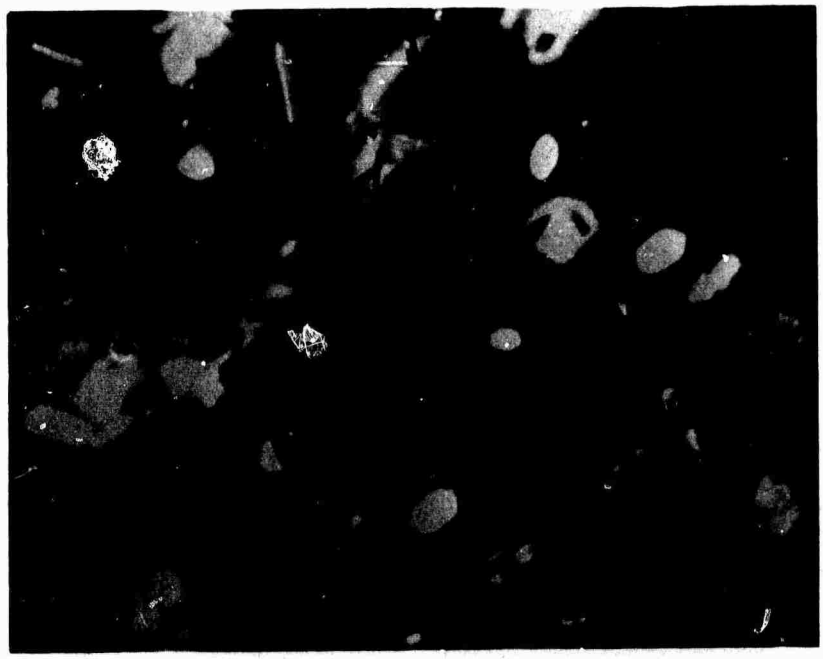

Figure 7. Tungsten Platelets in a Stabilized ZrO_2 Matrix. One Plane of Platelets Is in Focus While the Remaining Platelets Are Blurred. Dark Field, X600.

et.al.[4], report non-stoichiometric oxygen-deficient ZrO_2 is black, while stoichiometric ZrO_2 is white. Normally the stabilized ZrO_2-W samples have been grown in an atmosphere consisting of 90% N_2 and 10% H_2 by volume. These samples have a white unmelted skin and a black molten interior attributed to substoichiometry or the presence of the W fibers. A sample of ZrO_2-10 mole % Y_2O_3 containing no W was melted in the 90% N_2-10% H_2 atmosphere, partially lowered, and then rapidly cooled (quenched). Figure 8 shows this sample; the extensive cracking is the result of the shock of quenching. Most of this sample is composed of clear, transparent, yellow-tinted crystals, suggesting they are nearly stoichiometric. The rapidly cooled upper portion of the melt zone is dark colored and contains a small amount of a metallic phase, suspected to be Zr metal. Apparently in the molten state the oxide is oxygen deficient. Upon slow cooling the non-stoichiometric phase picks up oxygen from the oxygen content in the N_2-H_2 atmosphere and is converted back toward the stoichiometric O:Zr ratio of 2.00.

Two additional samples of the same composition, ZrO_2-10 mole % Y_2O_3, were melted in atmospheres consisting solely of N_2 or of H_2. In both cases the samples were held in their respective environment for four hours and then quenched. The sample held in N_2 contained primarily clear, yellow-tinted crystals; but some dark as well as two-phase areas were also observed. The molten interior of the sample, Figure 9, run

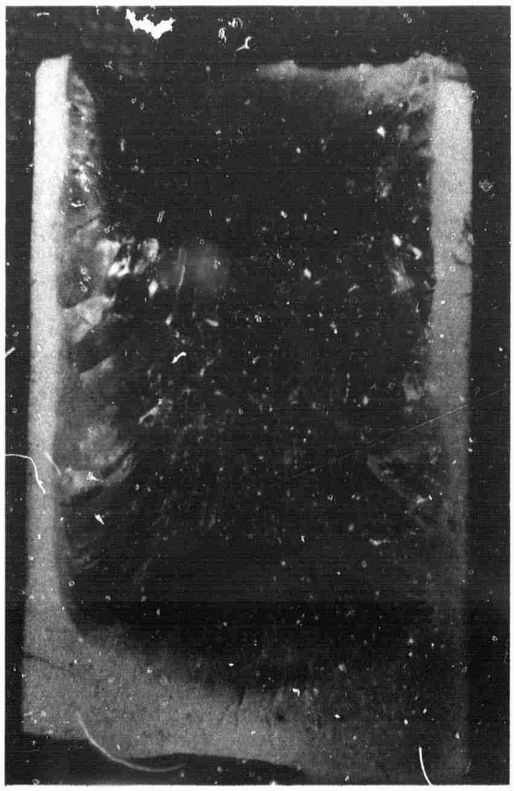

Figure 8. Polished Section of a ZrO_2 - 10 Mole % Y_2O_3 Pellet Melted in a N_2:H_2 Atmosphere Showing Transparent Crystals in the Slow-Cooled Base and Dark Substoichiometric Material in the Quenched Top of the Sample. X3.5.

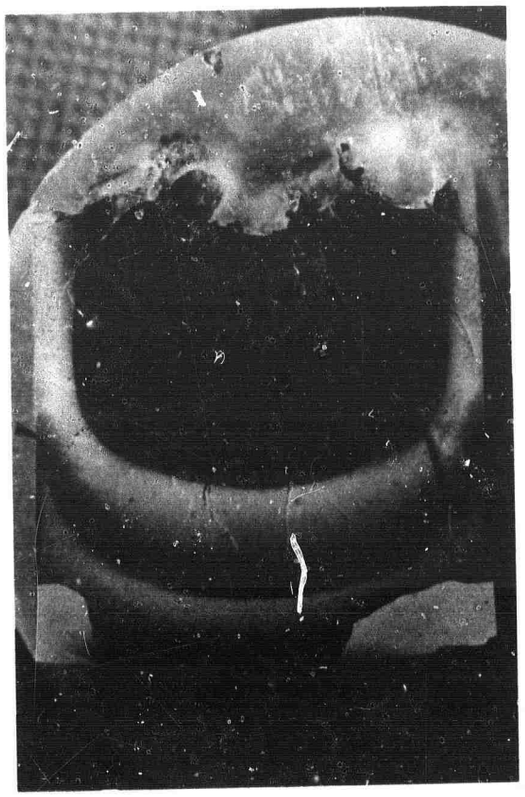

Figure 9. Polished Section of a ZrO_2-10 Mole % Y_2O_3 Pellet Melted in H_2 and Quenched. The Dark Substoichiometric Material Is Present Throughout the Molten Zone. X4.

in H_2, was black; and metallic inclusions were present.

An extensive description of the role oxide stoichiometry changes play during the growth of UO_2-W is presented in Section IV. Many of these comments may be applicable to the stabilized ZrO_2-W system.

2. Stabilized HfO_2-W

The success of rf melting HfO_2 stabilized with CaO (noted in Table II) suggested that this oxide is suitable for composite growth. The difficulties encountered in obtaining satisfactory oxide-metal structures employing HfO_2-CaO-W mixtures and the subsequent improved structures obtained by substituting Y_2O_3 in place of CaO are described.

The initial selection of hafnia, oxide-stabilizer, and tungsten ratios for testing were based on similar ratios in the stabilized ZrO_2-W system because of the chemical similarity between HfO_2 and ZrO_2. In the first successful internal melting of a stabilized HfO_2-W mixture, a hafnia pellet containing 6 weight % of both CaO and W was preheated to 1850°C using a 7.6 MHz field and a vitreous graphite preheater in a H_2-N_2 atmosphere. Both this pellet and a duplicate run with the same composition were difficult to control after melting because of a reddish-brown vapor deposit that coated the silica tube used to contain the samples. In an effort to gain more control of the melt temperature and improve the stability of the molten zone, another sample of the same

composition was preheated to 1990°C using a molybdenum preheat tube and an rf frequency of 3.8 MHz. This procedure reduced the vapor deposits on the SiO_2 tube, and the sample readily melted; however, difficulty was encountered moving the molten zone through the pellet.

Examination of the HfO_2-CaO-W samples melted using the 7.6 and 3.8 MHz rf fields revealed that the specimen melted at the lower frequency possessed a thicker unmelted skin (Figure 10). Tungsten dendrites were observed (Figure 11) in some areas of the solidified oxide; however, no ordered oxide-metal structures were observed. Isolated fibers (Figure 12) were observed in another pellet of the same composition that was preheated to 2000°C and melted using a 3.8 MHz field. In addition, portions of the matrix appeared to consist of a two-phase oxide structure (Figure 13). Both HfO_2 and W are capable of forming compounds with CaO. Increasing the tungsten content to 10 and 12 weight % improved the fiber structure only slightly (Figure 14), and the two-oxide phases were still present.

Even though previous attempts to couple to HfO_2 which was stabilized with yttria were unsuccessful, an attempt was made to melt this system with a tungsten addition. Tungsten was added to hafnia stabilized with 10 mole % yttria in the amount of 10 weight % of the stabilized mixture. This pellet was preheated using a Mo susceptor to 1950°C, internally melted using a 3.8 MHz field in a H_2-N_2 atmosphere, and lowered at

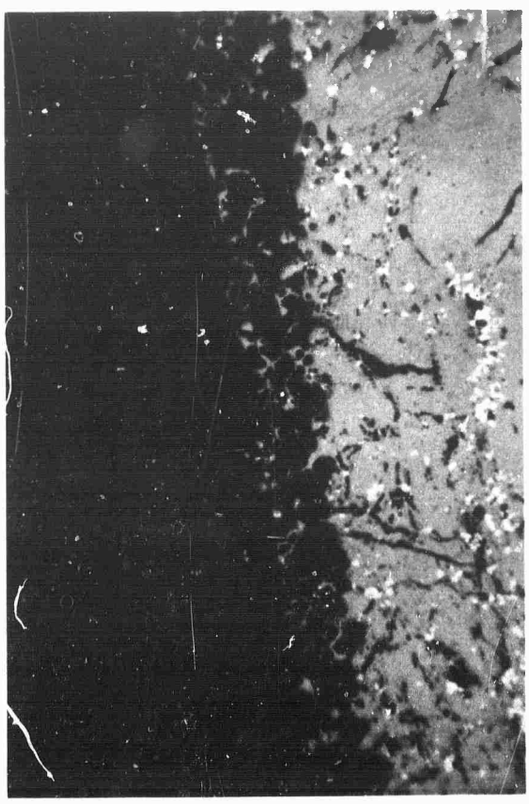

a) Melted at 7.6 MHz.

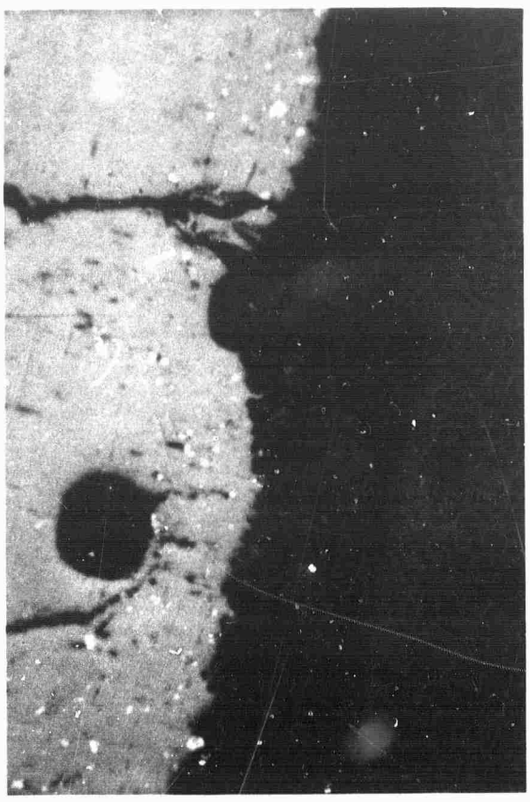

b) Melted at 3.8 MHz.

Figure 10. Polished Sections of HfO_2-Y_2O_3-W Samples Showing Difference in Unmelted Skin Thickness for Pellets Melted at 7.6 and 3.8 MHz. Bright Field, X50.

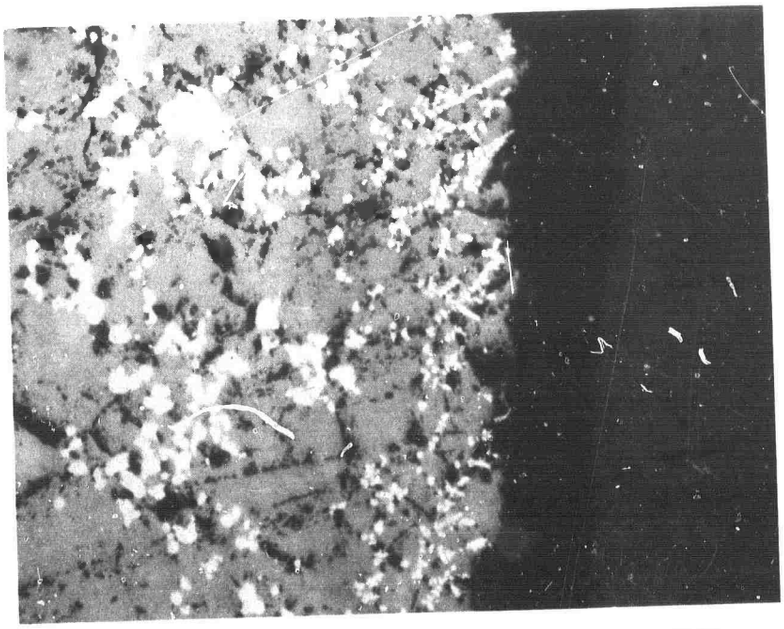

Figure 11. Tungsten Dendrites in a Solidified HfO_2 - 6 Weight % CaO - 6 Weight % W Sample. Bright Field, X600.

Figure 12. Random Tungsten Fibers in a Solidified HfO_2 - 6 Weight % CaO - 6 Weight % W Specimen. Dark Field, X600.

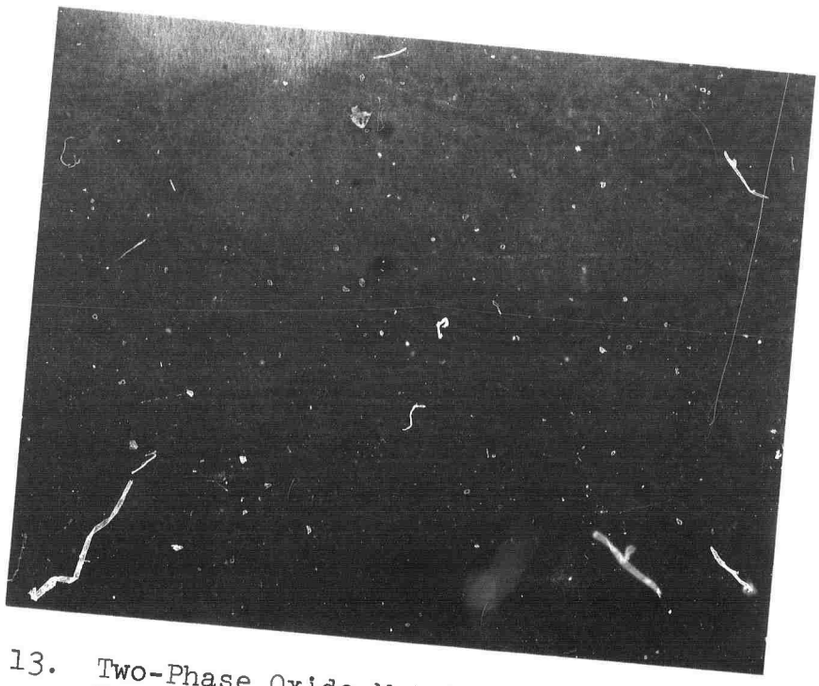

Figure 13. Two-Phase Oxide Matrix Present in a Solidified HfO_2 - 6 Weight % CaO - 6 Weight % W Sample. Bright Field, X600.

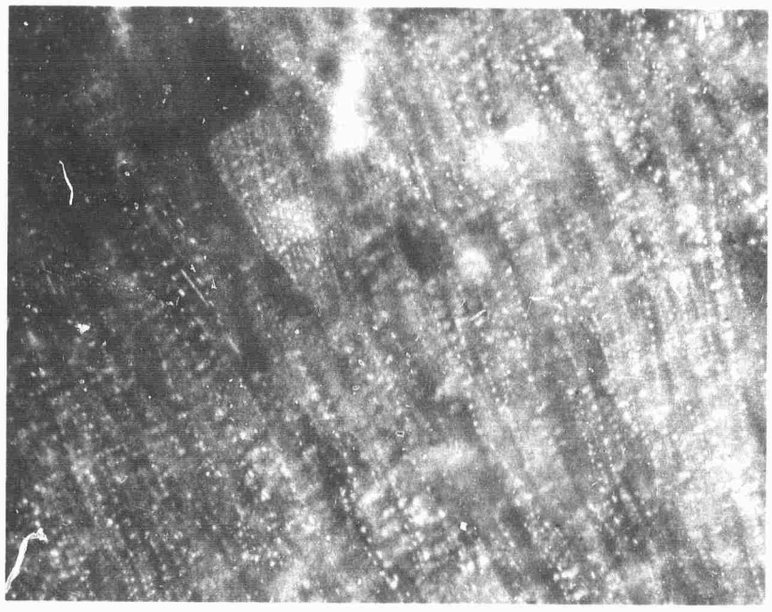

a) Containing
10 Weight % W.

b) Containing
12 Weight % W.

Figure 14. Tungsten Fiber Structures Present in a CaO Stabilized HfO_2 Pellet Containing a) 10 Weight % W, and b) 12 Weight % W. Dark Field, X600.

about 3 cm/hr. Figure 15 shows the resultant well-ordered fiber structure in a single-phase oxide matrix. Another pellet containing the same amount of yttria and tungsten was melted under identical conditions. It showed the same oxide-metal geometry as the previous pellet; but the melt zone was much longer, and there was considerable "banding" present (Figure 16), typical of that observed for the stabilized ZrO_2-W and UO_2-W structures. Since the "banded" structure may be an indication that not enough metal was present to produce the eutectic composition, additional samples where 12 and 14 weight % W was added to the stabilized oxide were prepared, and after internal melting, lowered through the field at about 1 cm/hr. The 12% W sample contained better fiber growth and less banding than that of 10 weight % sample. Several areas of short tungsten platelets oriented in two or three directions, similar to those seen in some ZrO_2-W samples, were also observed in this sample (Figure 17). The sample containing 14 weight % W also contained well-ordered parallel fibers throughout most of the solidified melt (Figure 18), but a small amount of banding was still present. The oxide matrix in all the Y_2O_3 stabilized HfO_2 samples appeared to be a single phase.

All of the Y_2O_3 stabilized HfO_2-W composites contained cracks which are assumed to be due to the severe thermal gradient present. Methods of eliminating these cracks are under investigation.

Figure 15. Longitudinal Section of a Y_2O_3 Stabilized HfO_2 Sample to Which 10 Weight % W Was Added. Dark Field, X600.

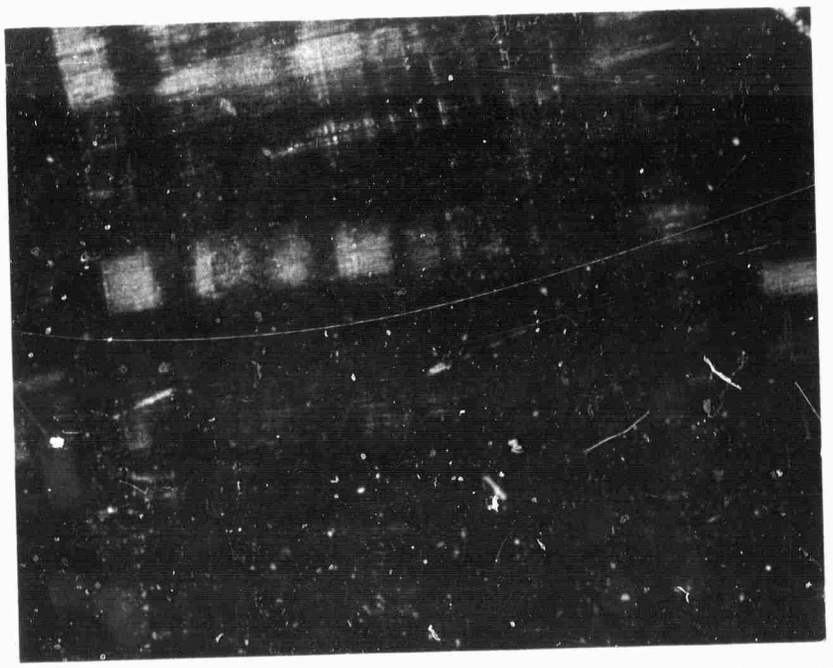

Figure 16. "Banded" W Fiber Growth in a Y_2O_3-HfO_2-W Sample. Dark Field, X200.

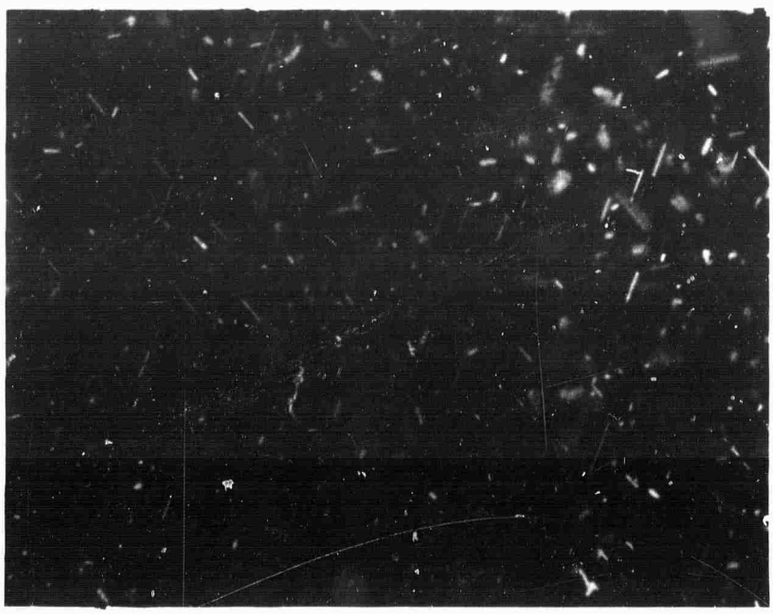

Figure 17. Tungsten Platelets and Rods Present in Some Areas of a Y_2O_3 Stabilized HfO_2 Sample to Which 12 Weight % W Was Added. Dark Field, X600.

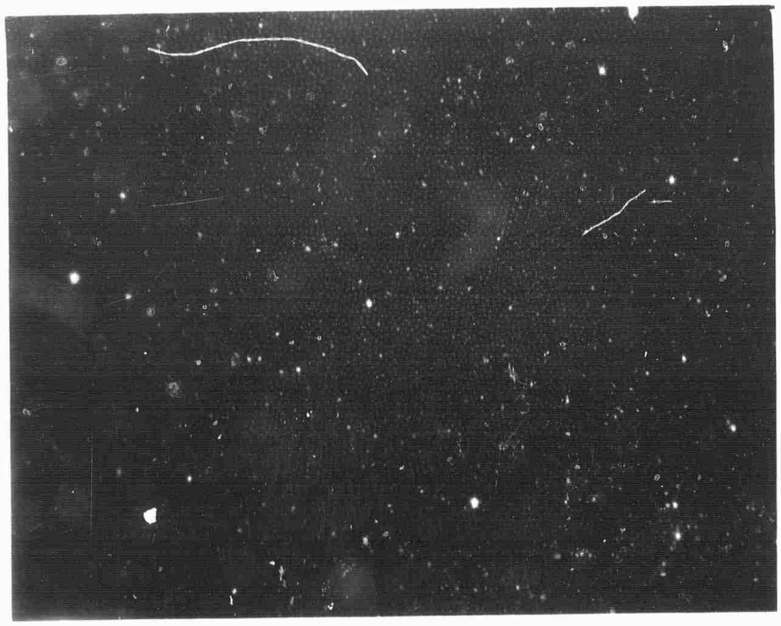

a) Transverse Section

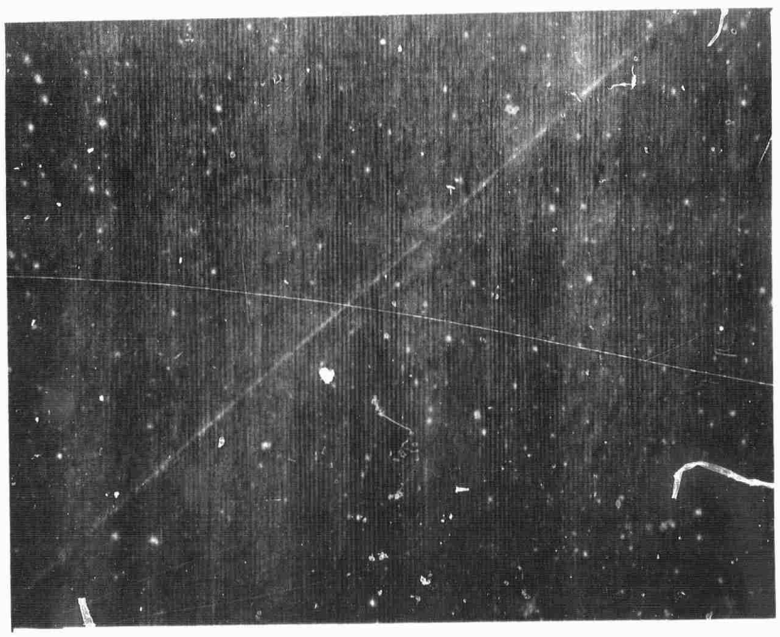

b) Longitudinal Section

Figure 18. Transverse and Longitudinal Sections of "Good" Fiber Growth in a Y_2O_3 Stabilized HfO_2 Sample to Which 14 Weight % W Was Added. Dark Field, X600.

3. UO_2-Metal Systems

Preliminary experiments designed to evaluate the compatability of metals other than tungsten as the metal component in UO_2-metal composites have been reported.[1]

Early efforts to produce ordered oxide-metal fiber structures in the UO_2-Ta system were not very successful. Pellets containing 5, 7, and 10 weight % Ta were tested. The major problems encountered were specimen cracking and swelling during preheat and nonhomogeneous internal melting, which was most likely the result of the cracks introduced during preheating. The UO_2-10% Ta pellet revealed the presence of considerably more metallic phase than the other two and the most extensive small regions of UO_2-metal eutectic growth (Figure 19) found, at that time, in any system besides UO_2-W. All three of these specimens contained what appeared to be two-phase oxide structures, particularly in areas that were not well melted. Since W and Ta form a continuous solid solution series, mixtures of these metals were incorporated in UO_2 pellets. A UO_2 pellet containing a 10 weight % mixture addition (Ta:W = 1:3) swelled even more than those containing only Ta additions.

A search of the literature revealed that nitrogen and hydrogen are readily absorbed by tantalum in the temperature range used to preheat and sinter these samples. It appears that the swelling is due to the absorption of N_2, since H_2

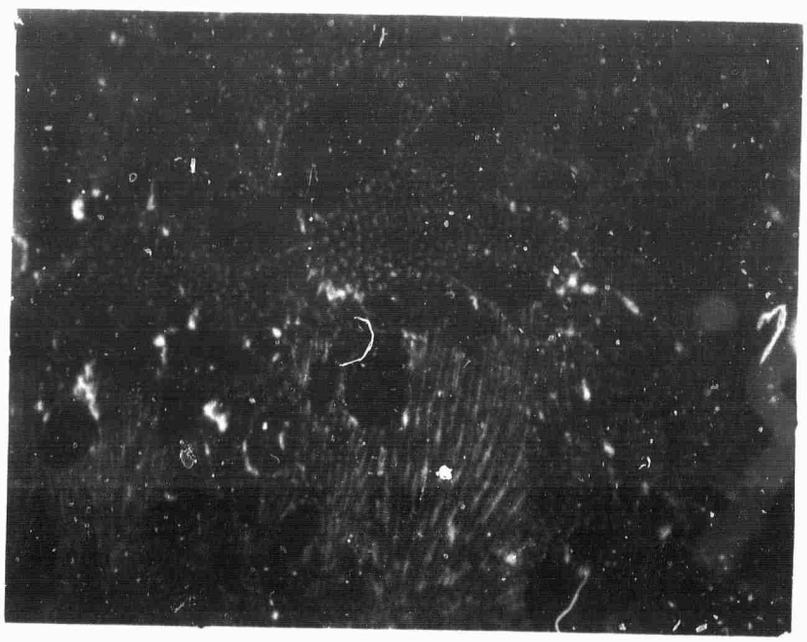

Figure 19. Random Areas of Ordered Oxide-Metal Growth in the System UO_2-Ta. Dark Field, X200.

solubility decreases rapidly with increasing temperatures. It also appears that the W may have acted as a catalyst to promote N_2 solubility in Ta. In an attempt to eliminate these hydriding and nitriding problems, a UO_2-Ta pellet was heated in a He atmosphere using a 4 MHz field. As suspected the pellet could not be heated to its coupling temperature because the He gas ionized, and the resultant arcing terminated the experiment.

Presintering a UO_2-Ta pellet containing 10 weight % Ta to 1400°C for 3 hours in a small vacuum furnace prior to composite growth reduced the amount of porosity in the melted portion of the UO_2-Ta sample and increased the size of the areas of ordered oxide-metal growth.

In an effort to eliminate the large surface area of Ta present in UO_2-Ta pellets formed from powders, a UO_2 pellet was prepared and a hole drilled in its top face. A Ta rod was inserted into this hole to serve as the source of Ta in the melt. However, when this pellet was internally melted, the Ta rod was forced out of the hole either by gas or liquid pressure. Slower heating rates may overcome this problem. Figure 20 shows examples of the oxide-metal structures of the solidified zone around the tantalum rod and suggests the formation of an ordered oxide-metal lamellar structure.

A UO_2-Ta pellet containing a further increase in Ta content up to 12 weight % was preheated to 1500°C and internally melted using a 4 MHz field in a H_2-N_2 atmosphere. The sample

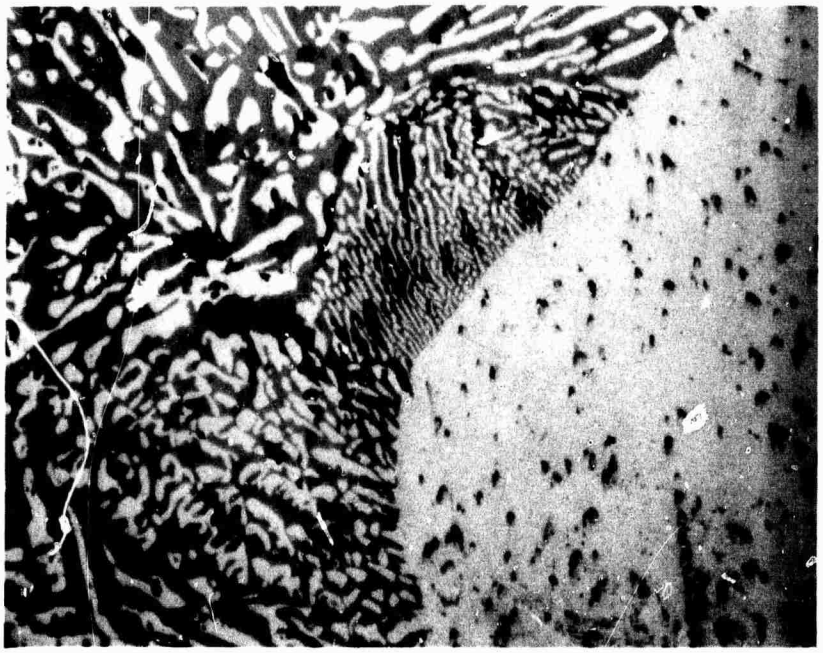

a) Adjacent to Ta Rod.

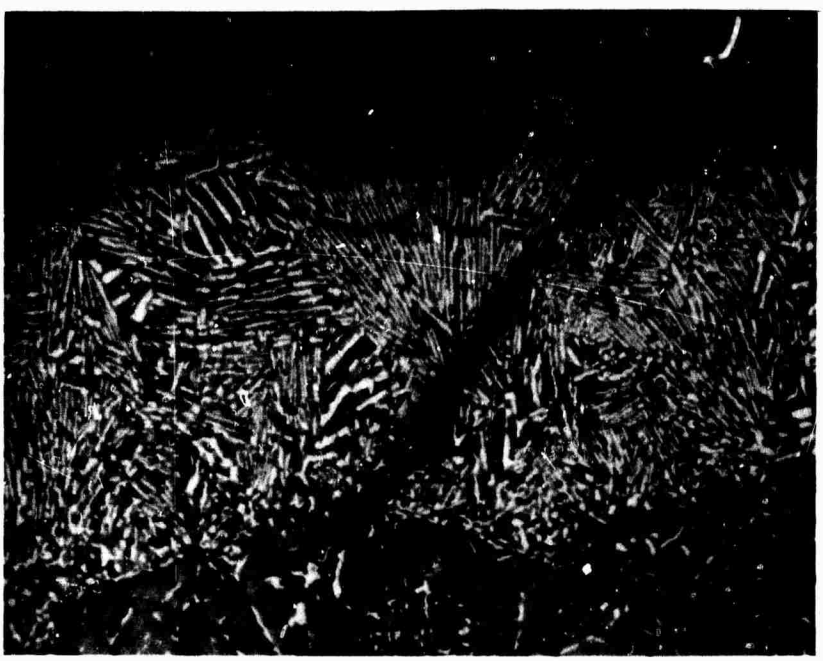

b) Adjacent to Void Cavity.

Figure 20. Solidified Regions of a UO_2-Ta Sample Using a Ta Rod as the Metal Source. High Concentration of Ta Adjacent to Rod Appears Favorable for the Formation of an Oxide-Metal Lamellar Structure. Bright Field, X200.

was lowered in an attempt to produce metallic fibers, but the experiment was cut short after 20 minutes when rf arcing problems shut off the induction generator. A polished section of this pellet revealed the presence of an extensive area of tantalum fiber growth (Figure 21). This result is most noteworthy because Ta is the first metal to be incorporated with UO_2 besides W to produce a well-ordered oxide-metal eutectic structure. The problem of heating Ta in N_2-H_2 atmospheres remains; however, the encouraging composite growth results justify additional work on techniques to circumvent the Ta nitriding and hydriding problem. Systems containing tantalum fibers are of particular interest for superconductivity testing since there are theories which indicate that decreasing conductor size may increase the critical temperature, Tc, where metals become superconducting. Since Ta has a Tc value significantly higher than does W, composites containing Ta would make the theories much easier to test.

UO_2 compositions containing 5 and 10 weight % Nb were also internally melted after preheating to about 1500°C. During melting, temperatures between 1920° and 1940°C were observed through quartz tubes that had deposits on their inside surfaces. Slight cracking occurred during the heating process; and, after cooling, the samples displayed a metallic coating on their surfaces. Examination of the 5% Nb pellet revealed that the metallic phase concentration increased from the center to the exterior of the pellet. In addition to the

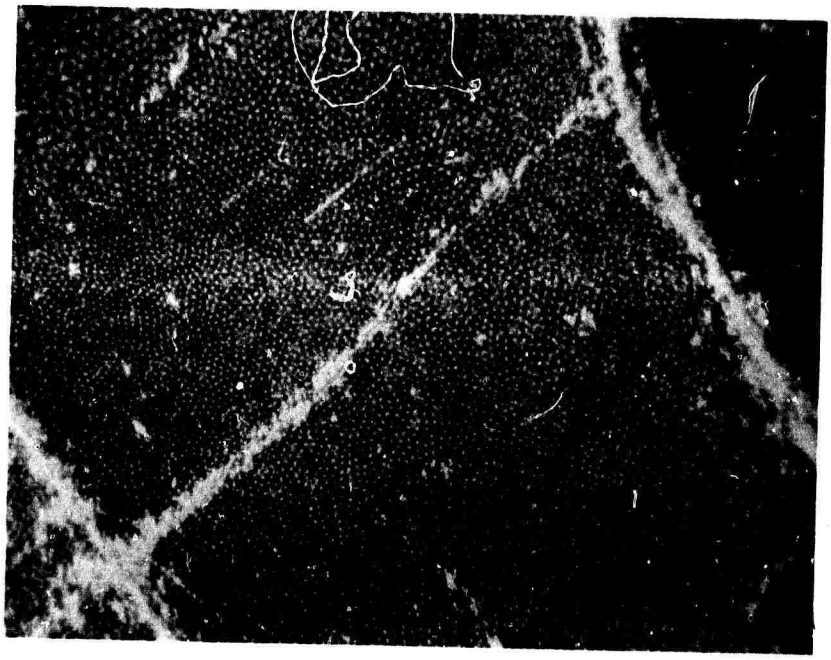

Figure 21. Transverse Section of UO_2-Ta Sample Displaying Extensive Area of "Good" Fiber Growth. Dark Field, X600.

metallic phase there were two gray oxide phases observed. In isolated areas what appeared to be an oxide-oxide ordered structure was observed. The microstructure of the 10% Nb sample was very similar to that of the 5% Nb sample.

The melting points and sublimation points of the metals that have thus far been incorporated in UO_2 are listed below.

Metal	Melting Point °C	Boiling Point °C
Nb	2468	3300
Mo	2620	4800
Ta	3000	5300
W	3380	6000

The fact that Nb has a lower melting point and a significantly higher vapor pressure than the other refractory metals tested is most likely the reason the Nb migrates to the surface of the pellet during the melting process.

SECTION III

STRUCTURAL AND CHEMICAL CHARACTERIZATION OF OXIDE-METAL COMPOSITES

X-ray diffraction techniques and the scanning electron microscope (SEM) have been employed for the routine characterization of oxide-metal composite structures; the SEM is especially useful for the examination of chemically etched specimens. In the following sections the oxide-metal orientations and lattice constants in the system UO_2-W are reviewed, and the initial investigation of the location of impurities and dopants in this system are reported. The recent improvement in quality and size of the stabilized ZrO_2-W composites (described in Section II-B) has warranted examining additional samples in this system. Preliminary orientation information, the effectiveness of various stabilizer additions, and an impurity analysis of stabilized ZrO_2-W samples are also presented.

A. CHARACTERIZATION OF UO_2-W COMPOSITES

In previous reports[1,2] the mutual orientation relationships were determined for several UO_2-W samples. This information can be reduced to three primary relationships, which are presented in order of decreasing frequency of occurrence.

1. $(110)_W // (111)_{UO_2}$ with $[\bar{1}10]_W // [\bar{1}10]_{UO_2}$,

2. $(110)_W // (111)_{UO_2}$ with $[001]_W // [\bar{1}10]_{UO_2}$,

3. $(100)_W // (111)_{UO_2}$ with $[011]_W // [\bar{1}10]_{UO_2}$.

These data show that the most often occurring growth direction of the UO_2 matrix is $[111]$, whereas the tungsten growth is divided between $[110]$ and $[100]$. Thus $\{110\}$ and $\{100\}$ faces are the surfaces on the tungsten tips commonly formed when polishing and etching wafer-shaped samples for emission testing.

Lattice constants, determined by x-ray diffraction methods for UO_2, were generally in the range of values for stoichiometric UO_2 (5.470 Å) regardless of the source of material, growth mode or oxide-to-metal ratio. The lattice constants for tungsten were also quite close to the ASTM value of 3.1648 Å. Here again it is interesting that differences in the growth mode of the specimens apparently have little if any effect on the magnitude of the lattice constants.

The UO_2 and W lattice constants were checked using selected area diffraction (SAD) in the high-voltage electron microscope at the U.S. Steel Research Laboratories. This technique offers the advantage of obtaining an electron diffraction pattern from a single tungsten fiber or within a

single oxide cell (grain), whereas during x-ray diffraction analysis multiple fibers and oxide matrix cells are examined. Figure 22a is an SAD pattern from (110) planes of UO_2. From this and similar patterns a lattice constant of 5.465 Å was obtained. Figure 22b is an SAD pattern for an individual tungsten fiber with a [100] growth direction. A lattice constant of 3.164 Å was obtained from this and similar patterns. These lattice constants are quite close to ASTM values, but they are in both cases lower than the x-ray values. The reason for this apparent difference is not known.

The initial attempts to establish the location of impurities in UO_2-W samples were carried out using conventional microprobe analysis. The first results suggested some segregation of impurities at the cell (grain) boundaries; however, efforts to duplicate this behavior using another as-grown, as well as doped, sample were inconclusive. The reason for this apparent inconsistency is unclear at present, although the beam area in the microprobe may be too large to effectively look at the very small areas necessary to detect compositional variations across cell boundaries, and certainly at the metal-fiber oxide-matrix interface.

Since more spatial resolution was desired for this analysis, the UO_2-W samples were examined in the Stereoscan SEM in conjunction with the energy dispersive detector. The SEM microprobe system has a much finer electron beam than the conventional microprobe equipment; and, consequently, the

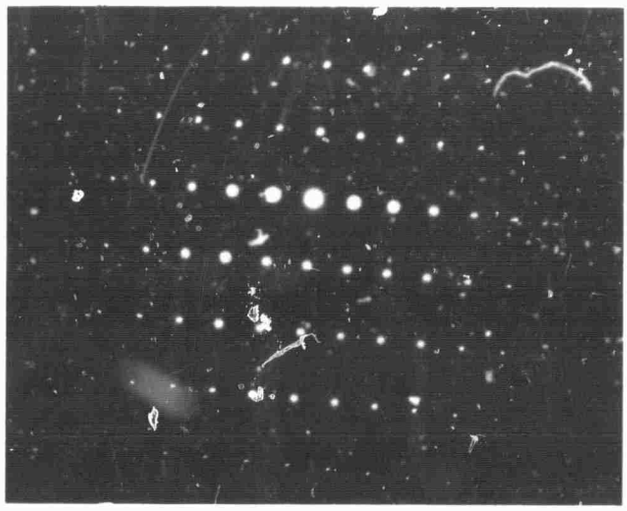

a) UO_2 Matrix with [110] Orientation.

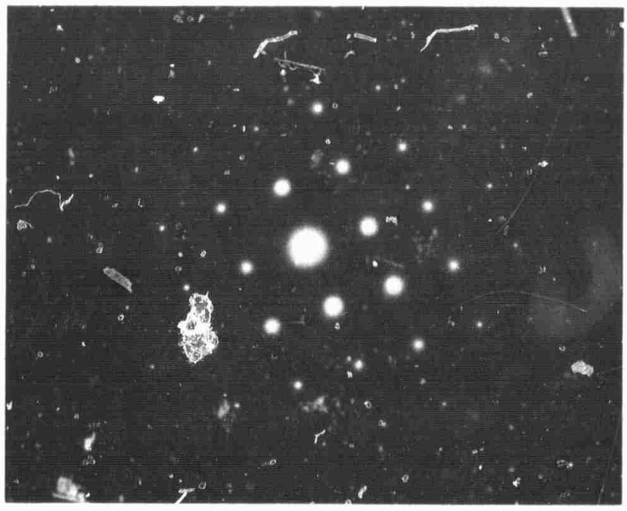

b) Single Tungsten Fiber with [100] Orientation.

Figure 22. Selected Area Diffraction Patterns of a) the UO_2 Matrix, and b) a Single W Fiber from a UO_2-W Sample. Patterns Obtained Using a High Voltage Electron Microscope.

spatial resolution is orders of magnitude better. For example, it was possible to scan across the matrix and then across individual W pins of less than 1μ in diameter. At the same time the specimens can be viewed at magnifications greater than 20,000X; and, under ideal conditions, areas only a few hundred angstroms across can be analyzed.

In the following set of Figures (23 through 28) the first effort to employ the non-dispersive detector of the SEM to obtain composition profiles across a UO_2-W composite sample is presented. In Figure 23 two SEM micrographs of different areas of chemically etched UO_2-W sample (No. 136) are shown. Each viewing area was selected to include a cell (grain) boundary. The lines across the Figures show the locations where the compositic profiles were obtained.

Prior to running the profiles, an overall determination of the x-ray spectrum of the UO_2-W area shown in Figure 23a was obtained and is presented in Figure 24. As expected, the uranium $M_{\alpha,\beta}$ peak is the strongest element in this spectrum. Tungsten shows up with an unresolved $M_{\alpha,\beta}$ doublet and the resolved $L_{\alpha,\beta}$ peaks. The major impurity present is Fe, but its peak height has no direct quantitative significance, because as much as one-third of the peak area may be produced by x-rays which originated at the pole piece of the SEM's third condensor lens. This observation is based on previous experience analyzing other materials in the SEM. Molybdenum is also present in the amount of about 1 weight %. This metal probably

came from impurities in the W or UO_2 powders. Lesser amounts of Si, Al and Ca were also detected; and one small peak suggested the presence of either Au, As or Re.

Figures 25 and 26 show the composition profiles for W and Fe along the lines drawn on the SEM micrographs (Figures 23a and b). These scans were obtained by admitting either the W or Fe signal into the memory of the multichannel analyzer and eliminating the rest of the spectrum by setting the window of the single channel analyzer accordingly. The tungsten pins and the tungsten precipitate in the grain boundary are visible in the form of individual peaks (Figures 25 and 26) and clearly demonstrate the sensitivity of the method. The scans of the major impurity, Fe, indicated that this element is concentrated in the W pins. The tungsten pin circled in the center of Figure 23b was scanned at a magnification of approximately 20,000X and plotted at a magnification of 38,000X in Figure 27a and b. These scans show a steep compositional gradient at the oxide-metal boundary, suggesting a well-defined oxide-matrix metal-pin interface.

A UO_2-10 weight % W sample was doped with 1 weight % Fe_2O_3 and melted in the conventional manner to investigate the influence of impurities on oxide-metal structures. Figures 28a and b show the specimen surface and the corresponding Fe scan along the dark horizontal line across the SEM micrograph. Again the Fe concentration increased in the W pins, and no obvious segregation of Fe in or adjacent to the cell boundary was found.

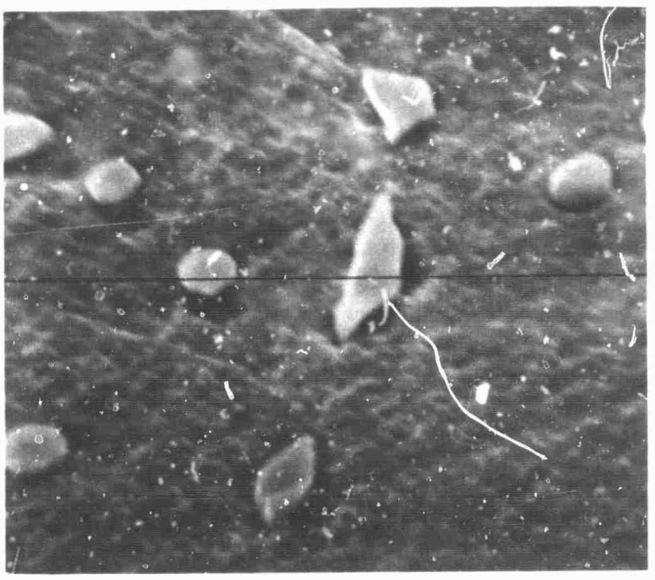

a) Magnification X7,000.

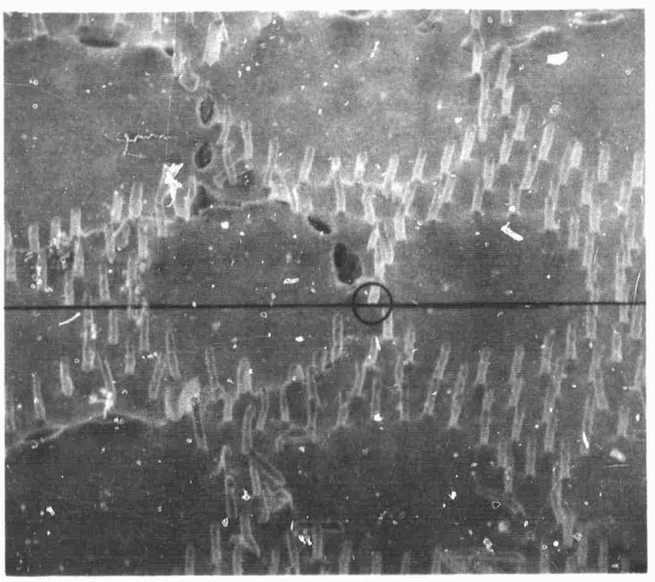

b) Magnification X1,100.

Figure 23. Scanning Electron Micrographs of UO_2-W Sample Showing the Locations Where the Compositional Profiles Were Run.

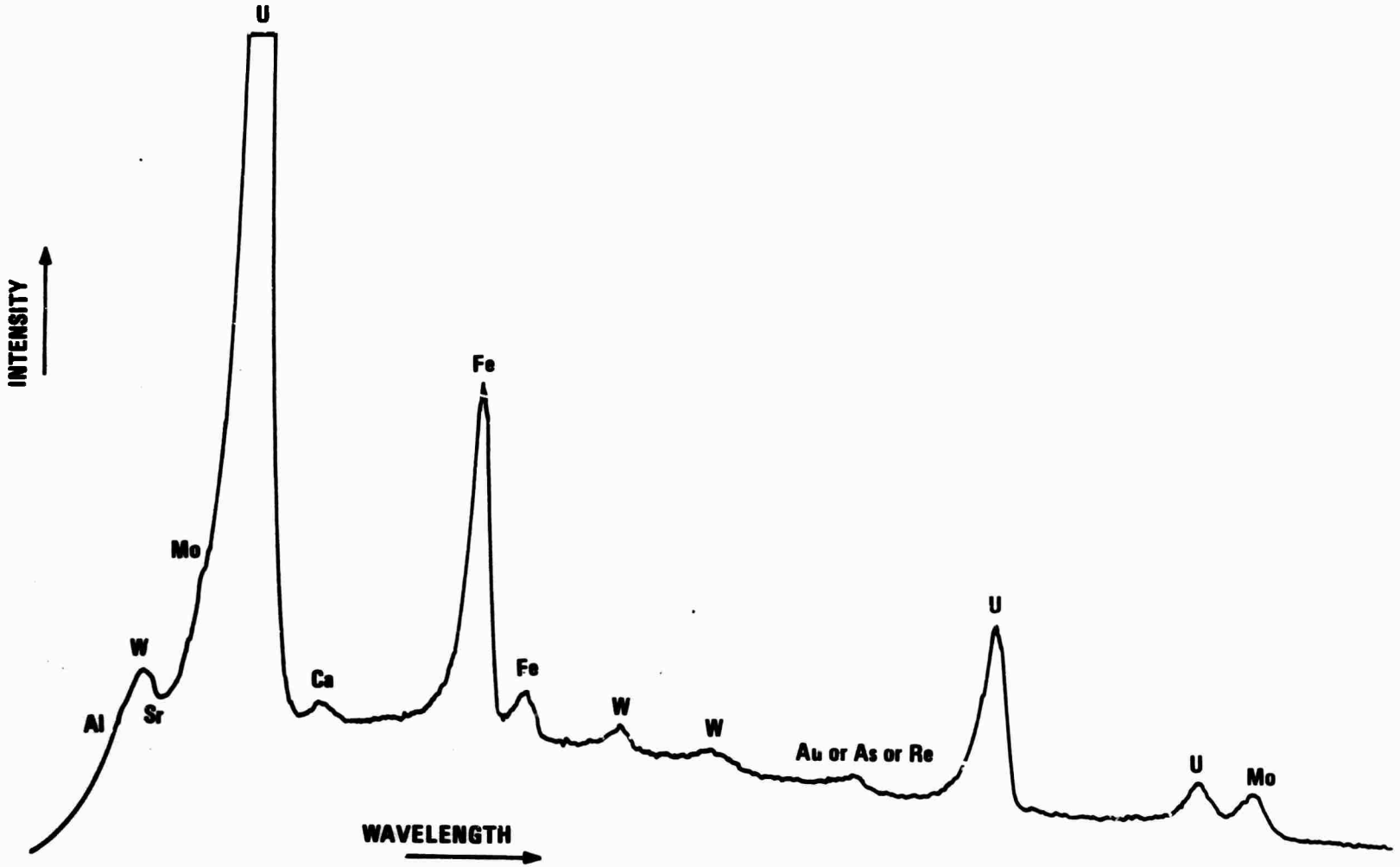

Figure 24. X-ray Spectrum Collected With the Energy Dispersive Detector of the SEM for the Area Shown in Figure 23a.

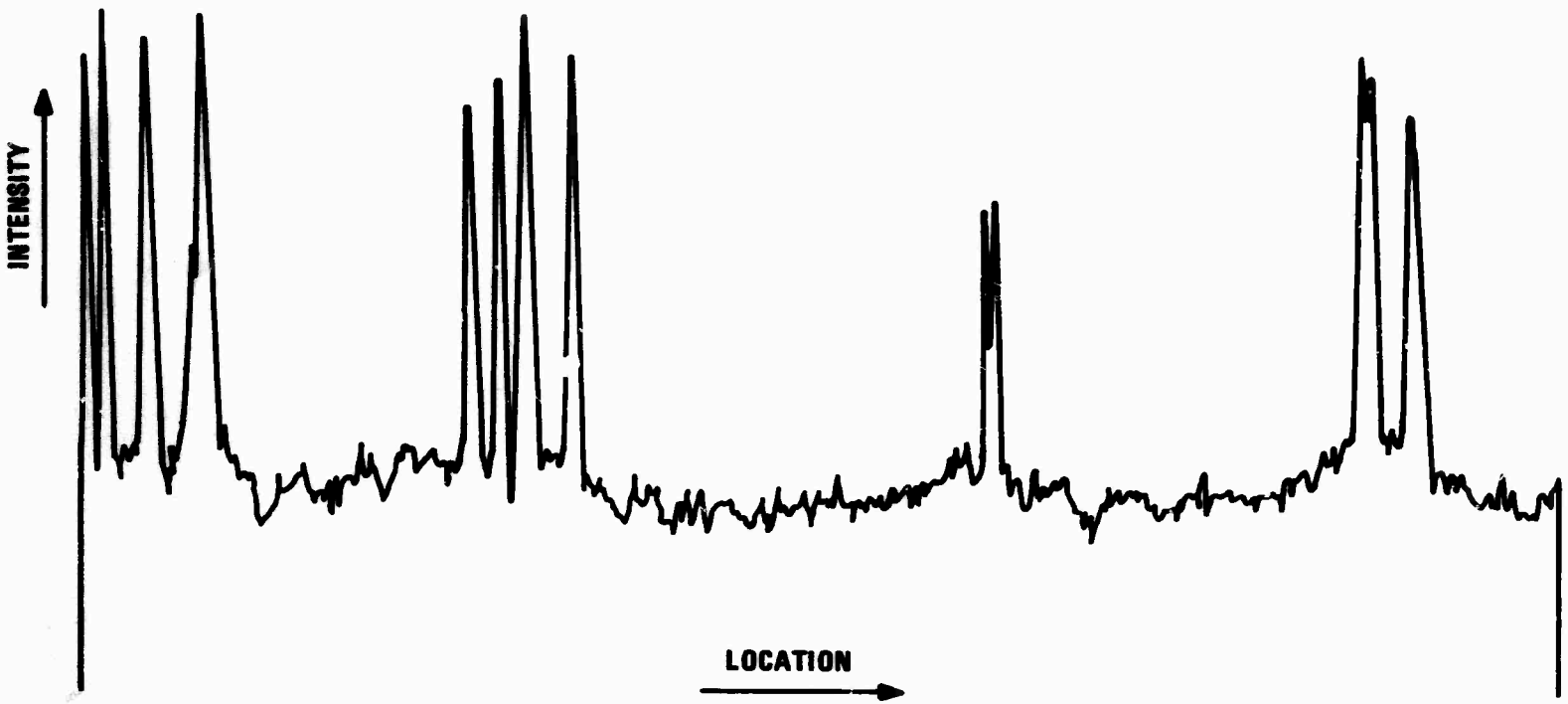

Figure 25. Tungsten Scan Along the Line Shown in Figure 23b. X1,700.

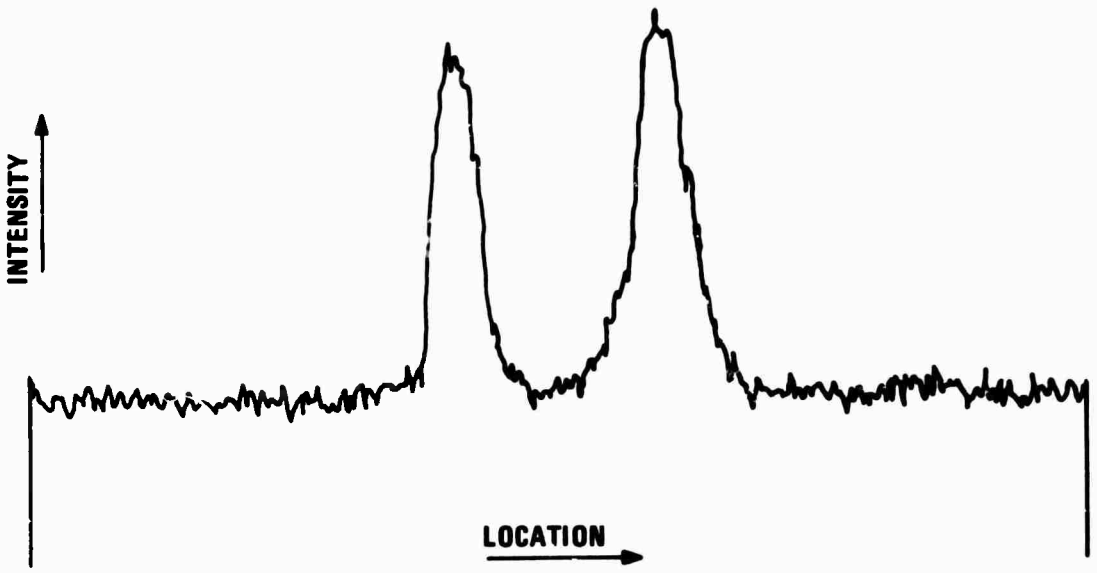

a) W Scan

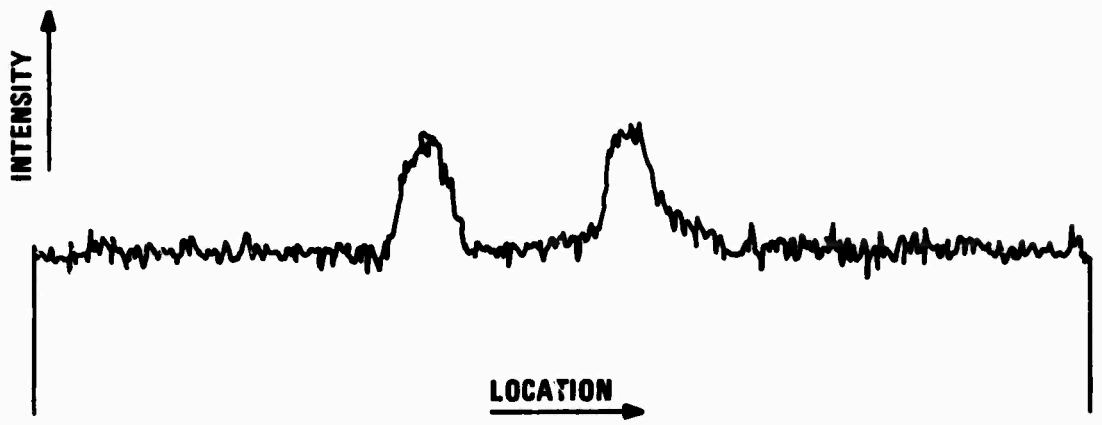

b) Fe Scan

Figure 26. Composition Profiles Along the Line Shown in Figure 23a. X10,000.

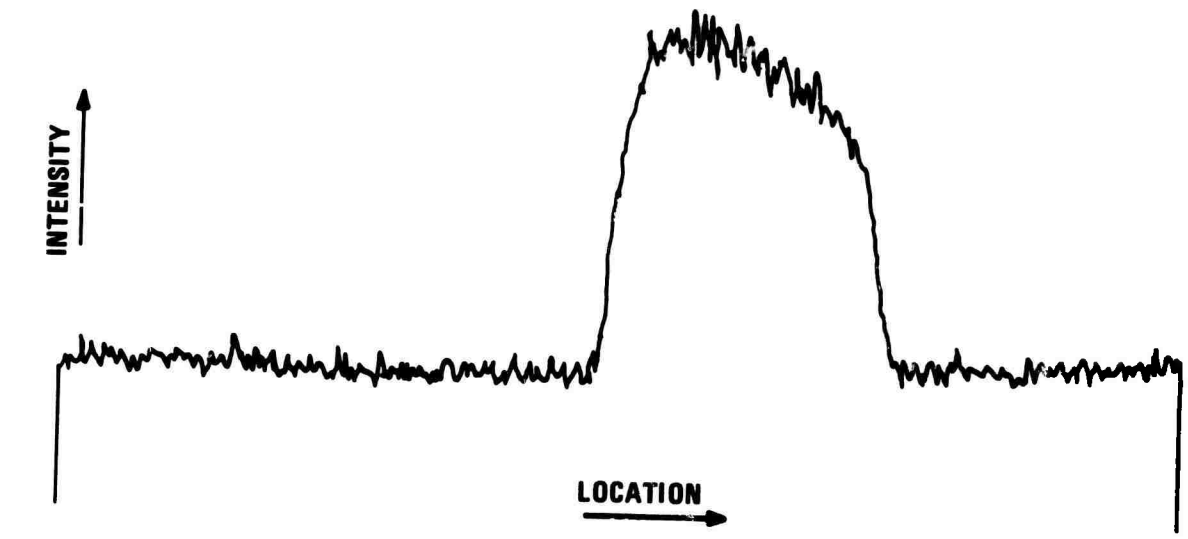

a) W Scan

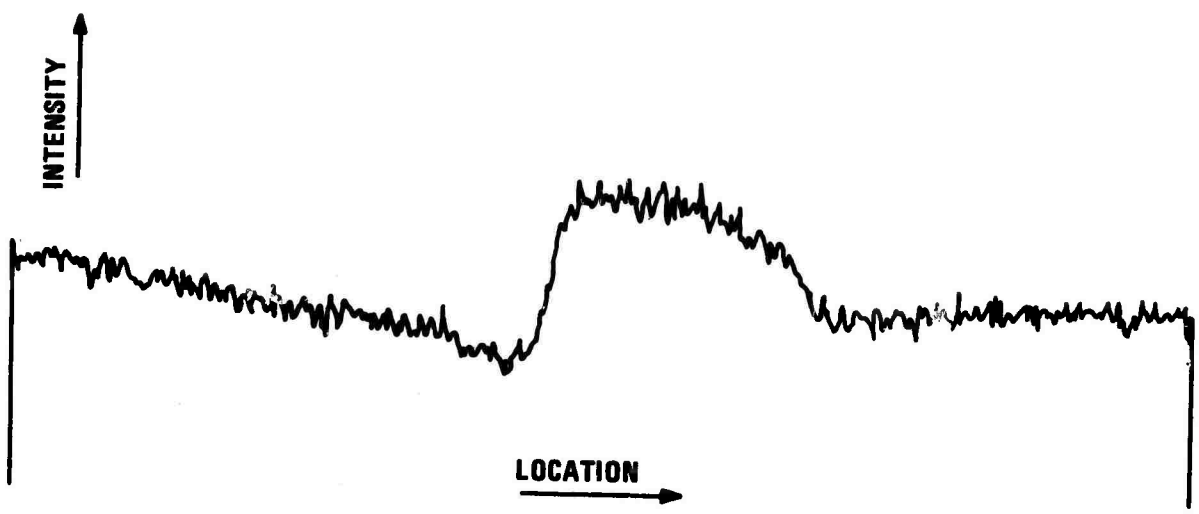

b) Fe Scan

Figure 27. Composition Profiles Across the Single Tungsten Fiber Circled in Figure 23b. X38,000.

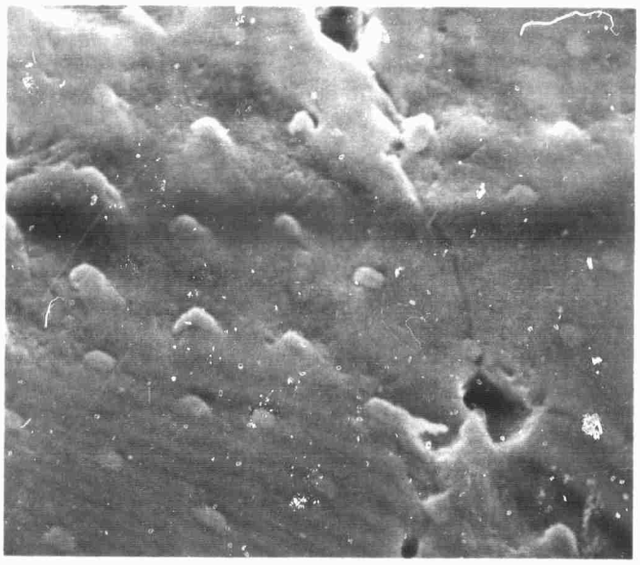

a) SEM Micrograph. X5,000.

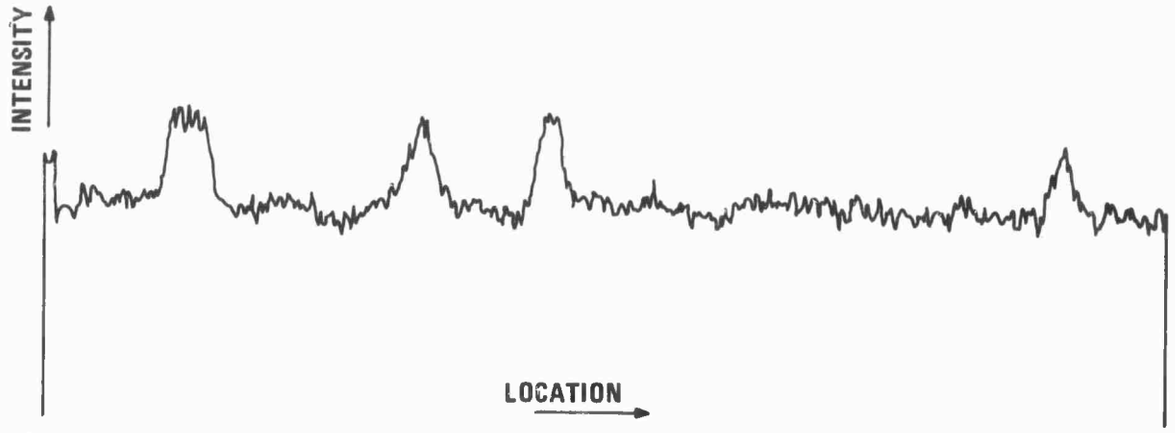

b) Fe Scan Along Dark Line in the SEM Micrograph Above. X8,500.

Figure 28. Iron Profile for UO_2 - 10 Weight % W Sample Doped With 1 Weight % Fe_2O_3.

B. CHARACTERIZATION OF STABILIZED ZrO_2-W COMPOSITES

X-ray diffraction techniques were employed to determine the orientational relationships and lattice parameters in a ZrO_2-7.9 mole % yttria - 10 weight % tungsten specimen grown in the 90% N_2-10% H_2 (by volume) atmosphere and lowered at about 2 cm/hr. The dominant growth direction determined for the zirconia matrix was [111] and for the tungsten [110]; however, for both the oxide and metal a [100] component was present. The major overall mutual oxide-metal orientations found was $(110)_W // (111)_{ZrO_2}$ with $[\bar{1}10]_W // [\bar{1}10]_{ZrO_2}$. Interestingly, this is the same relationship found for the UO_2-W composites. Lattice constants for the stabilized zirconia and tungsten were 5.15 Å and 3.165 Å respectively.

A series of melt experiments were performed using zirconia containing 5, 8, and 10 mole % yttria, and no metal additive, to investigate the effectiveness of Y_2O_3 additions as stabilizers for solidified ZrO_2. The 8 and 10 mole % samples were melted in the 90% N_2-10% H_2 atmosphere using an rf frequency of 3.8 MHz and lowered for crystal growth at about 2 and 5 cm/hr respectively. The sample containing the 5 mole % Y_2O_3 displayed poor melting characteristics and was not lowered because it was impossible to position the molybdenum

post heater for controlled growth and maintain sufficient rf coupling to keep the sample molten. Apparently the lower Y_2O_3 does not impart sufficient electrical conductivity to support internal melting using the normal crystal and composite growth geometry.

A Laue photograph typical of the ZrO_2 stabilized with 8 and 10 mole % Y_2O_3 is shown in Figure 29. The sharp diffraction spots and low intensity background indicates these materials are well crystallized. Additional x-ray analysis using precession and Weissenberg's techniques show the 8 mole % yttria material to be cubic with a lattice constant of 5.16 Å and an x-ray density of approximately 6.10 grams per cm^3. In contrast to the samples containing 8 and 10 mole % Y_2O_3, the Laue photograph of the 5 mole Y_2O_3 sample, Figure 30, displays a very high degree of disorder as is evident from the weak diffraction spots and the high background. This material was so poorly crystallized that it was unsuitable for single crystal x-ray diffraction studies. These results support the literature information[3] indicating that at least 7 mole % yttria is acquired to stabilize zirconia.

Several Y_2O_3 stabilized ZrO_2 specimens were analyzed with the energy-dispersive detector in the SEM. The spectrum shown in Figure 31 is characteristic of the ZrO_2-Y_2O_3 samples studied. The only impurity detected was Fe; and interestingly the Mo, previously found in the UO_2-W specimens, was not detected, suggesting the Mo was an impurity present in the W powder.

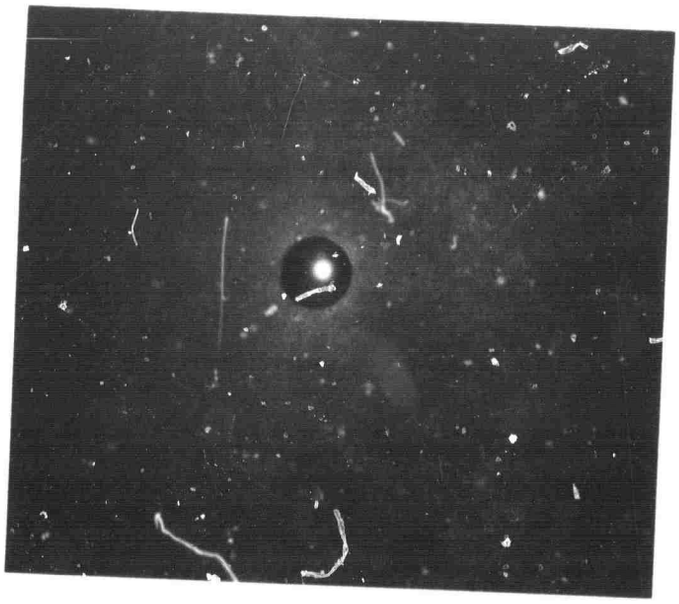

Figure 29. Laue Photograph of ZrO_2 - 10 Mole % Y_2O_3 Indicating Well Crystallized Product.

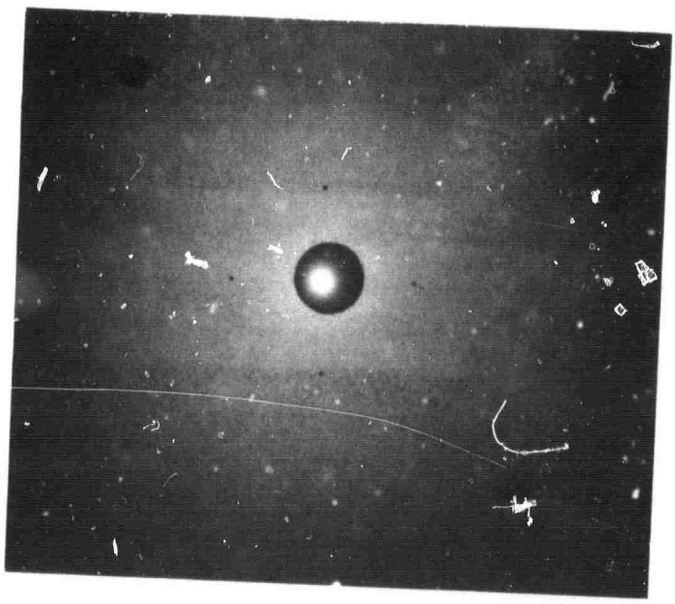

Figure 30. Laue Photograph of ZrO_2 - 5 Mole % Y_2O_3 Showing Poorly Crystallized and Disordered Material.

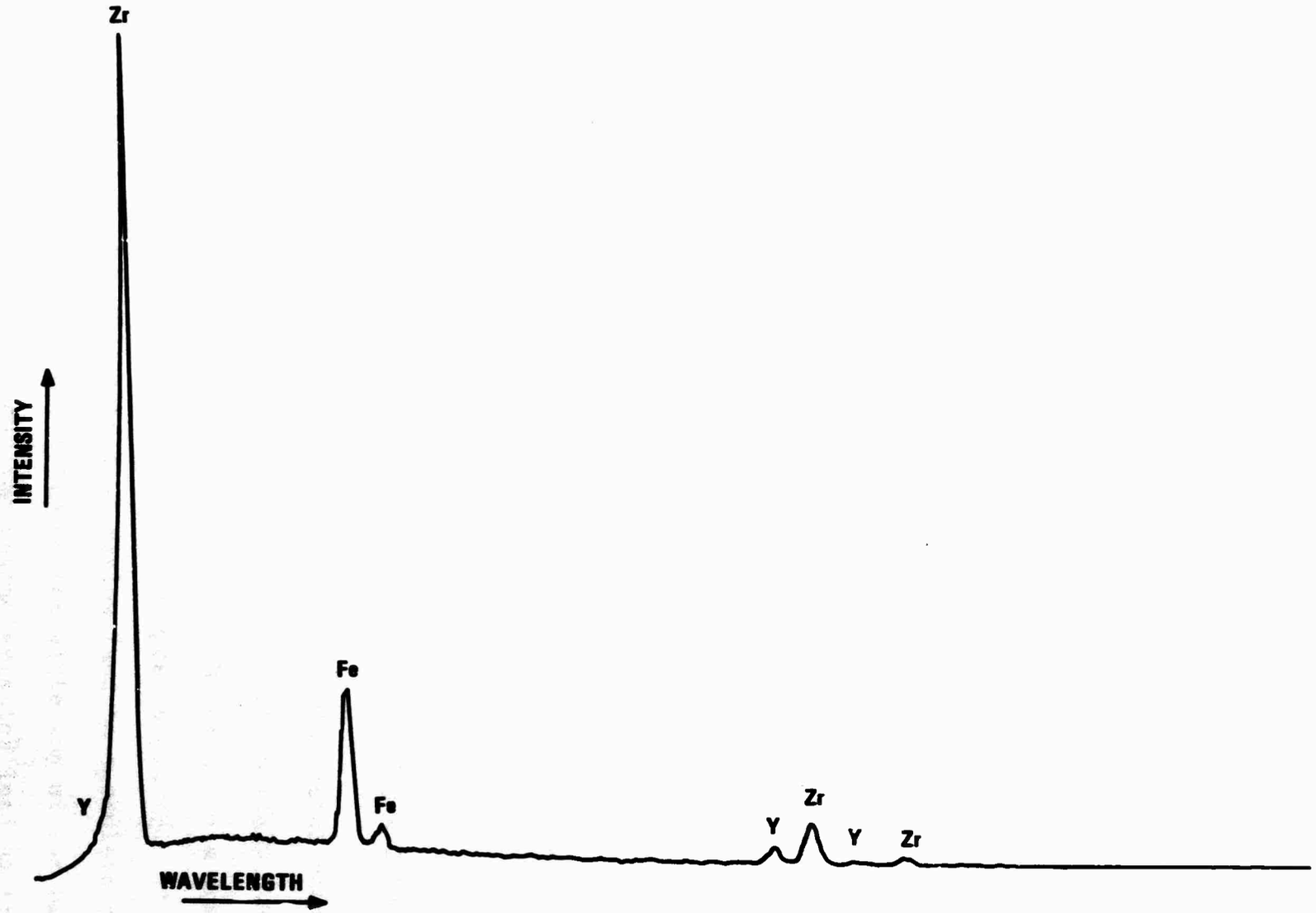

Figure 31. X-ray Spectrum Collected With the Energy Dispersive Detector of the SEM Typical for the Y_2O_3 Stabilized ZrO_2 Samples.

SECTION IV

THE FORMATION OF OPTIMUM EMITTING ARRAYS

The objective of this research area is to study the role growth parameters impart to oxide-metal structures with emphasis on obtaining composite geometries suitable for electronic applications. Previous reports[1,2] have provided information about oxide-metal ratios, growth rates, etc.; and, in Section II-B of this Report, the influence of rf frequency has been emphasized. The effect of variable oxide stoichiometry in the growth of UO_2-W composites is reviewed, and the importance of this parameter is documented with experimental observations. Additional work on the chemical etching of UO_2-W and ZrO_2-W samples designed to expose, shape and remove the W fibers is presented.

A. THE INFLUENCE OF STOICHIOMETRY CHANGES ON UO_2-W GROWTH

During recent work in the growth of oxide-metal composites in the system UO_2-W, it has become increasingly evident that the oxygen-uranium (O:U) ratio of the oxide is a dominant factor controlling successful composite growth. It therefore seems appropriate to review (and to speculate on) the influence of the O:U ratio on the sintering of the oxide-metal pellets, on the coupling characteristics leading to

the formation of an internal molten zone, on the melting and solidification kinetics relative to maintaining a stable molten zone, and on the cooling process needed to obtain large, sound (crack free) specimens. Following this discussion, some experimental results pertinent to this topic are described.

The preparation of oxide-metal rods suitable for composite growth is accomplished by powder fabrication techniques. A UO_2 powder with an O:U ratio in the neighborhood of 2.03 to 2.05 is required because finely divided stoichiometric UO_2 powder is pyrophoric, burning to U_3O_8. During the initial preheating and sintering stage prior to melting the interior of the UO_2-W rods, maintaining an O:U ratio above 2.0 is desirable because of the enhanced sintering characteristics and the increased electrical conductivity (necessary for favorable rf coupling characteristics) of this material. Using a starting oxide with an O:U ratio above 2.1, for example, while suitable for sintering and coupling needs, is most troublesome because the oxygen released leads to excessive oxidation problems with the W metal.

During composite growth a stable oxide-metal melt must be maintained. It is apparent that the evolution of oxygen from the oxide phase would be most disruptive during this step of the growth process. This problem is perhaps more complex than initially appreciated because the oxide phase may go sub-stoichiometric; thus, in atmospheres containing a low oxygen potential (for example H_2), the O:U ratio may go

down well below 2.00, liberating additional quantities of oxygen. Thus it becomes necessary to find and maintain the oxygen partial pressure (using H_2:H_2O ratios) that will maintain the O:U ratio of the melt near 2.00. Experimental work in this area is underway.

In addition to the preceeding problems, the ability of the solidified oxide-metal structure to withstand the large thermal gradients inherent in the internal-zone growth technique may also be sensitive to O:U ratio. It is well documented that hyperstoichiometric uranium dioxide is more plastic than the stoichiometric composition, and hence, less subject to thermal shock problems. Thus it appears desirable to maintain the O:U ratio slightly above 2.00 to prevent cracking of the sample during the cooling cycle.

A number of experimental observations have been made which support the importance of the O:U ratio as a parameter effecting the growth of UO_2-W composites. During the routine growth of UO_2-W samples, a nitrogen-hydrogen ratio of approximately 10:1 volume % has been employed. Frequently these samples show one or more cracks which prevent cutting the specimens to shapes desirable for testing. Increasing the N_2:H_2 ratio up to 20-30:1 (with an accompanying increase in the oxygen potential in the system) has resulted in well grown samples exhibiting infrequent cracking during cooling. Figure 32 shows a cross section of a crack-free UO_2-W composite rod from which a number of wafer shaped samples 0.3 to 0.4mm

Figure 32. Section of a Sound (Crack-Free) UO_2-W Rod Solidified in an Increased Partial Pressure of O_2. X5.

thick have been sliced.

In another experiment a UO_2-10 weight % W rod was melted employing an atmosphere consisting solely of H_2. The rod was initially held for several hours for equilibration with the low oxygen pressure in the H_2 environment prior to lowering the sample at 2 cm/hr for composite growth. Examination of this sample showed no well defined molten zone, and the solidified material was void of metallic fibers. Apparently the continual evolution of oxygen as the oxide phase goes sub-stoichiometric destroys the liquid-solid geometry required for composite growth or disrupts the W solubility in molten UO_2.

Recent attempts to grow UO_2-W structures at fast growth rates, up to several hundred millimeters per hour, in H_2-N_2 atmospheres have been hampered by the apparent kinetic problem of removing the excess oxygen, because increased amounts of the oxide must be melted per unit length of time. In support of these experiments some work was done to characterize the UO_2 powder being used in these growth studies. The determination of the O:U ratio by ignition to U_3O_8 showed the present powder has an O:U ratio of about 2.14. Even after sintering this material in nitrogen to 1400°C, the O:U ratio remained as high as 2.09. These values are much higher than anticipated, as the original specifications showed the O:U ratio for the as-received powder to be 2.05. Apparently the O:U ratio of the powder has been slowly increasing during

storage. It is planned to reprocess the current batch of powder to reduce the O:U ratio down to the more desirable level of 2.03-2.05.

These experimental observations document the necessity to control the O:U ratio of the starting powder closely and monitor the oxygen potential (H_2:H_2O ratio) employed during growth. An alumina oxide hydrometer will be installed to monitor the water vapor between a few and several thousand ppm both in the inlet and exhaust gas sides of the growth chamber. In view of the many complex and interrelated stoichiometry effects it may appear surprising that well-ordered crack-free UO_2-W structures have been obtained at all. In actuality these problems were recognized earlier; however, only recently were the other growth parameters (i.e. oxide: metal ratio, growth rate, rf frequency, etc.) under sufficient control so that specific experiments devoted to the influence of stoichiometry can be undertaken. Most of the comments relative to oxide stoichiometry are applicable to other oxide-metal systems, i.e. ZrO_2-W, HfO_2-W, although the limits of the stoichiometry change occurring in these oxides are usually much less than that exhibited by uranium oxide.

B. SELECTIVE ETCHING STUDIES

In previous reports[1,2] the chemical etching procedures used to expose, shape and recess the W fibers in UO_2-W and ZrO_2-W samples were described. The current work has concentrated on approaches to obtain recessed pins of known depth in UO_2-W samples and the testing of various techniques to expose the W pins by removing the chemically inert ZrO_2 from ZrO_2-W specimens.

For the selective removal of the W pins from a UO_2 matrix an etchant of the following composition was used:

100 ml distilled H_2O
5 g NaOH
15 g $K_3Fe(CN)_6$

Work is in progress to find a technique suitable for measuring the depth to which the pins have been recessed during etching. One approach, while not entirely satisfactory, has provided some initial results. The UO_2-W samples were first carefully polished on both sides using a polishing fixture devised to produce samples with parallel surfaces. After polishing the samples were cleaned in benzene in the ultrasonic cleaner.

Etching was accomplished in the standard apparatus[1] after measuring the thickness of the sample with a micrometer reading to 0.0001inch. The samples were rotated at 22 rpm, and it was found that an etching time of 7 minutes produced holes between 18 to 30μ in depth. The hole depth was determined by repolishing the sample surface until microscopic examination

showed the W fibers were again flush with the surface, then remeasuring the thickness of the sample. The difference in thickness represents the depth to which the pins have been etched.

The principal problems encountered using this technique are related to the polishing and the thickness measurements. It is extremely important to obtain the sample faces as flat and parallel as possible, and this has proven quite difficult. Also, the accuracy is limited since a measurement of one thousandth of an inch (0.001) is 25 microns and reliable thickness measurements of one ten-thousandth of an inch (0.0001), needed to determine the depth to within several microns, are difficult to achieve.

The selective removal of the oxide matrix from stabilized ZrO_2 to expose the tungsten pins has proven to be a formidable task. No chemical etchant has yet been found that dissolves the oxide without attacking the W pins to some extent. Figure 33 shows a sample that was held for 20 minutes in a concentrated Hf (50% Hf) solution at room temperature. The W fibers were exposed slightly and the matrix's surface roughened.

Several preliminary treatments of stabilized ZrO_2-W samples in hot (175-210°C) concentrated phosphoric acid for 20 minutes has also slightly exposed the W pins with perhaps less attack on the tungsten pins. Additional etching work, especially with the phosphoric acid using longer etching times, is planned.

Ion milling was tried as an alternative approach to mechanically remove the oxide without destroying the tungsten. Figure 34 shows the resultant hilloch structure of the ZrO_2 matrix and again only the slight protrusion of the tungsten pins.

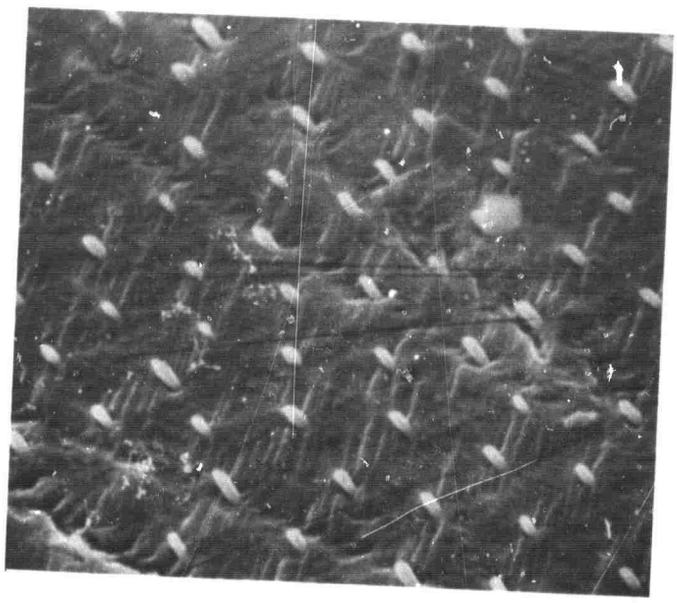

Figure 33. A Y_2O_3 Stabilized ZrO_2-W Sample Etched in Concentrated HF for 20 Minutes Showing Slight Exposure of the W Pins. SEM Micrograph, X6,200.

Figure 34. Ion Milled Stabilized ZrO_2-W Sample Displaying Hilloch Structure. SEM Micrograph, X10,000.

SECTION V

FIELD EMISSION THEORY

In a previous study[5] the calculation of the electrostatic potential surrounding a square array of charged surface states on an insulating dielectric substrate was determined. The potential was determined by imaging the surface states through a grounded conducting planar anode and by solving the appropriate Poisson equation by using a harmonic mode expansion of the potential in each cell which consisted of a surface state and its image. The resulting undetermined coefficients in the series expansions were computed by applying the Neumann boundry conditions at every common cell interface. The form of the answer was a double Fourier series. Certain special points of interest in each cell, e.g. points of maximum and minimum potential, which could be summed easily under certain spacing requirements, were sufficient to sketch a profile of the potential everywhere inside the interelectrode space as a function of the dielectric/anode spacing and the pin spacing. This study was also expanded to include a dielectric discontinuity at the surface.

In the present study the charged surface states have been replaced with the finite conducting pins of the actual device, which protrude out of the insulating dielectric substrate.

Therefore, an attempt is being made to generalize the previous model to include the important parameters of the pin itself, i.e. pin shape, pin height and pin cross-sectional area, which were not present in the earlier model. This generalization of the model severely complicates the problem and necessitates the use of several approximations in order to obtain an answer in a useable form.

A. THEORETICAL ANALYSIS

A theoretical analysis of the field emission anticipated from a planar array of conducting metallic pins uniformly embedded in an insulating dielectric substrate is being undertaken. The potential distribution within the interelectrode space is being developed as a function of its geometrical and electrical parameters including the pin shape, the pin height, the pin cross-sectional area, the pin spacing, the pin/anode spacing, and the applied boundary potentials. The electric field strength in the neighborhood of each individual pin can then be calculated by taking the negative gradient (negative directional derivative normal to the pin surface) of the potential function. Finally, the electric field strength can be used in the appropriate quantum mechanical formula for tunnelling through a surface potential barrier to obtain the surface current density on each pin, which can be integrated over the pin surfaces to find the total current

emitted per pin. The total current emitted by the array is simply obtained by summing the individual currents of the several pins. Once the potential distribution in the interelectrode space of the device has been determined, it will be a simple matter to carry this analysis to its conclusion and to assess and to optimize the parameters which control the electron emission properties of the device.

Since the determination of the potential distribution in the interelectrode space is the most difficult part of the calculations, the initial research has been concentrated in this area. This report describes the important initial step of determining the potential distribution in the interelectrode space; only after the potential distribution can be developed for a reasonably general model will the remaining steps of the analysis be undertaken.

1. Model

A theoretical model has been developed based on a SEM picture of a single pin at X22,000 showing one of the possible growth modes available (see Figure 35). It is assumed that each pin has a uniform rectangular cross section d_x, d_y and a height h. The tip of each pin is assumed to be flat. In terms of a rectangular coordinate system, the array of pins is orientated in the x-y plane with the pins alined in the z direction. The pins are embedded in a dielectric substrate whose upper surface is planar and parallel to the x-y plane.

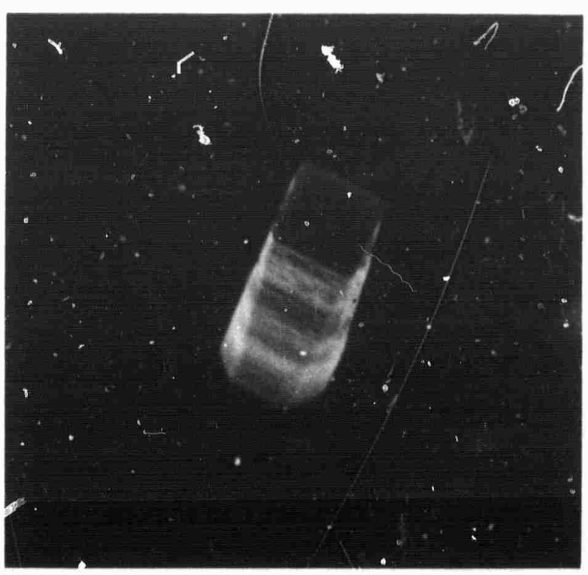

Figure 35. Single Tungsten Pin Showing One of the Many Growth Modes.

The pin distribution is assumed to be uniform with a spacing x_o, y_o. A grounded planar anode is assumed to be a distance z_o above and parallel to the x-y plane. The pins and the anode are assumed to be good conductors; the dielectric substrate is assumed to be a poor conductor. The pin dimensions d_x, d_y, the pin spacings x_o, y_o, the pin height h, the pin/anode spacing z_o, and the applied boundary potential V_o are parameters in this study.

Notice that the boundary potential V_o is applied to the backside of the dielectric substrate. When the pins draw current, the potential of the pin tips V_+ will be reduced somewhat below the steady state value V_o. Similarly, the potential of the dielectric substrate V_- will be reduced somewhat below the steady state value V_o. Due to the difference in conductivities of the two materials, these values will not be the same. It is also assumed that due to the large potential difference which usually exists across the interelectrode space, the resulting electric field strength is strong enough to remove any space charge which would otherwise accumulate above the pins.

2. Analysis

The initial analysis is made with two-dimensional pins only. Some of the assumptions involved in the mathematical model are being checked by comparison with a purely numerical solution. If the assumptions prove valid, then the analytical

method can be extended to the general three-dimensional case. A two-dimensional numerical solution has been developed; a three-dimensional numerical solution is being developed.

The two-dimensional analysis is divided into two parts involving different cross-sectional cuts of the general three-dimensional model. If the surface of the substrate matrix is used as a reference plane, then the problem divides easily into a parallel and perpendicular cross-sectional cut of the model. For case 1, the cross-sectional cut is taken parallel to the reference plane and through the tips of the pins. This produces a top view of the pins, looking down on the pin distribution (see Figure 36). This analysis considers the cross-sectional area of the pins, the pin spacings, and the pin/anode spacing, but neglects the height of the pins. Note that the potential distribution between the tips of the pins is assumed to be uniform at the value V_-. The actual potential distribution between the pins is a smoothly varying function of the distance between the pins with a minimum halfway between the pins. This smoothly varying potential distribution has been approximated by a square well potential distribution. The theory can be easily modified to consider this case when an approximate form for the potential distribution between the pins becomes known, e.g. from a numerical solution of the problem. Also note that this case is similar to the earlier analysis.

For case 2, the cross-sectional cut is perpendicular to

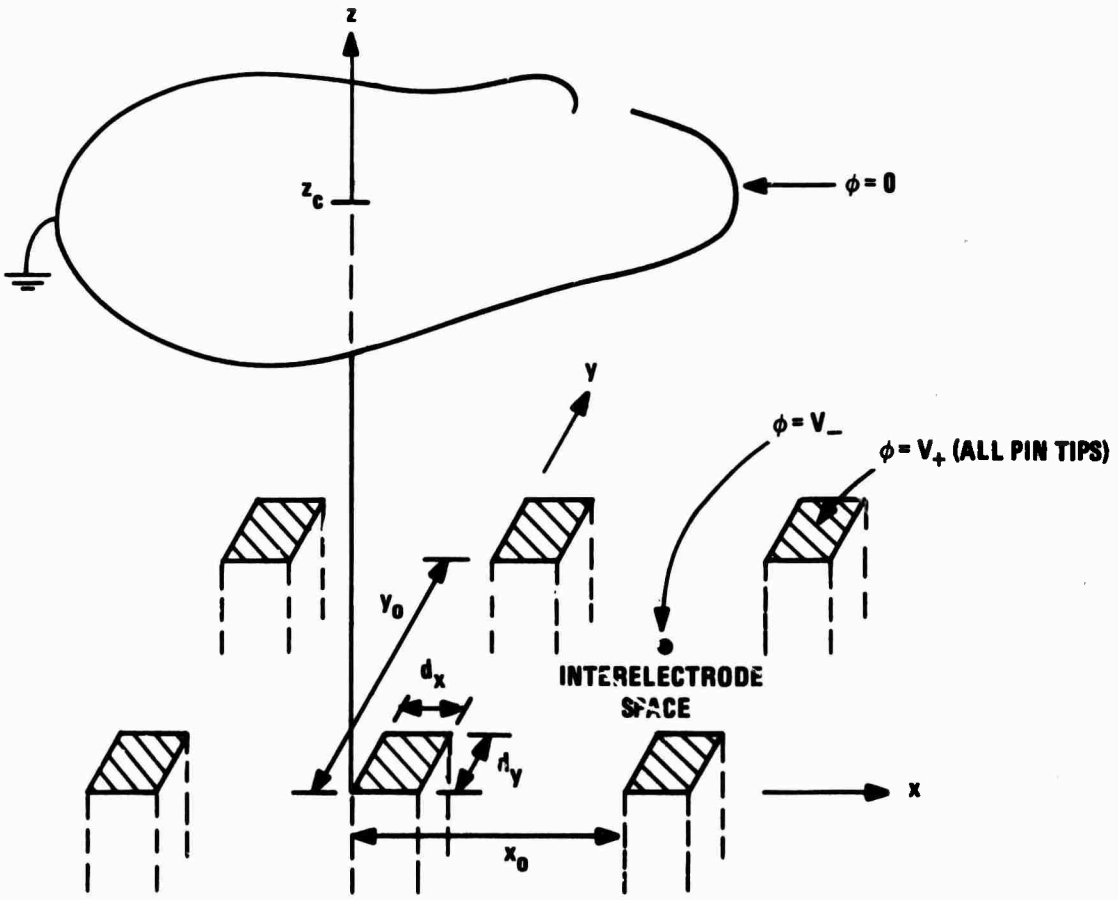

Figure 36. Electrode Geometry for Electric Potential Calculation, Case I.

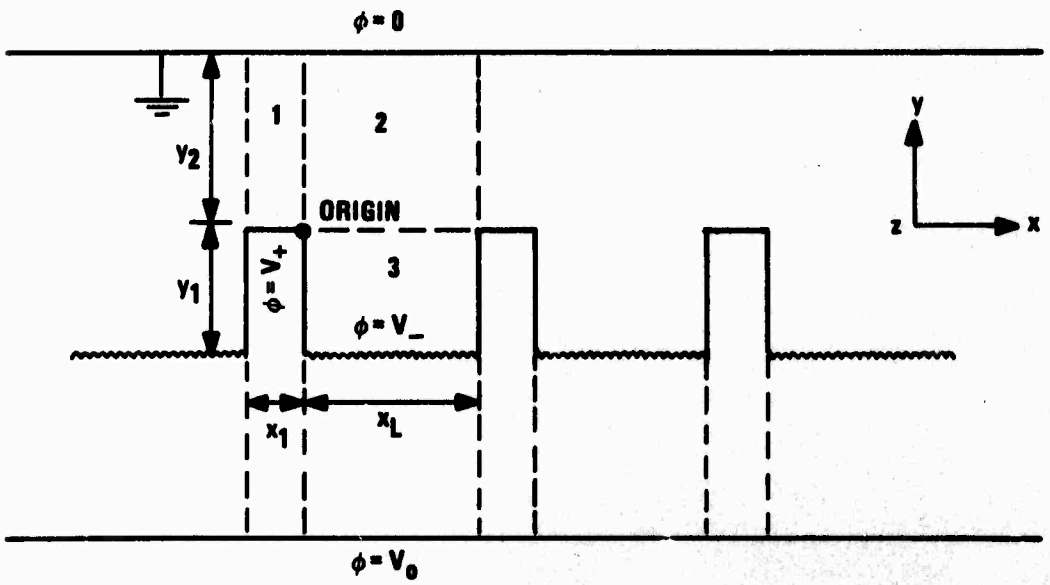

Figure 37. Electrode Geometry for Electric Potential Calculation, Case II.

the reference plane and intersects any row of pins through the center of each pin cross section. This produces a side view of the pins, looking across the pin distribution (see Figure 37). This analysis considers the pin height, the pin/anode spacing, and the pin spacings; but, it neglects the cross-sectional area of the pins.

3. Case I - Top View of Array

For static conditions (with negligible space charge), the scalar potential ϕ must satisfy the Laplace equation

$$\nabla^2 \phi = 0$$

everywhere within the interelectrode space shown in Figure 36. On the surface $z=z_o$, the potential must reduce to zero; on the surface $z=0$, the potential is equal to the specified values of $V(x,y)$, as shown in Figure 36.

In a rectangular coordinate system,

$$\nabla^2 \equiv \frac{\partial^2}{\partial x^2} + \frac{\partial^2}{\partial y^2} + \frac{\partial^2}{\partial z^2}$$

and the Laplace equation decomposes to

$$\left(\frac{\partial^2}{\partial x^2} + \frac{\partial^2}{\partial y^2} + \frac{\partial^2}{\partial z^2}\right)\phi = 0$$

If the potential is written in the product form

$$\phi = XYZ$$

where the eigenvalues X, Y, Z are functions of x, y, z, respectively, only then the Laplace equation separates into the three simpler equations

$$\left(\frac{\partial^2}{\partial x^2} + k_x^2\right)X = 0$$

$$\left(\frac{\partial^2}{\partial y^2} + k_y^2\right)Y = 0$$

$$\left(\frac{\partial^2}{\partial z^2} + k_z^2\right)Z = 0$$

where the eigenvalues k_x, k_y, k_z (to be determined) must satisfy the additional restriction

$$k_x^2 + k_y^2 + k_z^2 = 0$$

The eigenfunctions which satisfy the above equations are either the circular or hyperbolic trigonometric functions, depending on whether the eigenvalues are real or imaginary.

To satisy the boundary conditions shown in Figure 36 it will be convenient to assume that the x and y eigenvalues are imaginary, i.e.

$$k_x \equiv ik_x'$$

$$k_y \equiv ik_y'$$

where k_x' and k_y' are real and

$$i \equiv \sqrt{-1}$$

The most general form for the potential is, therefore,

$$\phi = \left\{a \begin{matrix}\sin\\ \cos\end{matrix} k_x'x\right\}\left\{b \begin{matrix}\sin\\ \cos\end{matrix} k_y'y\right\}\left\{c \begin{matrix}\sinh\\ \cosh\end{matrix} k_z z\right\}$$

where a,b,c are arbitrary constants (to be determined).

To satisfy the periodic boundary conditions in the x-y plane at z=0, the circular sine functions will be sufficient if the eigenvalues k_x', k_y' are chosen to be

$$k_x' = \frac{m\pi}{x_o} \qquad m = 1,2,3,\ldots$$

$$k_y' = \frac{n\pi}{y_o} \qquad n = 1,2,3,\ldots$$

From the restriction on the eigenvalues

$$k_z = \sqrt{k_x'^2 + k_y'^2} = \sqrt{\left(\frac{m\pi}{x_o}\right)^2 + \left(\frac{n\pi}{y_o}\right)^2}$$

To satisfy the boundary condition at $z=z_o$, the hyperbolic sine function will be sufficient if the argument is chosen to be $z-z_o$ or z_c-z.

It is found that a linear combination of the solutions discussed above for the various values of m and n must be used in order to satisfy the remaining boundary condition at z=0. Therefore, the required form for the potential is

$$\phi = \sum_{m=1}^{\infty}\sum_{n=1}^{\infty} C_{mn} \sin\frac{m\pi}{x_o}x \sin\frac{n\pi}{y_o}y \sinh\sqrt{\left(\frac{m\pi}{x_o}\right)^2 + \left(\frac{n\pi}{y_o}\right)^2}\,(z_o - z)$$

where the arbitrary constants are lumped into the constant C_{mn}.

Applying the remaining boundary condition at z=0 gives

$$v(x,y) = \phi\big|_{z=0} = \sum_{m=1}^{\infty}\sum_{n=1}^{\infty} C_{mn} \sin\frac{m\pi}{x_o}x \sin\frac{n\pi}{y_o}y \sinh\sqrt{\left(\frac{m\pi}{x_o}\right)^2 + \left(\frac{n\pi}{y_o}\right)^2}\,z_o$$

This is recognized as a double Fourier Series of the potential in the x-y plane. The constant C_{mn} can be determined explicitly with the use of the orthoganality conditions on the circular sine functions.

$$C_{mn} = \frac{1}{x_o y_o} \frac{1}{\sinh \sqrt{\left(\frac{m\pi}{x_o}\right)^2 + \left(\frac{n\pi}{y_o}\right)^2}\, z_o} \int_{-x_o}^{+x_o} dx \int_{-y_o}^{+y_o} dy\ V(x,y) \sin \frac{m\pi}{x_o} x \sin \frac{n\pi}{y_o} y$$

After performing the indicated integrations over the x-y plane

$$C_{mn} = \frac{V_+ - V_-}{mn\pi^2} \frac{1}{\sinh \sqrt{\left(\frac{m\pi}{x_o}\right)^2 + \left(\frac{n\pi}{y_o}\right)^2}\, z_o} C_m(x_o, d_x)\ C_n(y_o, d_y)$$

where

$$C_m(x_o, d_x) \equiv 1 - \cos \frac{m\pi}{x_o} d_x - \cos \frac{m\pi}{x_o} (x_o - d_x) + \cos m\pi$$

$$C_n(y_o, d_y) \equiv 1 - \cos \frac{n\pi}{y_o} d_y - \cos \frac{n\pi}{y_o} (y_o - d_y) + \cos n\pi$$

Therefore, the total potential is given by

$$\phi = \sum_{m=1}^{\infty} \sum_{n=1}^{\infty} \frac{V_+ - V_-}{mn\pi^2} C_m(x_o, d_x)\ C_n(y_o, d_y) \sin \frac{m\pi}{x_o} x \sin \frac{n\pi}{y_o} y \frac{\sinh \sqrt{\left(\frac{m\pi}{x_o}\right)^2 + \left(\frac{n\pi}{y_o}\right)^2}\, (z_o - z)}{\sinh \sqrt{\left(\frac{m\pi}{x_o}\right)^2 + \left(\frac{n\pi}{y_o}\right)^2}\, z_o}$$

The above constants C_m and C_n implicitly contain information about the pin geometries and the pin spacings.

4. Case II - Side View of Array

For static conditions (with negligible space charge), the scalar potential ϕ must satisfy the reduced Laplace equation

$$\nabla_t^2 \phi = 0$$

everywhere within the interelectrode space shown in Figure 37. On the surface $y = y_o$, the potential must reduce to zero; on the pin surfaces, the potential is equal to V_+; on the substrate matrix, the potential is equal to V_- (note: $V_+ \neq V_-$).

In a rectangular coordinate system,

$$\nabla_t^2 \equiv \frac{\partial^2}{\partial x^2} + \frac{\partial^2}{\partial y^2}$$

and the reduced Laplace equation decomposes to

$$\left(\frac{\partial^2}{\partial x^2} + \frac{\partial^2}{\partial y^2}\right)\phi = 0$$

If the potential is written in the product form

$$\phi = XY$$

where the eigenfunctions X, Y are functions of x, y respectively, only then the reduced Laplace equation separates into the two simpler equations

$$\left(\frac{\partial^2}{\partial x^2} + k_x^2\right)X = 0$$

$$\left(\frac{\partial^2}{\partial y^2} + k_y^2\right)Y = 0$$

where the eigenvalues k_x, k_y (to be determined) must satisfy the additional restriction

$$k_x^2 + k_y^2 = 0$$

The eigenfunctions which satisfy the above equations are either the circular or hyperbolic trigonometric functions, depending on whether the eigenvalues are real or imaginary. Therefore,

the potential has either of the forms

$$\phi = \left\{ a \begin{matrix} \sin \\ \cos \end{matrix} k'_x x \right\} \left\{ b \begin{matrix} \sinh \\ \cosh \end{matrix} k_y y \right\} \qquad k_x = ik'_x$$

or

$$\phi = \left\{ a \begin{matrix} \sinh \\ \cosh \end{matrix} k_x x \right\} \left\{ b \begin{matrix} \sin \\ \cos \end{matrix} k'_y y \right\} \qquad k_y = ik'_y$$

To continue, the interelectrode space is divided into three regions labled 1, 2, 3, as shown in Figure 37. The potential within each region will be found by superposition, and the various solutions will then be matched to the appropriate boundary conditions. It is necessary to require that the potential and its normal derivative be continuous over the common interfaces of the various regions.

Each region with four non-zero boundary potentials can be decomposed into four cells. Each cell has only one non-zero boundary potential and the remaining sides grounded. For example, consider the following cell in which the upper surface is held at a fixed potential V_o, and the remaining sides are grounded.

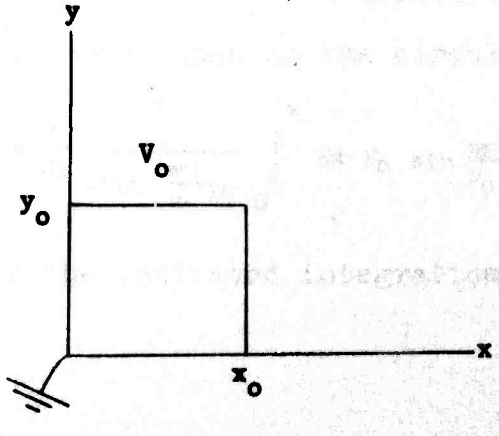

To satisfy the boundary conditions on the x=0 and the y=0 surfaces, it is necessary to assume that the potential inside the cell is of the form

$$\phi = C \sin kx \sinh ky$$

where C and k are to be determined.

To satisfy the boundary condition on the $x=x_o$ surface,

$$k = \frac{m\pi}{x_o} \qquad m = 1,2,3, \ldots$$

To satisfy the boundary condition on the $y=y_o$ surface, it is necessary to use a linear combination of the solutions discussed above for the various values of m. Therefore, the required form for the potential is

$$\phi = \sum_{m=1}^{\infty} C_m \sin \frac{m\pi}{x_o} x \sinh \frac{m\pi}{x_o} y$$

where the arbitrary constant C_m is a function of m.

Applying the remaining boundary condition at $y=y_o$ gives

$$V_o = \phi\Big|_{y=y_o} = \sum_{m=1}^{\infty} C_m \sin \frac{m\pi}{x_o} x \sinh \frac{m\pi}{x_o} y_o$$

This is recognized as a Fourier Series of the potential at $y=y_o$. The constant C_m can be determined explicitly with the use of the orthoganality conditions on the circular sine function

$$C_m = \frac{2}{x_o} \frac{1}{\sinh \frac{m\pi}{x_o} y_o} \int_0^x dx\, V_o \sin \frac{m\pi}{x_o} x$$

After performing the indicated integration over the x axis

$$C_m = \begin{cases} 0 & m \text{ even} \\ \dfrac{4V_0}{m\pi} \dfrac{1}{\sinh \dfrac{m\pi}{x_0} y_0} & m \text{ odd} \end{cases}$$

Therefore, the potential inside the cell is given by

$$\phi = \sum_{\substack{m \\ \text{odd}}} \frac{4V_0}{m\pi} \sin \frac{m\pi}{x_0} x \; \frac{\sinh \dfrac{m\pi}{x_0} y}{\sinh \dfrac{m\pi}{x_0} y_0}$$

The solution for the other three cells can be obtained from the above solution by an interchange of axis.

By superposition, the appropriate form for the potential in each region is given by

Region 1

$$\phi_1 = a \sin \frac{\pi}{y_2} y \; \sinh \frac{\pi}{y_2} x + b \sin \frac{\pi}{y_2} y \; \sinh \frac{\pi}{y_2} (x+x_1) - \sum_{\substack{m \\ \text{odd}}} \frac{4V_+}{m\pi} \sin \frac{m\pi}{x_1} x \; \frac{\sinh \dfrac{m\pi}{x_1} (y-y_2)}{\sinh \dfrac{m\pi}{x_1} y_2}$$

Region 2

$$\phi_2 = A \sin \frac{\pi}{y_2} y \; \sinh \frac{\pi}{y_2} x + B \sin \frac{\pi}{y_2} y \; \sinh \frac{\pi}{y_2} (x-x_2) + C \sin \frac{\pi}{x_2} x \; \sinh \frac{\pi}{x_2} (y-y_2)$$

Region 3

$$\phi_3 = C \sin \frac{\pi}{x_2} x \; \sinh \frac{\pi}{x_2} (y+y_1)$$

$$- \sum_{\substack{i \\ \text{odd}}} \frac{4V_-}{i\pi} \sin \frac{i\pi}{x_2} x \; \frac{\sinh \dfrac{i\pi}{x_2} y}{\sinh \dfrac{i\pi}{x_2} y_1}$$

$$+ \sum_{\substack{j \\ \text{odd}}} \frac{4V_+}{j\pi} \sin \frac{j\pi}{y_1} y \; \frac{\sinh \frac{j\pi}{y_1} x}{\sinh \frac{j\pi}{y_1} x_2}$$

$$- \sum_{\substack{k \\ \text{odd}}} \frac{4V_+}{k\pi} \sin \frac{k\pi}{y_1} y \; \frac{\sinh \frac{k\pi}{y_1} (x-x_2)}{\sinh \frac{k\pi}{y_1} x_2}$$

where a, b, c and A, B, C are arbitrary constants (to be determined).

When the boundary conditions are applied to determine the arbitrary constants, the generality of the series solution will not be required; therefore, only the terms corresponding to m=1 and n=1 are retained in the series containing the arbitrary constants. This will produce a first order approximation to the actual potential distribution. The accuracy of this assumption will be checked by comparison with a purely numerical solution.

The various forms for the potential in each region already satisfy the boundary conditions imposed on the potential at the anode surface, at the pin surfaces, and at the substrate matrix. To determine the values of the arbitrary constants that remain in the above expressions, it is only necessary to require that the potential and its normal derivative satisfy the continuity conditions.

$$\phi_1\Big|_{x=-x_1} = \phi_2\Big|_{x=+x_2}$$

$$\phi_1\Big|_{x=0} = \phi_2\Big|_{x=0}$$

$$\phi_2\Big|_{y=0} = \phi_3\Big|_{y=0}$$

$$\frac{d\phi_1}{d\ell}\Big|_{x=-x_1} = \frac{d\phi_2}{d\ell}\Big|_{x=+x_2}$$

$$\frac{d\phi_1}{d\ell}\Big|_{x=0} = \frac{d\phi_2}{d\ell}\Big|_{x=0} \qquad \ell = x,y,z$$

$$\frac{d\phi_2}{d\ell}\Big|_{y=0} \quad \frac{d\phi_3}{d\ell}\Big|_{y=0}$$

Due to the independence of the circular and hyperbolic trigonometric functions involved in the various forms of the potential in each region, it is impossible to match the various solutions over each entire interface. It will be necessary, therefore, to match the solution at only one point on each interface. That point is arbitrary; but, the mid-point of each interface will be chosen; it is thought that the degree of approximation is quite good for this case. This assumption will be checked by comparison with a purely numerical solution.

After performing the required operations, the undetermined constants must satisfy the relations

$$a = -A\alpha$$

$$b = -B\beta$$

$$c = -C\gamma$$

and

$$a\zeta + b + \kappa_1 = A\eta + B - c\xi$$

$$a + b\zeta - \kappa_1 = A + B\eta + c\xi$$

$$A\chi_1 + B\chi_2 + C\mu = c\nu + \kappa_2$$

where

$$\zeta \equiv \cosh \frac{\pi}{y_2} x_1$$

$$\eta \equiv \cosh \frac{\pi}{y_2} x_2$$

$$\xi \equiv \frac{y_2}{x_2} \frac{\sinh \frac{\pi}{x_2} (y_m - y_2)}{\sin \frac{\pi}{y_2} y_m}$$

$$\chi_1 \equiv \frac{x_2}{y_2} \frac{\sinh \frac{\pi}{y_2} x_m}{\sin \frac{\pi}{y_2} x_m}$$

$$\chi_2 \equiv \frac{x_2}{y_2} \frac{\sinh \frac{\pi}{y_2} (x_m - x_2)}{\sin \frac{\pi}{y_2} x_m}$$

$$\mu \equiv \cosh \frac{\pi}{x_2} y_2$$

$$\nu \equiv \cosh \frac{\pi}{x_2} y_1$$

$$\kappa_1 \equiv \frac{y_2}{x_1} \frac{4V_+}{\pi} \frac{1}{\sin \frac{\pi}{y_2} y_m} \sum_{\substack{i \\ \text{odd}}} \frac{\sinh \frac{i\pi}{x_1} (y_m - y_2)}{\sinh \frac{i\pi}{x_1} y_2}$$

$$\kappa_2 \equiv - \frac{4V_-}{\pi} \frac{1}{\sin \frac{\pi}{x_2} x_m} \sum_{\substack{i \\ \text{odd}}} \frac{\sin \frac{i\pi}{x_2} x_m}{\sinh \frac{i\pi}{x_2} y_1}$$

$$+ \frac{x_2}{y_1} \frac{4V_+}{\pi} \frac{1}{\sin \frac{\pi}{x_2} x_m} \sum_{\substack{i \\ \text{odd}}} \frac{\sinh \frac{i\pi}{y_1} x_m - \sinh \frac{i\pi}{y_1} (x_m - x_2)}{\sinh \frac{i\pi}{y_1} x_2}$$

and

$$\left.\begin{aligned}\alpha &\equiv \frac{\sinh \frac{\pi}{y_2} x_2}{\sinh \frac{\pi}{y_2} x_1} \\ \beta &\equiv \frac{\sinh \frac{\pi}{y_2} x_2}{\sinh \frac{\pi}{y_2} x_1}\end{aligned}\right\} \alpha = \beta$$

$$\gamma \equiv \frac{\sinh \frac{\pi}{x_2} y_2}{\sinh \frac{\pi}{x_2} y_1}$$

and

$$x_m \equiv \frac{x_2}{2}$$

$$y_m \equiv \frac{y_2}{2}$$

Notice that

$$C = \frac{\kappa_2 - A\chi_1 - B\chi_2}{\mu + \gamma\nu}$$

Therefore

$$A[\xi\chi_1 + (\alpha\zeta + \eta)(\mu + \gamma\nu)] + B[\xi\chi_2 + (\beta + 1)(\mu + \gamma\nu)] = \xi\kappa_2 + \kappa_1(\mu + \gamma\nu)$$

$$A[\xi\chi_1 - (\alpha + 1)(\mu + \gamma\nu)] + B[\xi\chi_2 - (\beta\zeta + \eta)(\mu + \gamma\nu)] = \xi\kappa_2 + \kappa_1(\mu + \gamma\nu)$$

These simultaneous equations can be easily solved for A and B

$$A = \frac{(v-p)c - (v+q)k}{\Delta}$$

$$B = \frac{-(u-q)c + (u+p)c}{\Delta}$$

where

$$u \equiv \xi\chi_1$$

$$v \equiv \xi\chi_2$$

$$p \equiv (\alpha\zeta+\eta)(\mu+\gamma\nu)$$

$$q \equiv (\alpha+1)(\mu+\gamma\nu)$$

and

$$\left.\begin{aligned} c &\equiv \xi\kappa_2 + \kappa_1(\mu + \gamma\nu) \\ k &\equiv \xi\kappa_2 + \kappa_1(\mu + \gamma\nu) \end{aligned}\right\} \quad c = k$$

and

$$\Delta \equiv (v-p)(u+p) - (v+q)(u-q)$$

For a non-trivial solution, Δ must not equal zero.

With A and B determined, C can be determined from above. With A, B, C determined, the constants a, b, c can be determined from above. This information can then be substituted into the defining equations for the potential in the different regions. The results of actually determining the remaining constants and substituting their values back into the defining equations for the potential are quite lengthy, and therefore, are not presented.

B. NUMERICAL ANALYSIS

In the preceding theoretical analysis of the field emission properties of a planar electron emitting array, a solution to the Laplace equation in the interelectrode space was obtained for the perpendicular and parallel cross-sectional geometries of the model with respect to the plane of the dielectric substrate. It is observed that the theoretical analysis is complicated by the periodicity of the structure and by the closeness of the planar anode structure above the

pins. The solution to the Laplace equation for a device with non-periodic spacing of the pins or with pins of a geometry for which the Laplace equation is inseparable, is very complicated if not impossible; and, at best, it will produce an answer in the form of a slowly converging infinite series.

An alternate approach to this problem is to solve the Laplace equation by a purely numerical-type solution and to implement this solution on a high speed computer. With reasonable pin spacing distributions and specified individual pin geometries (which, incidently, need not be the same for each pin) a numerical solution of the Laplace equation can be made to produce a reasonably accurate representation of the exact solution in a finite amount of time.

A computer program is now available which will solve the Laplace equation in any two-dimensional region subject to any set of boundary conditions. The results of this program is a plot of the potential distribution within the given boundaries determined in the program. The output can be obtained as a relief map of the potential or as an equipotential contour plot. Examples of each type of output are present in this report.

In the following plots the various pin distributions are enclosed on the top and on the sides by a grounded conducting box. The pin distributions need not actually be inside this box, as the program can accommodate a finite section of a periodic array of pins; however, the grounded

box has little effect on the values of the potential inside the pin distributions away from the edges of the box, and has the advantages of greatly speeding the convergence of the computer program. For these initial runs it was thought that this approximation was justified.

Figure 38 is an equipotential contour plot for a distribution of several circular conducting pins inside a grounded square. This is a top view looking down on the pin distribution (see Case 1).

Figure 39 is an equipotential contour plot for a distribution of several cylindrical conducting pins under a grounded rectangle. This is a side view looking across the pin distribution (see Case 2).

Figure 40 is an equipotential contour plot showing the effects of placing a grid of wires above the pin distribution for various grid potentials.

Figure 41 is an equipotential contour plot showing the effect of a recessed pin distribution on the potential distribution. Figures 42 and 43 are relief maps of the potential distribution of several circular conducting pins inside a grounded square comparing the effects of various pin diameters. The diameter of the pins in Figure 43 are greater than those of Figure 42.

Figure 44 is a relief map of the potential distribution showing the effects of non-uniform pin spacings and non-uniform charge distributions.

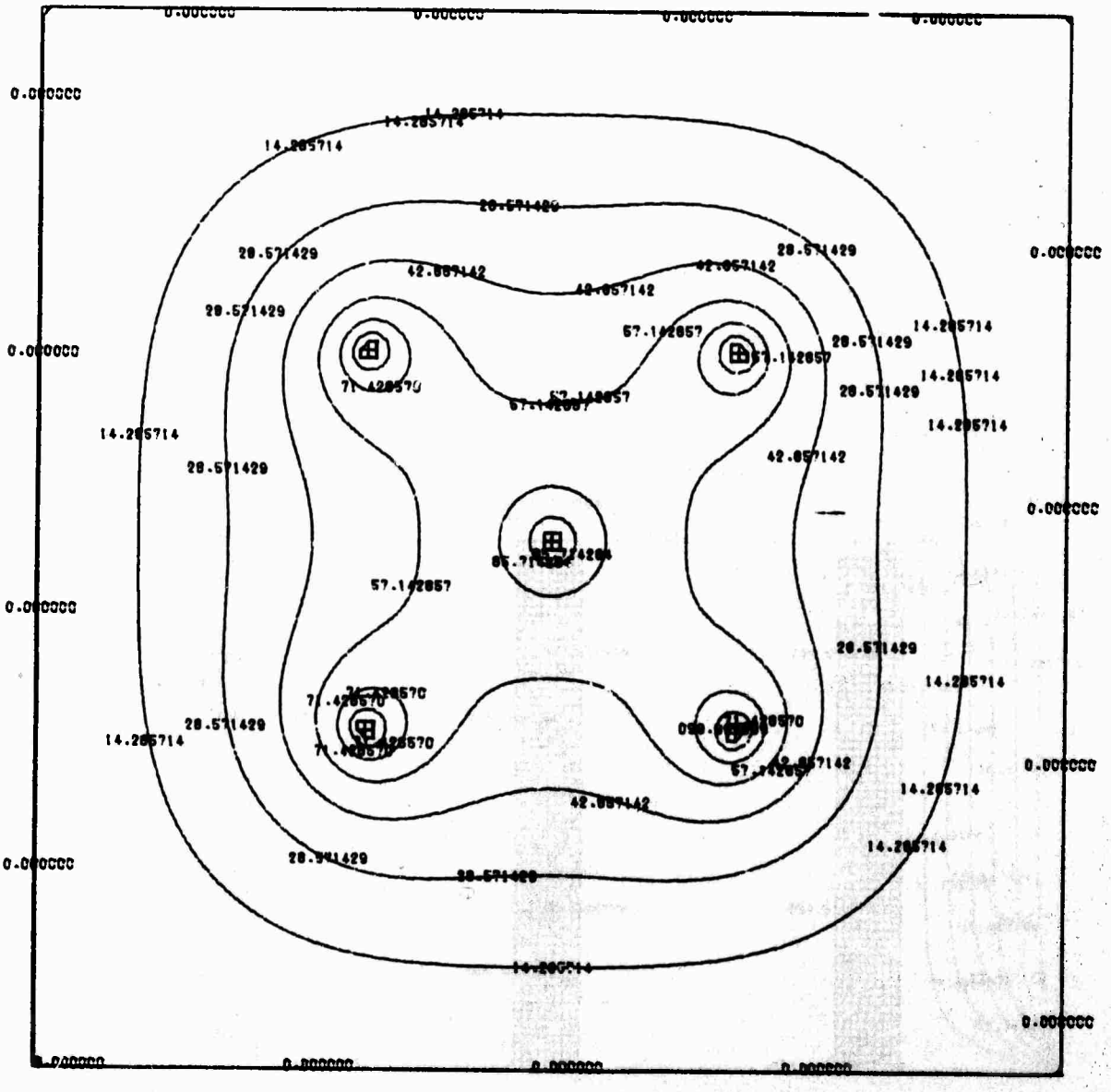

Figure 38. Equipotential Contour Plot for a Distribution of Several Circular Pins Inside a Grounded Square.

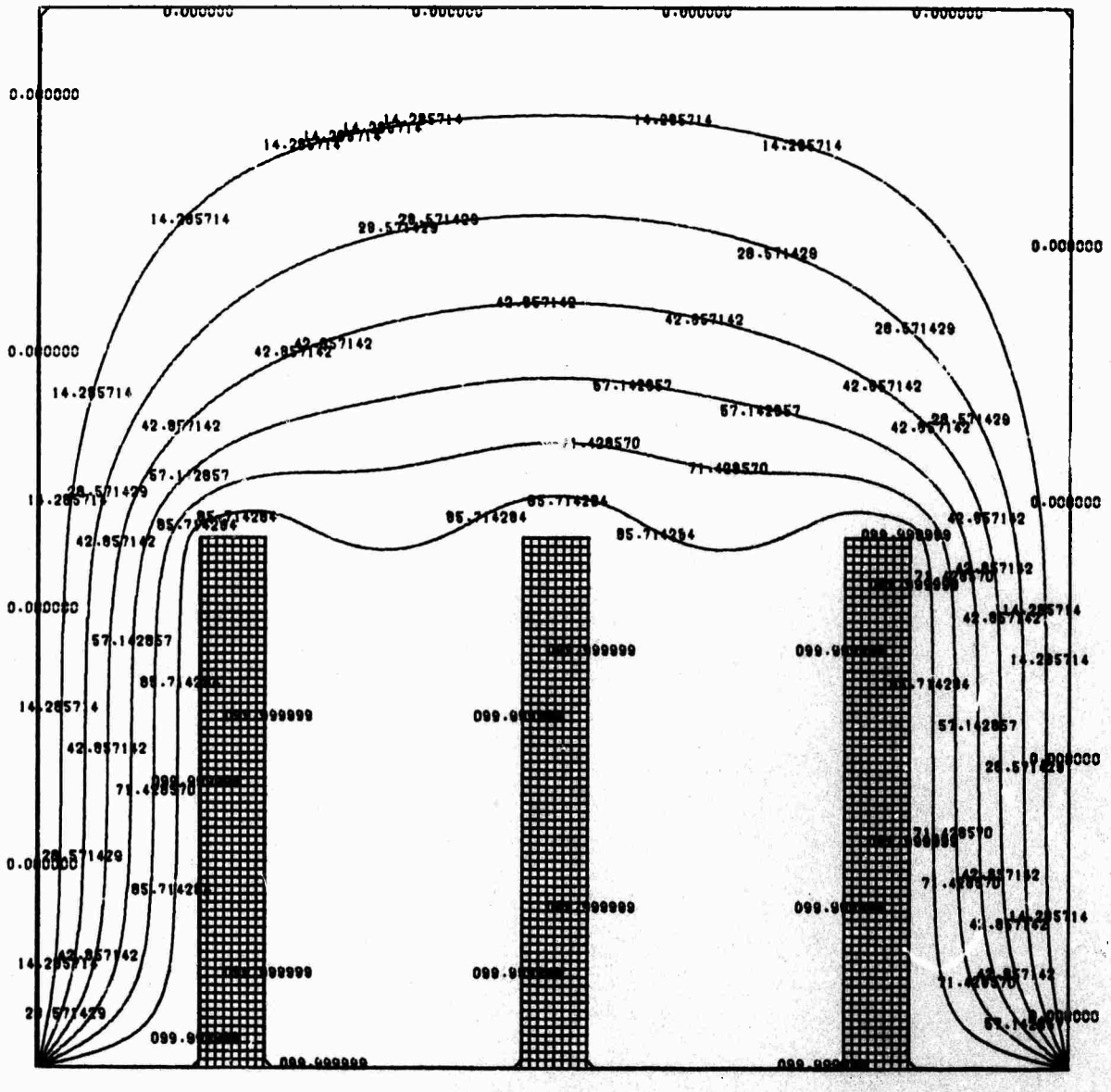

Figure 39. Equipotential Contour Plot for a Distribution of Several Cylindrical Conducting Pins Under a Grounded Rectangle.

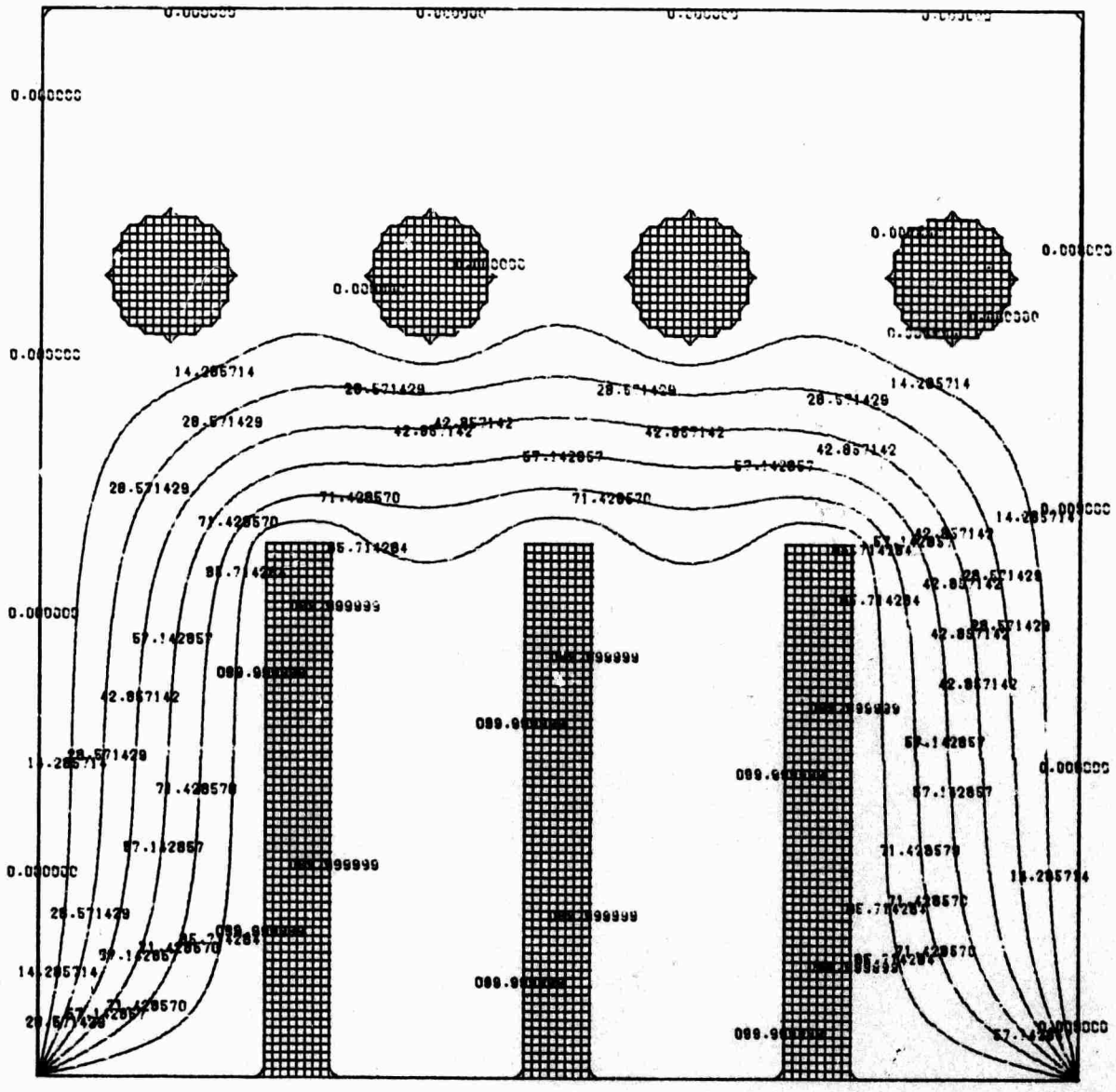

Figure 40. Equipotential Contour Plot for a Distribution of Several Cylindrical Conducting Pins With a Grounded Grid and Under a Grounded Rectangle.

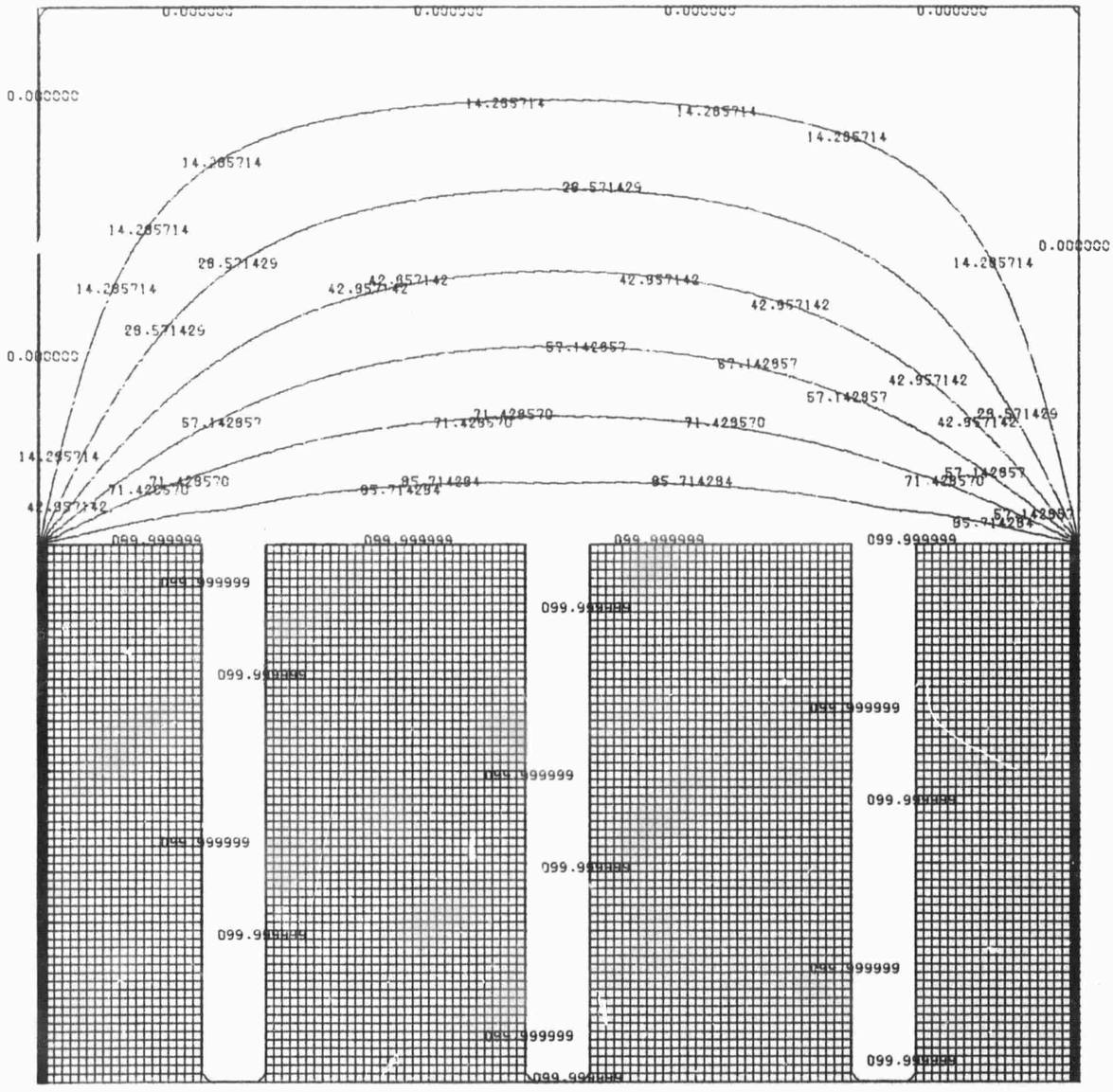

Figure 41. Equipotential Contour Plot for Several Cylindrical Recessed Pins Under a Grounded Rectangle.

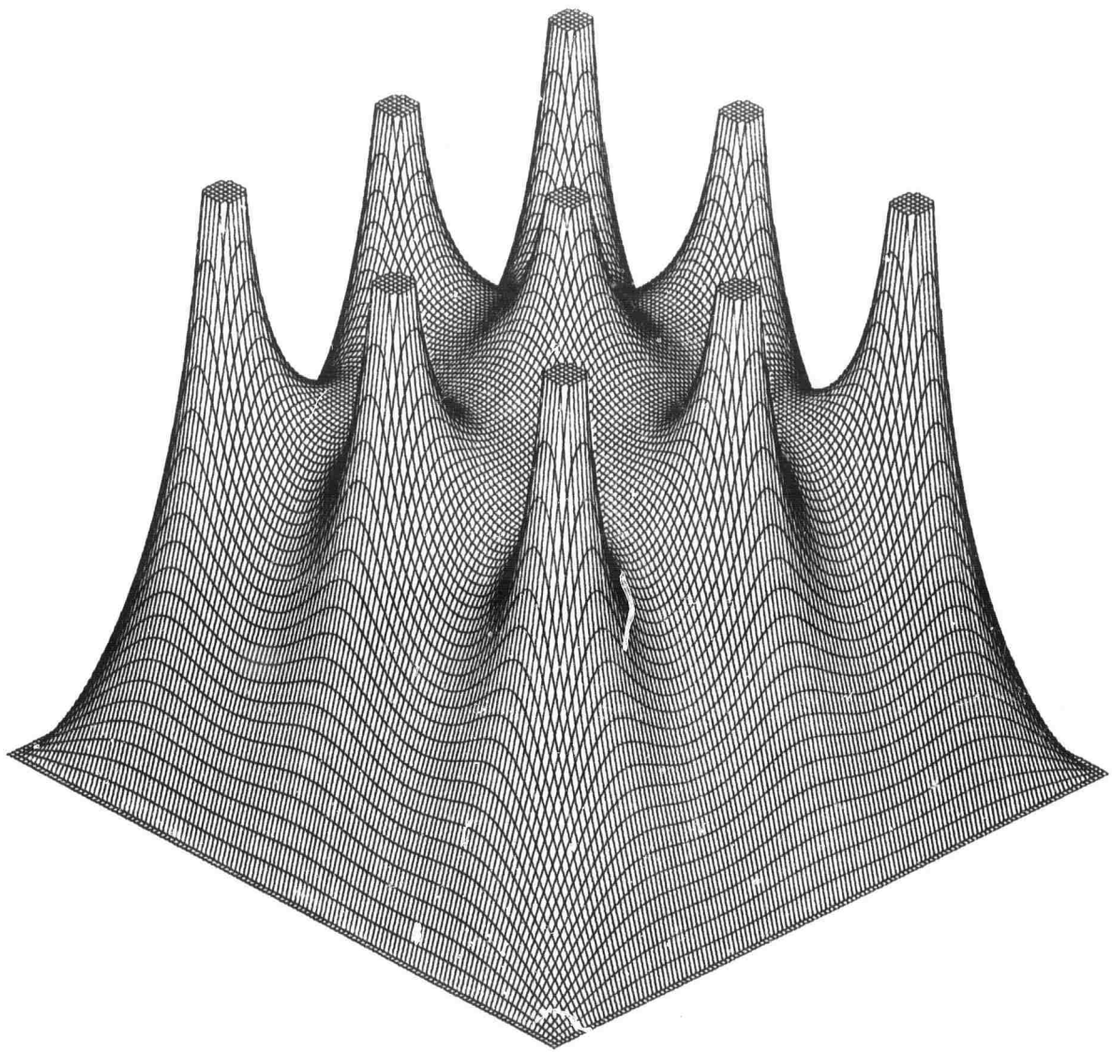

Figure 42. Relief Map for a Distribution of Several Small Diameter Conducting Pins Inside a Grounded Square.

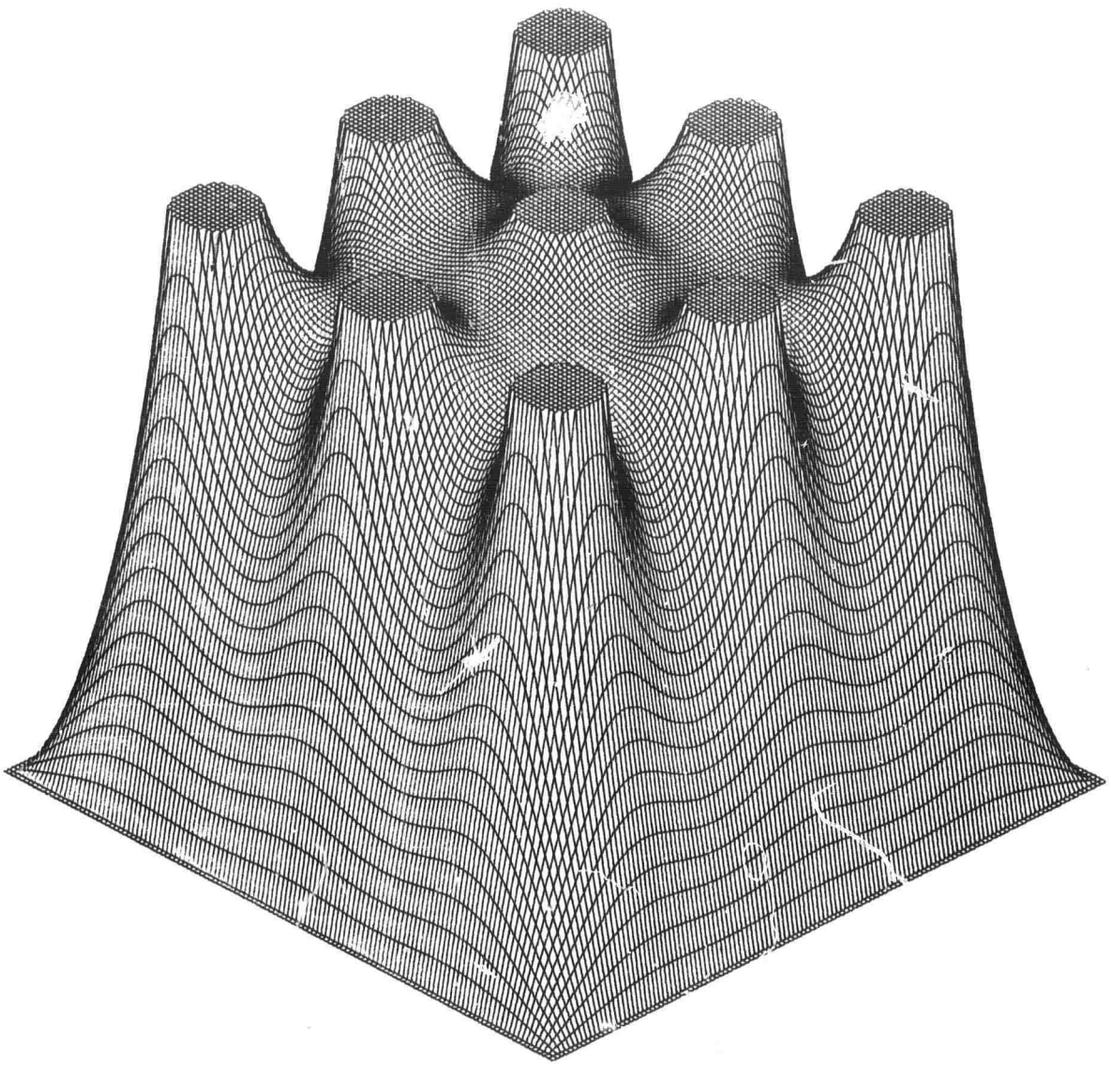

Figure 43. Relief Map for a Distribution of Several Large Diameter Conducting Pins Inside a Grounded Square.

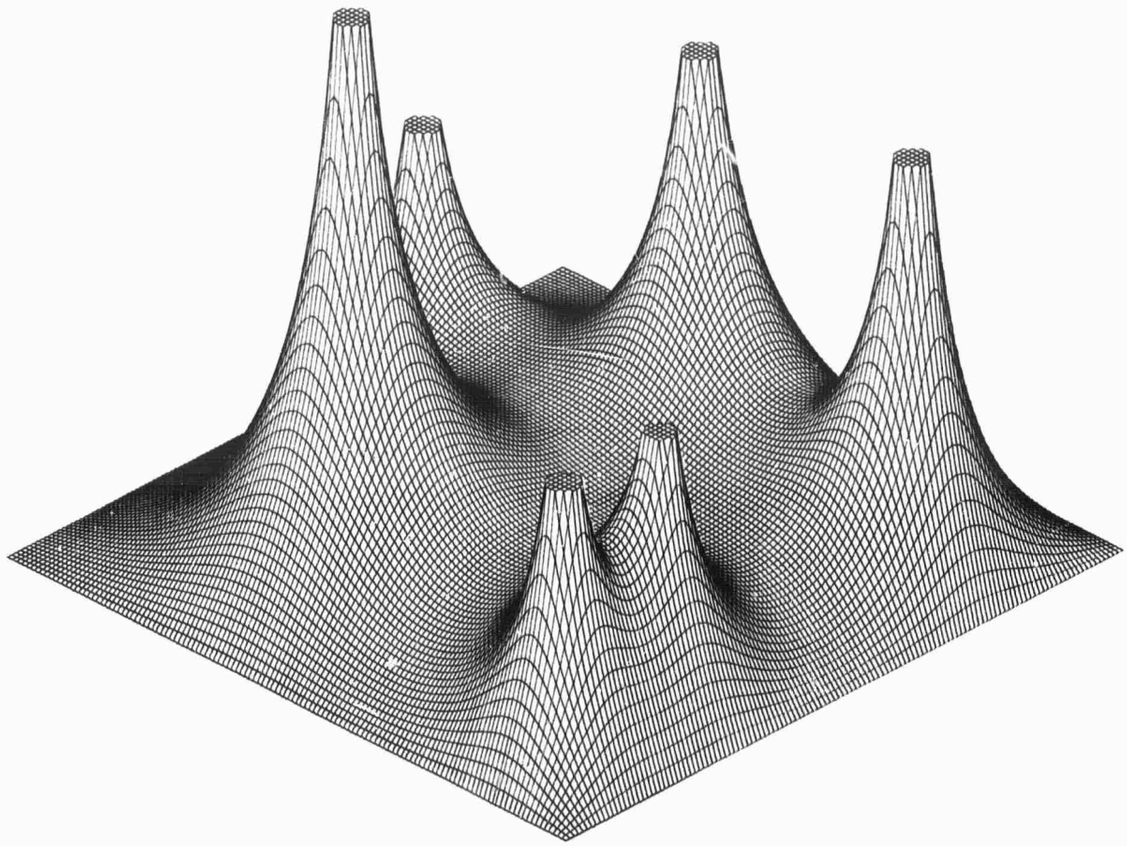

Figure 44. Relief Map for a Distribution of Circular Conducting Pins Inside a Grounded Square Showing the Effects of Non-Uniform Pin Spacings and Charge Distributions.

SECTION VI

EXPERIMENTAL EMISSION MEASUREMENTS

This section describes the experimentally observed electron emission characteristics of the oxide-metal composite materials. Most of the experimental work was performed with the test diode described previously,[1,2] but part of the work was done with a segmental collector assembly that was subsequently added to the test apparatus, and the fabrication of this collector is described.

A summary of representative experimental results is presented both for those emitters having exposed pins and those having flush pins. Results obtained with the segmental collector assembly are given, and the observed correlation with emitter morphology is indicated.

A. EXPERIMENTAL APPARATUS

The major components of the experimental apparatus have been described previously.[1,2] Since that time the vacuum chamber bakeout has been improved so that a base pressure of $2\text{-}3 \times 10^{-10}$ Torr is routinely obtained. The previously described test diode, which was also used in the current measurements, suffered from the disadvantage of an inadequate power dissipation capability. Thus, under moderate power

operation (about 30 watts) the anode expanded and decreased the interelectrode spacing which further increased the current and attendent heating. Best experimental results were obtained when the measurements were completed before the anode became hot enough to experience significant thermal expansion. Probably the "hysteresis" effect noted previously[1] was at least partially attributable to the thermal expansion of the anode.

Figure 45 shows the test diode modified to include the segmental collector assembly. The collector was constructed from a glass-epoxy printed circuit board. The copper cladding of the board was cut so as to form a 25-segment matrix with 0.09 x 0.09 inch segments. The segments are separated by the 0.010 inch width of the saw that was used to make the collector. The work was performed on a milling machine. The segments were indexed and blind-drilled from the back (insulator) side to receive leads which were soldered to the copper cladding. The wire leads go first to a support standoff insulator and then to a 20-pin feedthrough. Since only 20 pins were available, the four corner pins were grounded and one lead was made common to two segments.

Because of its printed circuit board construction, the test diode matrix has a poor heat dissipation capability. Therefore, in operation, the total device power dissipation was kept below about 0.2 watts.

Vacuum performance of the segmental collector, which was not expected to be particularly good, has been quite

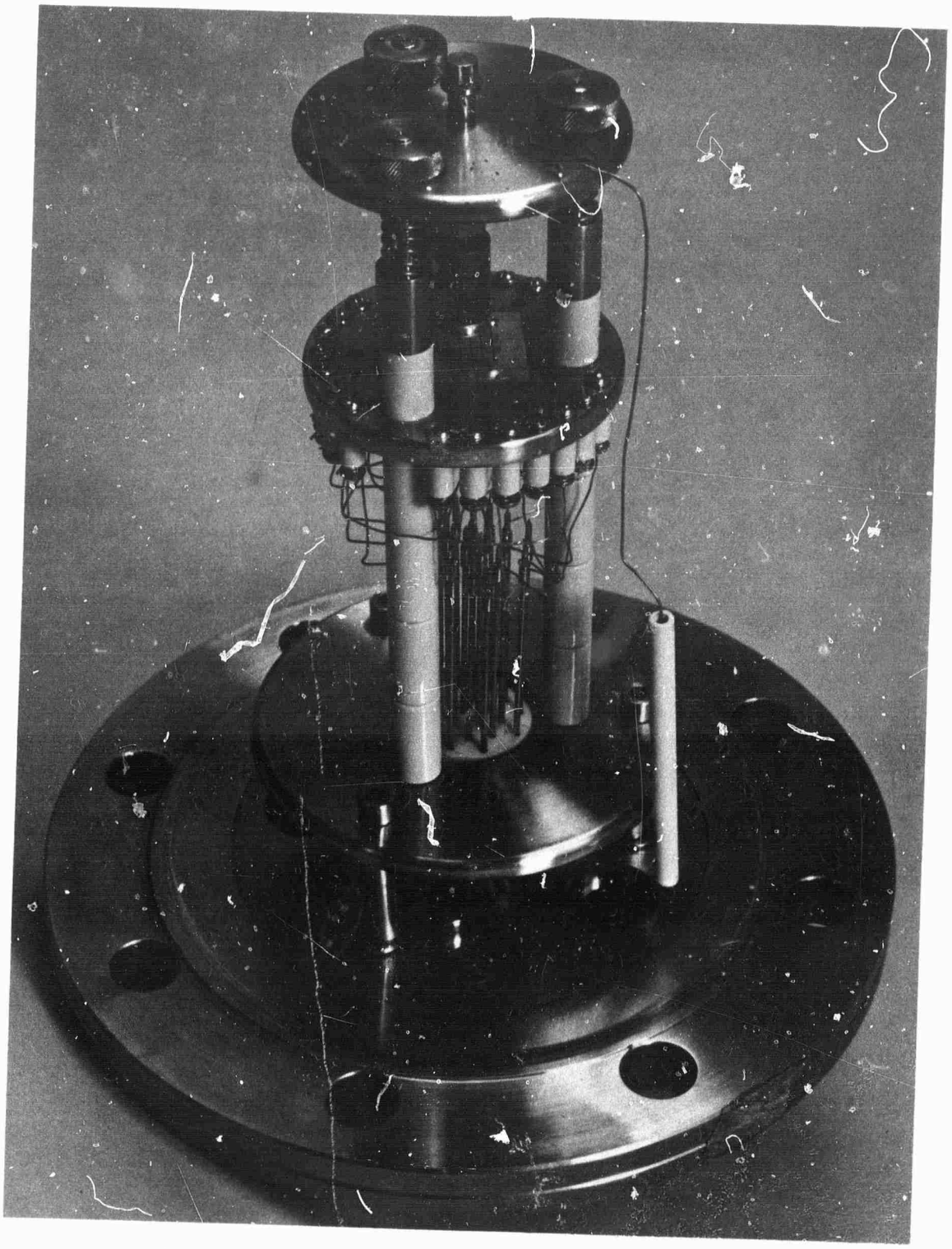

Figure 45. Overall View of the Test Diode Showing the Segmental Electron Collector Assembly.

satisfactory. The use of soft soldered connections precluded bakeout temperatures greater than about 100°C, and the glass-epoxy circuit board was expected to have a relatively high outgass rate. Nevertheless, an operating pressure of approximately 3×10^{-9} Torr was routinely obtainable with the test diode; this pressure was adequate for the purpose of the emission experiments.

B. ELECTRON EMISSION MEASUREMENTS

This section gives a summary of the electron emission measurements. All of the data are for UO_2-W composites. A ZrO_2-W sample was tested, but emission data for this sample were not reproducible. Measured currents were quite low, with 5μa at 8000 V and 0.01 inch spacing being the largest value recorded. It is probable that this lack of reproducibility was due to poor contact between the W pins and the cathode support. Of the several UO_2-W samples tested, gross emission data are presented only for UO_2-W sample 13-48. This particular sample was chosen because it is representative of the material from which the most copious emission has been obtained and because both exposed pin and flush pin emission testing was performed using this sample.

Electron emission data utilizing the segmental collector are given for Samples 136/11-11 and 13-58/11-8. These data indicate the degree of correlation obtainable between the segmentary collector data and the observed emitter morphology.

satisfactory. The use of soft soldered connections precluded bakeout temperatures greater than about 100°C, and the glass-epoxy circuit board was expected to have a relatively high outgass rate. Nevertheless, an operating pressure of approximately 3×10^{-9} Torr was routinely obtainable with the test diode; this pressure was adequate for the purpose of the emission experiments.

B. ELECTRON EMISSION MEASUREMENTS

This section gives a summary of the electron emission measurements. All of the data are for UO_2-W composites. A ZrO_2-W sample was tested, but emission data for this sample were not reproducible. Measured currents were quite low, with 5μa at 8000 V and 0.01 inch spacing being the largest value recorded. It is probable that this lack of reproducibility was due to poor contact between the W pins and the cathode support. Of the several UO_2-W samples tested, gross emission data are presented only for UO_2-W sample 13-48. This particular sample was chosen because it is representative of the material from which the most copious emission has been obtained and because both exposed pin and flush pin emission testing was performed using this sample.

Electron emission data utilizing the segmental collector are given for Samples 136/11-11 and 13-58/11-8. These data indicate the degree of correlation obtainable between the segmentary collector data and the observed emitter morphology.

These particular samples were chosen because of their large area; the large area was necessary for best utilization of the rather coarse resolution of the segmental collector.

1. Gross Emission Measurements

Representative emission data are presented for UO_2-W sample 13-48 in Figure 46. Two curves are given; the first curve gives the emission as a function of anode potential for the case where the matrix was selectively etched to expose the pins, while the second curve reflects the emission from the same sample after the pins were polished flush with the UO_2 matrix. The interelectrode spacing employed to obtain the data for both curves was 0.015 inch. This information indicates that, with the same interelectrode spacing, flush pin electron emitters can give current densities comparable to those achieved with exposed pins if the anode voltage is increased by a factor of about three. This requirement for increased anode potential is due mostly to the larger effective pin radius and hence smaller electric field of the flush pin electron emitter.

It should be noted that Figure 46 compares two of the many sets of data that were taken with Sample 13-48. Emission characteristics were taken for other interelectrode spacings and anode potential regimes. The largest electron emission current density yet measured (about 100 mA/cm^2) in the present research was recorded with Sample 13-48 (exposed pins) operating with an interelectrode spacing of 0.01 inch and an anode

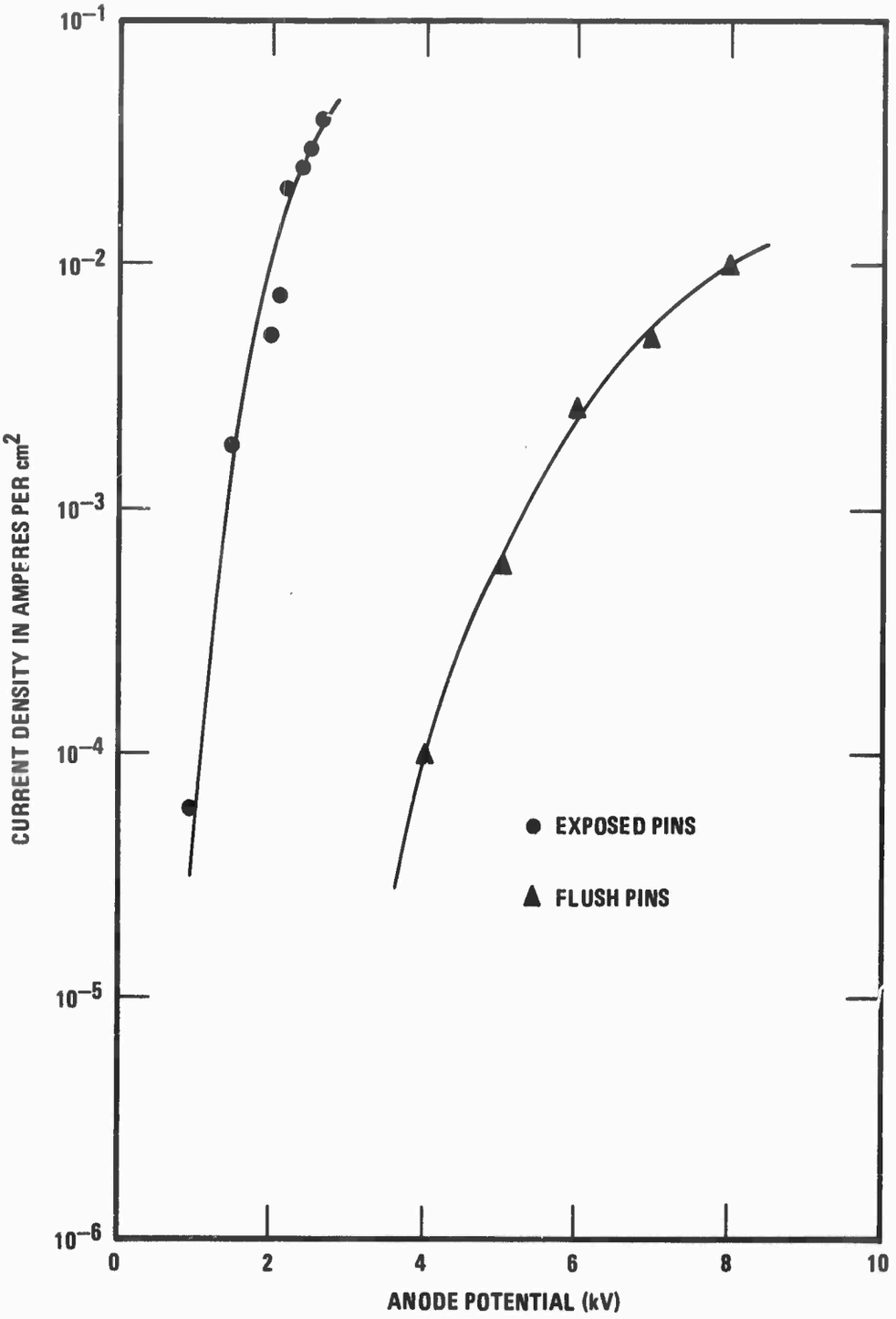

Figure 46. Field Emission Current Density as a Function of Anode Potential for UO_2-W Sample No. 13-48 Using a 0.015 Inch Interelectrode Spacing.

potential of 3000 V. The maximum obtainable current, for both exposed pins and flush pins, was always limited by the onset of electrical breakdown in the test diode.

The growth/etch characteristics of Sample 13-48 (exposed pins) are shown in Figure 47a. Additional SEM micrographs at higher magnification revealed the pins were quite long (2 x 10^{-3}cm). The structure contains, along with the oxide-metal eutectic regions, circular areas of primary UO_2 that are depleted of pins.

Figure 47b shows the degree of post-emission damage to Sample 13-48 (exposed pins). It can be seen that a few scattered arc craters exist, but that the damage is not extensive. Almost all of the post-emission damage was confined to one region of the sample.

Post-emission damage to Sample 13-48 (flush pins) is depicted in Figure 48. It is apparent that when arcs occur, they terminate on a pin. This is logical since emission current originates from the pins. The shingle-like layers of oxide partially detached from the UO_2 matrix are probably produced as a result of rapid sample heating and the subsequent spalling of the surface layers.

2. Spatial Distribution of the Electron Emission

Emission results obtained with the segmental collector assembly are presented in this section. A diagram of the collector-segment numbering system and experimental data for two samples are given. The correlation of collector data with

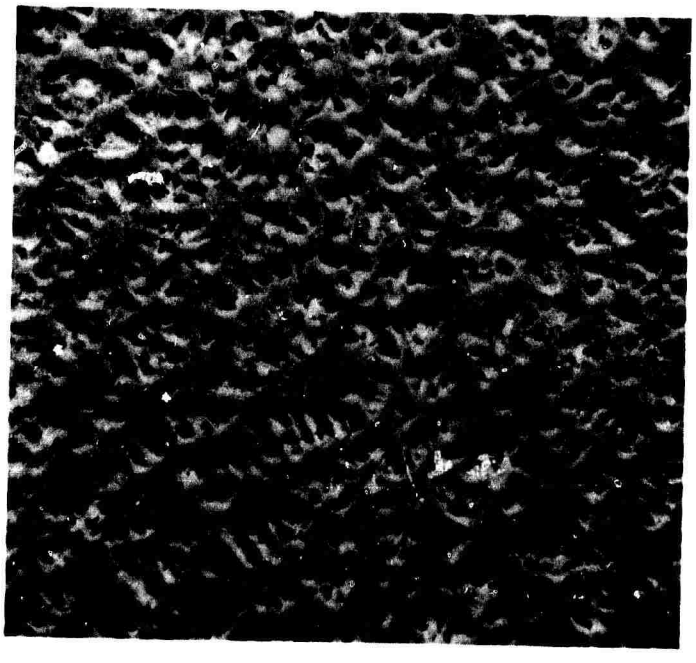

a. Pre-Emission Growth-Etch Characteristics, X100.

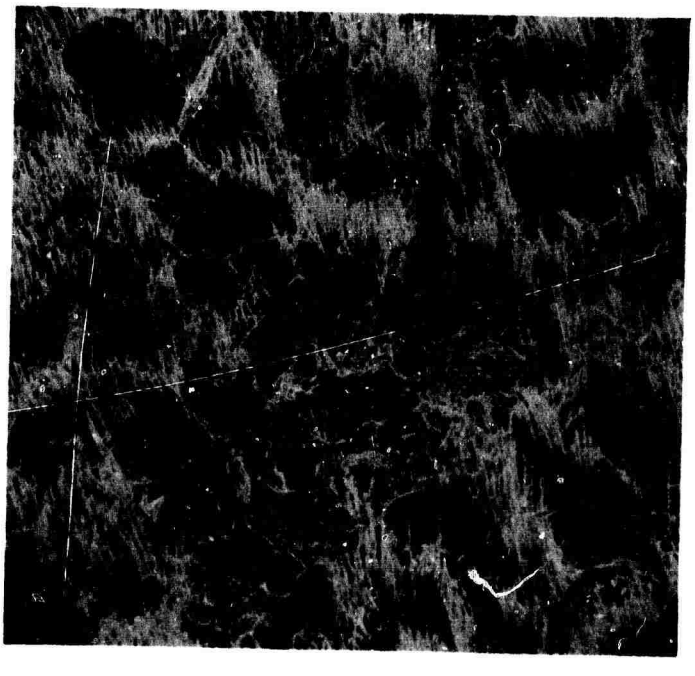

b. Post-Emission Damage, X550.

Figure 47. Scanning Electron Micrographs of UO_2 Sample No. 13-48.

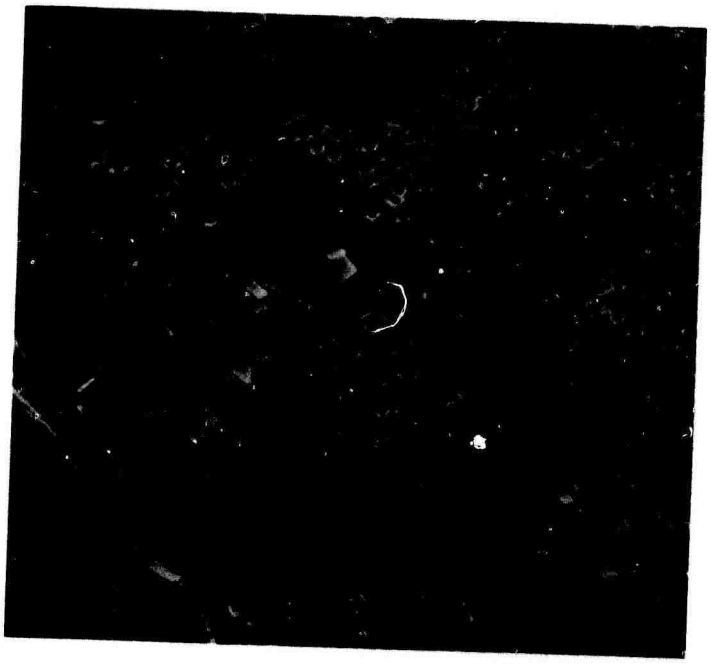

Figure 48. Scanning Electron Micrograph of UO_2-W Sample No. 13-48 With Flush Pins Showing Post-Emission Damage, X1100.

emitter morphology is discussed.

Figure 49 shows Sample 136/11-1 with the collector grid superimposed over it. The currents collected by each segment are given in Table III. Note that segments numbered 1, 2, 5, 7, and 13 are receiving almost all of the current. These segments are all concentrated along one edge of the sample. It was first thought that perhaps an uneven interelectrode gap spacing was responsible for this concentration of current along one edge. To check this hypothesis, the interelectrode spacing was made nonparallel in such a manner as to enhance the emission from those areas from which low emission was initially noted. No significant change in the absolute current magnitude or distribution of current was observed after making the change in spacing, thus suggesting that the variation in emission was due to differences in pin growth-etch characteristics across the sample. This suggestion was confirmed by subsequent SEM examination. Figure 50a shows the growth typical around areas 2 and 6. It can be seen that the pins are well exposed and have good, high density growth. This can be contrasted with Figure 50b which shows area 17, one of those areas having poor emission. The pins around area 17 are neither dense nor well exposed. The rough appearance of the substrate is indicative of poor etching in this area. Therefore, it is reasonable to conclude that, at least for this particular case, the electron emission spatial distribution was determined by the emitter growth and preparation

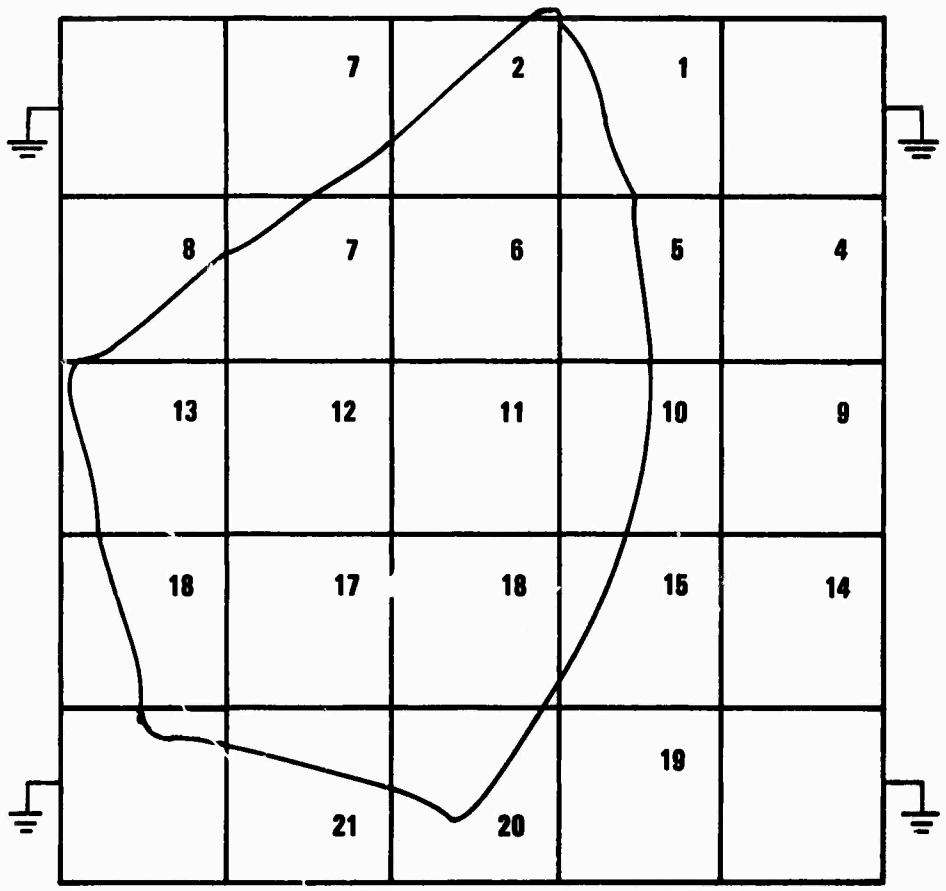

Figure 49. Outline of UO_2-W Sample No. 136/11-1 With Superimposed Collector Grid.

TABLE III

SPATIAL DISTRIBUTION OF FIELD EMISSION CURRENT

Segment Number	Collected Current (A)* Sample No. 136/11-1	Sample No. 158/11-8
1	6.2×10^{-6}	2.6×10^{-5}
2	8.0×10^{-6}	1.6×10^{-5}
3	4.0×10^{-11}	3.8×10^{-9}
4	-	1.2×10^{-5}
5	4.0×10^{-6}	7.0×10^{-6}
6	7.7×10^{-8}	2.2×10^{-6}
7	2.4×10^{-6}	1.8×10^{-5}
8	9.0×10^{-7}	2.0×10^{-4}
9	-	2.8×10^{-6}
10	9.0×10^{-9}	1.6×10^{-5}
11	1.0×10^{-9}	5.0×10^{-6}
12	1.7×10^{-7}	6.0×10^{-6}
13	1.1×10^{-6}	4.0×10^{-5}
14	-	6.0×10^{-8}
15	1.2×10^{-10}	2.4×10^{-6}
16	1.0×10^{-10}	2.2×10^{-7}
17	1.4×10^{-10}	4.0×10^{-7}
18	2.2×10^{-10}	2.2×10^{-6}
19	-	1.0×10^{-8}
20	2.0×10^{-10}	5.0×10^{-9}

*Anode potential 5kV, interelectrode spacing approximately 0.02 in for both samples.

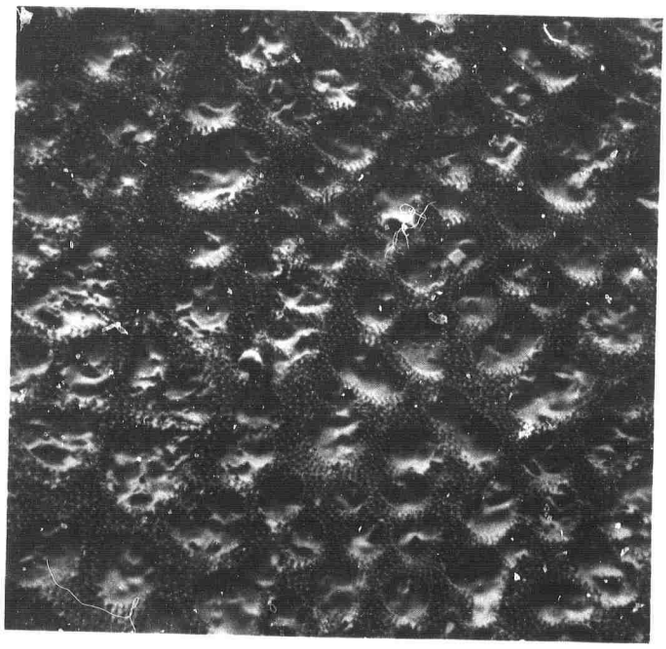

a. Growth-Etch Characteristics Under Collector Segments 2 and 6. X220.

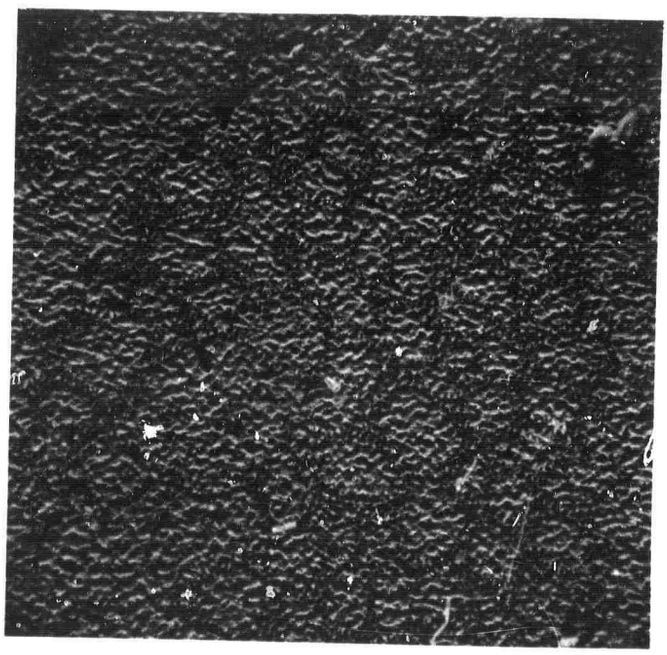

b. Growth-Etch Characteristic Under Collector Segment 17. X230.

Figure 50. Scanning Electron Micrographs of UO_2-W Sample No. 136/11-1

characteristics and not by variations in the interelectrode spacing.

Data for Sample 13-58/11-8 are also presented in Table I. Those segments which show the low current values, i.e. numbers 3, 14, 19, and 20, were positioned over the polycrystalline skinand are not expected to show significant emission current. (In general, however, the electron emission from this sample is much more uniform that that from the previously described sample.) A set of scanning electron micrographs that compare areas 8 and 13 with area 16 is given in Figures 51a and b. Note that the pin height and density are slightly greater in the areas 8 and 13, thus giving an indication that the emission current should be higher in those areas. This is in agreement with the observed electron emission. The tips of the pins shown in Figure 51 are deformed (sheared); this is the typical tip shape observed after slicing UO_2-W samples (with a diamond saw) and etching the samples without first polishing the surface to be etched.

In the future selection of emission samples, more effort will be devoted to the complete characterization of the composite structures prior to emission testing. Other techniques, besides the use of silver paste, are under investigation as ways to connect the pins of the emitter structure to the cathode assembly.

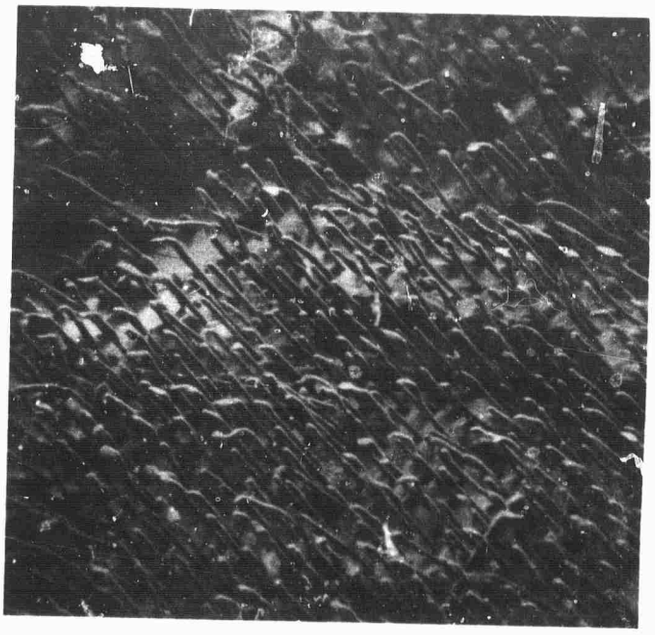

a. Growth-Etch Characteristics Under Collector Segments 8 and 13, X1200.

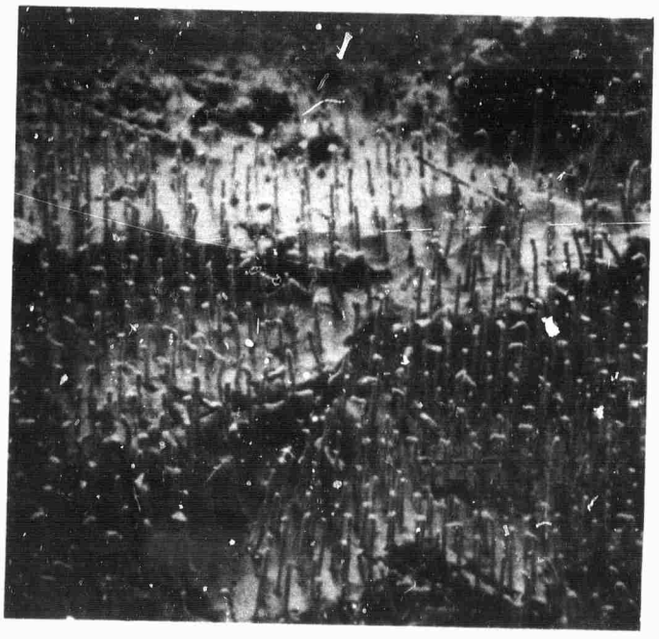

b. Growth-Etch Characteristics Under Collector Segment 16. X1300.

Figure 51. Scanning Electron Micrographs of UO_2-W Sample No. 13-58/11-8.

SECTION VII

SUMMARY

During the last eighteen months work has been underway on ARPA Order No. 1637 developing melt-grown oxide-metal composite structures suitable for electron emission testing. The objective of this study is to understand the growth processes and parameters that produce ordered eutectic structures during controlled solidification of oxide-metal mixtures, and to produce samples suitable for the evaluation of their potential for electronic applications. To meet these objectives the research program is divided into five areas:

1. Induction Coupling and Solidification Behavior of Oxides and Oxide-Metal Mixtures.
2. Structural and Chemical Characterization of Oxide-Metal Composites.
3. The Formation of Optimum Emitting Arrays.
4. Field Emission Theory.
5. Experimental Emission Measurements.

The current method used to grow the oxide-metal composites is a modified floating-zone technique where the oxide-metal mixtures are internally melted using induction heating and, subsequently, unidirectionally solidified to achieve ordered growth. Prior to this report successful growth had been

achieved only in the system UO_2-W and to a lesser extent in stabilized ZrO_2-W samples. In search of new oxide-metal mixtures adaptable to this growth scheme, the induction coupling characteristics of numerous oxides, oxide compounds and oxide mixtures were studied. Results of this work lead to the successful development of Y_2O_3 stabilized HfO_2-W as an additional refractory oxide-metal combination suited for composite growth and samples suitable for property measurements have been grown.

Major insight into the parameters controlling extensive ordered growth of stabilized ZrO_2-W samples has been obtained and the initial emission testing of this material was performed. Previous attempts to add refractory metals besides W to UO_2 and achieve ordered structures had proved unsuccessful. Recent experiments using UO_2-Ta mixtures have produced extensive areas of Ta fiber growth in this oxide and some of the reasons for this improved growth have been delineated.

X-ray diffraction techniques and the scanning electron microscope (SEM) have been employed for the routine characterization of oxide-metal structures. The initial orientation information for stabilized ZrO_2-W structures indicated the preferred growth direction is [111] for the oxide and [110] for the metal fibers. Interestingly, this is identical to the dominant orientation found for UO_2-W. Attempts to examine impurity profiles across UO_2-W surfaces using conventional microprobe equipment were inconclusive. Similar analyses

using the SEM in conjunction with an energy dispersive detector indicated this instrument provided the necessary spatial resolution to examine individual oxide-matrix metal-fiber interfaces and this work suggested the major metallic impurity, iron, is segregated in the W fibers.

The question of oxide stoichiometry and its influence on composite growth was extensively considered during this report period. Stabilized ZrO_2 samples containing no W were melted in H_2 and readily formed a black substoichiometric material, whereas melting the same composition in N_2 produced clear transparent crystals. Increasing the N_2:H_2 ratio during the growth of UO_2-W samples reduced the occurrence of sample cracking during cooling, and promoted the growth of sound (crack-free) composite rods.

Selective chemical etching was used to expose, shape and recess the tungsten pins to form interesting oxide-metal emitter structures. Attempts to selectively remove the ZrO_2 matrix and expose the W pins in the stabilized ZrO_2-W samples using a variety of approaches met with only limited success, because of the chemical inertness of ZrO_2.

A theoretical analysis of the field emission anticipated from an array of conducting metallic pins, uniformly embedded in and protuding above, an insulating matrix has been undertaken. The first step in this analysis, the determination of the electric potential distribution within the interelectrode space, is being developed as a function of the array geometry

and the electrical properties of the composite. The resultant equations for the electric potential are complicated, if not impossible to solve, and numerical approaches have been employed to obtain computer plots of the equipotential surfaces for several different pin array geometries.

The experimental measurements of the electron field emission of selected oxide-metal structures were continued with the primary objective of predicting the performance of these materials as cathodes in practical electron devices. Gross electron emission current densities of approximately 100 mA/cm^2 can be routinely achieved. Attempts to exceed this current density have been limited by the onset of electrical breakdown in the test diode. A contributing factor to this electrical breakdown may be the outgassing of the anode structure due to excessive heating.

A series of emission experiments using a segmental collector assembly capable of correlating the emission from selected areas of the emitter surface with the pin morphology in that area were performed. These measurements indicated that non-uniform composite growth and etching characteristics were more influential in controlling the emission than such factors as slightly nonparallel emitter-collector surfaces.

REFERENCES

1. A. T. CHAPMAN, et. al., "Melt-Grown Oxide-Metal Composites", Final Technical Report (No. 2), ARPA Order No. 1637 and Contract DAAH01-70-C-1157, School of Ceramic Engineering, Georgia Institute of Technology, July 1971.

2. A. T. CHAPMAN, et. al., "Melt-Grown Oxide-Metal Composites", Semi-Annual Technical Report (No. 1), ARPA Order No. 1637 and Contract DAAH01-70-C-1157, School of Ceramic Engineering, Georgia Institute of Technology, January 1971.

3. S. C. CARNIGLIA, et. al., "Phase Equilibrium and Physical Properties of Oxygen-Deficient Zirconia and Thoria", J. Am. Cer. Soc. 54 1 13-17 (1971).

4. P. DUWEZ, "The Zirconia-Yttria System", J. Electrochem. Soc. 98 9 356-62 (1951).

5. J. D. Levine, "The 3-D Electrostatic Potential Surrounding a Square Array of Surface Charges", Surface Sci. 10 313-26 (1968).